FORCE INTERACTION AND SENSING IN BIO-MICROMANIPULATION

Ali Ghanbari

A thesis submitted for partial fulfillment of the degree of

Doctor of Philosophy

in

Mechatronics Engineering

University of Canterbury

Christchurch, New Zealand

December 2012

To my parents, Batool & Hossein

ABSTRACT

Micromanipulation is considered a challenging task which requires high precision motion and measurement at the micro scale. When micromanipulation is concerned with living organisms important considerations need to be addressed. These include the physical or chemical properties of micro-organisms, living conditions, responses to the environment and achieving suitably delicate manipulation.

Bio-micromanipulation can include micro surgery or cell injection operations, or to determine interaction forces as the basis to investigate behavior and properties of living micro-organisms. In order to achieve suitable bio-micromanipulation appropriate processes and/or sensory systems need to be investigated. This thesis aims to look into the force interaction and sensing addressing two distinctive challenges in the field of bio-micromanipulation.

To this end, this thesis presents two major contributions to advancing bio-micromanipulation. Firstly, a novel *Haptic Microrobotic Cell*

Injection System is introduced which is able to assist a bio-operator through haptic interaction. The system introduces a mapping framework which provides an intuitive method for the bio-operator to maneuver the micropipette in a manner similar to handheld needle insertion. To accurately control the microrobot, a neuro-fuzzy modeling and control scheme has been developed. Volumetric, axial and planar haptic virtual fixtures are introduced to guide the bio-operator during cell injection. Aside from improving real-time operator performance using the physical system, the system is novel in facilitating virtual offline operator training.

Secondly, a first-of-its-kind *micro-pillar based on-chip system* for dynamic force measurement of *C. elegans* motion is introduced. The system comprises a microfabricated PDMS device to direct *C. elegans* into a matrix of micropillars within a channel mimicking its dwelling environment. An image processing algorithm is able to track the interaction of the *C. elegans* with the pillars and estimate contact forces based on micropillar deflections. The developed micropillar system is capable of measuring the force with sub-micron resolution while providing a continuous force output spectrum.

ACKNOWLEDGEMENTS

The journey undertaken in completing the research presented in this thesis has been challenging and immensely rewarding. This is due in no small part to a number of individuals whom I would like to acknowledge and thank for their contributions.

Firstly, I would like to express my gratitude to my research supervisors, Professor XiaoQi Chen, Dr Wenhui Wang, Professor J. Geoffrey Chase and Dr Chris E. Hann for their support and guidance throughout my PhD candidature. I would like to extend special thanks to my senior supervisor, Professor XiaoQi Chen, for his continued support and to my co-supervisor Dr Wenhui Wang who introduced me to the wonderful world of bio-micromanipulation.

I would also like to express special gratitude and appreciation to Professor Saeid Nahavandi and Dr Ben Horan for their generous support, contribution and guidance and the invaluable opportunity to be hosted within the Center for Intelligent Systems Research at Deakin University.

My thanks also go to Dr Volker Nock and Dr Hamid Abdi with whom I had the pleasure of collaboration during my PhD research and to Julian Murphy for his technical assistance at the Mechatronics Research Laboratory at the University of Canterbury.

I would like to acknowledge the financial support provided to me by the University of Canterbury through the UC doctoral scholarship, departmental premier PhD scholarship, operational research fund and conference attendance grant. Without this support, this thesis would not be possible.

Finally, to my family, my parents Batool and Hossein, my brother Saeed, and my sisters Saeedeh and Vahideh for their endless love and support.

CONTENTS

LIST OF FIGURES

LIST OF TABLES

NOMENCLATURE

Nomenclature used in this thesis is listed here for easy reference.

AFM	Atomic Force Microscopy
ANFIS	Adaptive Neuro Fuzzy Inference System
ANN	Artificial Neural Network
API	Application Programming Interface
BEM	Boundary Element Method
C. elegans	Caenorhabditis elegans
CDF	Cumulative Distribution Function
CMOS	Complementary Metal–Oxide–Semiconductor
CPU	Central Processing Unit
CS	Cross Sections
DAQ	Data Acquisition
DEM	Discrete Element Method
D-H	Denavit-Hartenberg

DI	Deionized
DNA	Deoxyribonucleic acid
DOF	Degree of Freedom
FEM	Finite Element Method
FIS	Fuzzy Inference System
FRVF	Forbidden-Region Virtual Fixture
GUI	Graphical User Interface
GVF	Guidance Virtual Fixture
IPA	Isopropyl Alcohol
HIP	Haptic Interaction Point
LSCD	Least-Squares circle Detection
LSE	Least Squares Estimate
MEMS	Microelectromechanical System
MF	Membership Function
MPO	Maximum Percent Overshoot
MSD	Mass-Spring-Damper
NF	Neuro Fuzzy
NFS	Neuro Fuzzy System
NGM	Nematode Growth Medium
NI	National Instrument
PC	Personal Computer
PDMS	Polydimethylsiloxane
PID	Proportional Integral Derivative
PVDF	Polyvinylidene Fluoride
RAM	Random Access Memory
RMSE	Root Mean Square Error
RNA	Ribonucleic acid
SEM	Scanning Electron Microscope

TMCS	Trimethylchlorosilane
VF	Virtual Fixture
ZN	Ziegler-Nichols
1D	1 Dimensional
2D	2 Dimensional
3D	3 Dimensional

"Twenty years from now you will be more disappointed by the things that you didn't do than by the ones you did do. So throw off the bowlines. Sail away from the safe harbor. Catch the trade winds in your sails. Explore. Dream. Discover."

Mark Twain
1835-1910, American writer

Chapter 1

INTRODUCTION

1.1 OVERVIEW AND OBJECTIVES

The field of developmental biology includes embryonic development, cancer research and neurobiology and requires a diverse range of micromanipulation operations. These operations range from cell level subunits such as organelles, embryos and egg cells, to whole organisms such as Drosophila*, C. elegans* and zebra fish.

Bio-micromanipulation is by its nature highly interdisciplinary involving disciplines ranging from biology to engineering. Typical biomanipulation tasks include separation, transportation, positioning, measurement and visualization. To achieve such tasks requires specific

technologies able to achieve high precision and/or speed, teleoperation, specific sensory systems, visual and/or force feedback. Research into bio-micromanipulation can broadly be categorized into the following areas: *observation, actuation, measurement, physical phenomena and scaling issues, microfarbrication, calibration, control, transportation, alignment, and fixation, communication and, human-machine interfacing* [1].

Typically, bio-micromanipulation tasks require real-time decision making and flexibility and for this reason are generally not well suited to system autonomy. In contrast, manually performed operations are limited by the capabilities of the bio-operator which can include human-level response time, precision and repeatability. One approach to enhancing bio-micromanipulation is to focus on improving the bio-operators performance. This can be achieved through the integration of technologies able to provide useful information and guidance for bio-micromanipulation. Such technologies include sensory systems for measurement, algorithms for processing and providing information, and human machine interfaces for providing real-time feedback to the bio-operator.

This thesis investigates force interaction and sensing as two distinctive challenges in the bio-micromanipulation research field. To this end, this thesis discusses the design, development and evaluation of a novel haptically enabled microrobotic cell injection system which haptically assists bio-operators during cell injection. The microfabrication, development and testing of a first-of its-kind micro-pillar based on-chip system for dynamic force measurement of *C. elegans* in motion is also presented.

1.2 THESIS CONTRIBUTIONS

The main contributions of this thesis can be summarized as follows:

- *Haptically Enabled Microrobotic Cell Injection System* [2]

1. *Haptic Mapping framework* [3]. As the basis for utilizing haptic interaction in intercellular injection, the haptic kinematic mapping framework is proposed. In order to develop such a framework, micromanipulator and haptic interface kinematics analysis, bilateral mapping workspace, scaling factors, tracking delay and system resolution are addressed. The novelty of such an approach lies in the provision of an intuitive method for controlling the micropipette with direct 3D position-to-position mapping from the haptic device. This provides the necessary foundation to introduce intuitive haptic feedback/assistance directly to 3D space as well as the ability to control the motion of the micropipette in a similar fashion to conventional handheld needle insertion.

2. *Adaptive neuro-fuzzy modeling and control* [4]. an ANFIS-based system identification and control scheme is developed to identify the nonlinear micromanipulator system models with high accuracy and achieving adequate control of the micromanipulator using haptic device in fine and coarse modes.

3. *Haptic guidance* [5]. Task specific haptic virtual fixtures (planar, axial and volumetric) are introduced to assist the bio-operator while performing the cell injection operation. Three novel volumetric (cone [5], paraboloid [6] and neiloid) force field virtual fixtures based on potential field multi-charged particle system models for

haptically guiding the bio-operator are introduced. This includes approaching and penetrating the biological cell at the desired location. The performance of haptic vitual fixtures are then evaluated. Vision-based sensing is utilized to obtain the cell parameters necessary to realize the virtual fixtures. The proposed virtual fixtures could be used as a training aid in a virtual environment, or are equally valid for real-time haptic guidance.

- *Micropillar-based on-chip system for automated force measurment of C. elegans in motion* [7]

4. *Micropillar-based on-chip system* [8]. A novel Polydimethylsiloxane (PDMS) device is microfabricated to allow *C. elegans* to move in a matrix of micropillars in a channel in the aim of quantifying multi-point locomotive forces of a moving *C. elegans*. Two different pillar array layouts were integrated on the device to investigate their suitability for use with *C. elegans*.

5. *Automated visual tracking algorithm* [9] *and force inference model* [10]. A force-deflection model of the micropillars resolving *C. elegans* force from the defecting micropillars based on microscopy computer vision is developed [10]. An image processing algorithm has also been introduced which tracks *C. elegans* and contact micropillars and accurately measures the deflections all automatically [9]. The developed on-chip system is cablable of quantifying multi-point locomotive forces of a moving *C. elegans* with sub-micron accuracy while having a continuous force output spectrum.

The following peer reviewed publications have been resulted from this thesis:

- **A. Ghanbari**, B. Horan, S. Nahavandi, X. Chen, and W. Wang, "Haptic Microrobotic Cell Injection System", *IEEE Systems Journal, (2012),* Issue: 99, DOI: 10.1109/JSYST.2012.2206440.

- **A. Ghanbari**, V. Nock, S. Johari, R. Blaikie, X. Chen, and W. Wang, " A Micropillar-based On-chip System for Continuous Force Measurement of *C. elegans*", *Journal of Micromechanics and Microengineering (2012),* Vol. 22. No. 9, pp. 1-10, DOI: 10.1088/0960-1317/22/9/095009.

- **A. Ghanbari**, X. Chen and W. Wang, "Intelligent Precision Control for Haptic Microrobotic Cell Injection System", *Proceedings of ACRA (2011).*

- **A. Ghanbari**, V. Nock, R.J. Blaikie, J.G. Chase, X. Chen, C.E. Hann, and W. Wang, "Force Pattern Characterization of Caenorhabditis elegans in Motion", *Journal of IJCAT (2010),* Vol. 39, No.1/2/3 pp. 137 - 144, DOI: 10.1504/IJCAT.2010.034742.

- **A. Ghanbari**, X. Chen, W. Wang, B. Horan, H. Abdi, and S. Nahavandi, "Haptic Microrobotic Intracellular Injection Assistance using Virtual Fixtures", *Proceedings of ICARCV (2010),* pp. 781 - 786, DOI: 10.1109/ICARCV.2010.5707390.

- **A. Ghanbari**, V. Nock, R.J. Blaikie, X. Chen, J.G. Chase, and W. Wang, "Automated Vision-Based Force Measurement of Moving *C. elegans*", *Proceedings of IEEE CASE (2010),* pp. 198 - 203, DOI: 10.1109/COASE.2010.5584225.

- **A. Ghanbari**, H. Abdi, B. Horan, S. Nahavandi, X. Chen, and W. Wang, "Haptic Guidance for Microrobotic Intracellular Injection", *Proceedings of IEEE BIOROB (2009),* pp. 162 - 167, DOI: 10.1109/BIOROB.2010.5627016.

- **A. Ghanbari**, X. Chen, and W. Wang, "Neuro-Fuzzy Microrobotic System Identification for Haptic Intracellular Injection", *Proceedings of IEEE ICCA (2009)*, pp. 860 - 866, DOI: 10.1109/ICCA.2009.5410444.

- **A. Ghanbari**, B. Horan, S. Nahavandi, X. Chen, and W. Wang, "Towards Haptic Microrobotic Intracellular Injection", *Proceedings of ASME/IEEE MESA (2009),* pp. 135-142, DOI: 10.1115/DETC2009-87822.

- **A. Ghanbari**, W. Wang, C.E. Hann, J.G. Chase, and X. Chen, "Cell Image Recognition and Visual Servo Control for Automated Cell Injection", *Proceedings of ICARA (2009),* pp. 92-96, DOI: 10.1109/ICARA.2000.4803986.

- **A. Ghanbari**, V. Nock, W. Wang, R.J. Blaikie, J.G. Chase, X. Chen, and C.E. Hann, " Force Pattern Characterization of *C. elegans* in Motion*", Proceedings of M2VIP (2008),* pp. 634 - 639, DOI: 10.1109/MMVIP.2008.4749604.

- S. Faramarzi, **A. Ghanbari**, X. Chen, and W. Wang, "A PVDF Based 3D Force Sensor for Micro and Nano Manipulation", *Proceedings of IEEE ICCA (2009),* pp. 867-871, DOI: 10.1109/ICCA.2009.5410237.

- M. Asgari, **A. Ghanbari**, S. Nahavandi and X. Chen, "3D Particle-Based Cell Modelling for Haptic Microrobotic Cell Injection", *Proceedings of ICMT (2011).*

- B. Horan, D. Lowe, Q. Ang, M. Asgari, **A. Ghanbari**, and S. Nahavandi, "Virtual Haptic Cell Model for Operator Training", *Proceedings of ICMT (2011).*

The work described in this thesis has also been partially presented in the following conferences and seminars in various forms:

- Oral presentation, "Force Interaction and Sensing in Bio-micromanipulation", *Departmental Seminar, Mechanical Engineering, University of Canterbury, Christchurch, New Zealand, 19 October, 2012.*

- Oral presentation, "Intelligent Precision Control for Haptic Microrobotic Cell Injection System", *Australasian Conference on Robotics and Automation, Melbourne, Australia, 7-9 December, 2011.*

- Oral presentation, "Virtual Haptic Cell Model for Operator Training", *The 15th International Conference on Mechatronics Technology, Melbourne, Australia, 30 November to 2 December, 2011.*

- Oral presentation, "3D Particle-Based Cell Modelling for Haptic Microrobotic Cell Injection", *The 15th International Conference on Mechatronics Technology, Melbourne, Australia, 30 November to 2 December, 2011.*

- Oral presentation, "Micropillar-Based On-Chip System for Force Pattern Analysis in *C. elegans* Locomotion", *Centre for Intelligent Systems Research (CISR) Seminar Series, Waurn Ponds, Victoria, Australia, 18 April, 2011.*

- Oral presentation, "Force Field Virtual Fixtures for Microrobotic Cell Injection", *Departmental Seminar, Mechanical Engineering, University of Canterbury, Christchurch, New Zealand, 17 December, 2010.*

- Poster presentation, "Haptic Microrobotic Intracellular Injection Assistance using Virtual Fixtures", *The 11th International Conference on Control, Automation, Robotics and Vision, Singapore, 7-10 December 2010.*

- Oral presentation, "Haptic Guidance for Microrobotic Intracellular Injection" *The Geelong Innovation Forum, Geelong, Victoria, Australia, 1-2 November, 2010.*

- Oral presentation, "Automated Vision-Based Force Measurement of Moving *C. elegans*", *IEEE Conference on Automation Science and*

Engineering, Toronto, Canada, 21-24 August, 2010 (Thorlabs best student paper finalist's award).

- Poster presentation, "Automated Vision-Based Force Measurement of Moving *C. elegans*", *IEEE Conference on Automation Science and Engineering, Toronto, Canada, 21-24 August, 2010* (Thorlabs best student poster finalist's award).

- Oral presentation, "Haptic Guidance for Microrobotic Intracellular Injection", *IEEE International Conference on Biomedical Robotics and Biomechatronics, Tokyo, Japan, 26-29 September, 2010.*

- Oral presentation, "Haptic Guidance for Microrobotic Intracellular Injection", *Institute for Technology Research and Innovation (ITRI) Seminar Series, Waurn Ponds, Victoria, Australia, 23 July 2010.*

- Oral presentation, "Force Pattern Characterization of *C. elegans* in Motion", *Centre for Intelligent Systems Research (CISR) Seminar Series, Waurn Ponds, Victoria, Australia, 29 April, 2010.*

- Oral presentation, "Neuro-Fuzzy Microrobotic System Identification for Haptic Intracellular Injection", *IEEE International Conference on Control and Automation, Christchurch, New Zealand, 9-11 December, 2009.*

- Oral presentation, "A PVDF Based 3D Force Sensor for Micro and Nano Manipulation", *IEEE International Conference on Control and Automation, Christchurch, New Zealand, 9-11 December, 2009.*

- Oral presentation, "Neuro-Fuzzy Microrobotic System Identification for Haptic Intracellular Injection", *Centre for Intelligent Systems Research (CISR) Seminar Series, Waurn Ponds, Victoria, Australia, 15 October, 2009.*

- Oral presentation, "Towards Haptic Microrobotic intracellular Injection", *ASME/IEEE International Conference on Mechatronic and*

Embedded Systems and Applications, San Diego, California, USA, 30 August - 2 September, 2009.

- Oral presentation, "Towards Haptic Microrobotic Intracellular Injection", *Departmental Seminar, Mechanical Engineering, University of Canterbury, Christchurch, New Zealand, 20 August 2009.*

- Oral presentation, "Force Pattern Characterization of *C. elegans* in Motion", *The 15th International Conference on Mechatronics and Machine Vision in Practice, Auckland, New Zealand, 2 - 4 December, 2008.*

- Oral presentation, "Cell Image Recognition and Visual Servo Control for Automated Cell Injection", *The 4th International Conference on Autonomous Robots and Agents, Wellington, New Zealand, 10-12 February 2009.*

- Oral presentation, "Haptic Procedural Operator Training for Biological Cell Injection", *Departmental Seminar, Mechanical Engineering, University of Canterbury, Christchurch, New Zealand, 19 November 2008.*

The work presented in this thesis has further been partially reported in the following non-peer reviewed form:

- *"Microrobotic Cell Injection with Haptic Guidance", Proceedings of ITRI Annual Conference (2010).*

1.3 THESIS STRUCTURE

The roadmap to this thesis is presented below:

Chapter 2 - *Background* presents the background research and motivation of the thesis. Challenging problems in bio-micromanipulation are discussed and force interaction and visual measurement are identified as important research areas. More specifically the challenges related to

biological cell microinjection operation and the force measurement of moving *C. elegans* are discussed.

Chapter 3 - *Haptic Microrobotic Cell Injection System* introduces a novel approach which integrates the bio-operator's haptic sensory modality offering immense benefits over conventional techniques. The high level architecture of the proposing haptic cell injection system is discussed. It investigates haptic bilateralism and introduces a kinematic mapping framework. This offers an intuitive method allowing the bio-operator to maneuver the micropipette in a manner similar to handheld needle insertion. The Chapter then demonstrates experimental position-to-position mapping framework performance of the developed system in different modes and scaling factors.

Chapter 4 - *Neuro-Fuzzy Modelling and Control* discusses the intelligent system identification and control approach taken to achieve adequate control of the micromanipulator using a haptic device. The Chapter discusses the ANFIS modeling process and direct inverse learning approach used to design the intelligent controller. It demonstrates that the developed ANFIS model and controller can achieve micron accuracy while the micromanipulator moves within cm range.

Chapter 5 - *Haptic Guidance* introduces task specific haptic virtual fixtures (planar, axial and volumetric). It assists the bio-operator while performing the cell injection task. This Chapter also addresses three novel volumetric (paraboloid, cone and neiloid) force field virtual fixtures. The virtual fixtures are based on potential field multi-charged particle system models. The introduced haptic virtual fixtures haptically guide the bio-operator in approaching and penetrating at the desired location on the

biological cell, and stopping at the deposition target inside it. The Chapter then demonstrates performance evaluation of the proposed force field virtual fixtures and compares their functionality.

Chapter 6 - *Micropillar-based On-chip System for Dynamic Force Measurement of C. elegans* introduces a novel micropillar-based PDMS device for quantifying multi-point locomotive forces of moving *C. elegans*. It discusses the device layout, microfabrication process, the force-deflection model of the micropillar, force resolution and the micropillar deflection visual tracking technique. The Chapter concludes by demonstrating experimental measurement results and analysis.

Chapter 7 - *Automated Vision-Based Measurement of Moving C. elegans* extends the on-chip system discussed in Chapter 6 and introduces an image processing algorithm capable of tracking *C. elegans* and the contact micropillars. The algorithm is able to accurately measure all deflections automatically. The developed automated on-chip system is cablable of quantifying multi-point locomotive forces of moving *C. elegans* with sub-micron accuracy while having a continuous force output spectrum in large quantity. This Chapter concludes by discussing *C.elegans* locomotion behaviour based on the observation obtained.

A summary of the work presented in this thesis is provided in **Chapter 8** - *Conclusion and Future Directions*, as are recommendations for future research.

"Anyone who has never made a mistake has never tried anything new."

Albert Einstein
1879-1955, German-born physicist

Chapter 2

BACKGROUND

This thesis investigates force interaction and visual measurement as two challenging problems in bio-micromanipulation. This Chapter discusses the background research and motivation, in particular, the challenges relating to biological cell microinjection and force measurement of *C. elegans* as a micro-scale multicellular nematode.

2.1 BIOLOGICAL CELL MICROINJECTION

Many diseases originate from single pathological cells. Accordingly, molecule screening at the single cell level is critical in molecular biology and drug discovery. This requires that target molecules be introduced into single cells to permit cellular-function-targeted molecules monitoring and quantifying of directly regulation, cell development and their functions. For that reason, the ability to manipulate individual biological cells is the

subject of an increasing research interest. Particularly, by depositing of certain amount of materials such as protein, sperm, DNA and bio-molecules into the specific locations of biological cells and observing the implications of these foreign materials, researchers are able to monitor effect of materials and drugs at cell level [11-13]. For example, nucleic acid based molecules such as short interfering RNA (siRNA) and antisense oligonucleotides (AS-ON), which inhibit cancer-related gene expression, need to be delivered into cancer cells to evaluate their effectiveness [14]. As another example, it has been discovered, by introducing the four genes of *OCT4*, *SOX2*, *NANOG*, and *LIN28* into human somatic cells, that these genes are sufficient to reprogram these cells to pluripotent stem cells. Thus, they represent the essential characteristics of embryonic stem cells [15].

In the literature, different techniques have been reported for cellular drug delivery. Broadly, these techniques can be categorized into non-contact and contact methods. Non-contact methods include ultrasound [16], electroporation [17] and nanovector-based delivery [18] and contact methods include mechanical microinjection [19-20]. Mechanical microinjection uses a single glass micropipette to manipulate cells and deposit materials. It has proven effectiveness for delivering macromolecules with high cell viability. This approach has lower rates of cell waste and damage as well as providing the flexibility of handling a diverse range of cells [21].

Cells to be injected have different mechanical properties including shape, size (in range of μm to mm) and contact and penetration forces (in range of μN to mN) [22]. Typically, the injection targets are embryos/oocytes of model organisms. Zebrafish and mouse cells are two

widely utilized models for studying vertebrate development, genetics, and reproduction [23-24]. Figure 2.1 shows the structure of a zebrafish embryo. The Zebrafish has major organs similar to humans and has emerged as an important model organism in genetic research and drug discovery. In addition, given its external fertilization and development, short development period, and transparency of embryos, the fate of individual cells during development can be conveniently observed [16]. The size varies from ~600 μm to ~1.2 mm including chorion. Zebrafish embryos have a delicate structure and if an inappropriate force or penetrating speed is exerted damage can easily occur.

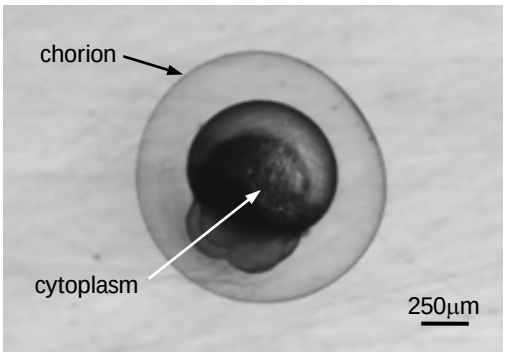

Figure 2.1 The structure of a zebrafish embryo

Conventionally, the cell injection task is performed manually by a trained bio-operator in a laboratory. Successful manual microinjection is highly dependent on being able to properly deal with the mechanical properties and constraints of the cell. Successful cell injection can be characterized by metrics including accuracy, speed and trajectory [25]. Research suggests that it takes approximately one year to adequately train an operator in the cell injection process and despite this, success rates remain low [26-27]. The reason is, in manual cell injection, the bio-operator remains limited to its visual sense for task feedback through the microscope or displayed on a monitor. Furthermore, it is often difficult for

the bio-operator to adequately perceive the microscale environment and conduct a successful micro-operation with high precision.

2.1.1 MICROROBOTIC CELL INJECTION

In the literature, approaches have been reported which utilize robotics to facilitate the cell injection operation. Broadly, two classes of microrobotic cell injection systems have been proposed, namely; a) microrobot-assisted or teleoperated systems and b) fully autonomous systems.

2.1.1.1 Teleoperated Microinjection

For teleoperated systems, the bio-operator conducts the cell injection operation by controlling the micromanipulators/microrobots in a human-in-loop scenario [28-32].

The work reported in [33-35] has developed an interface platform for teleoperation of a commercial bio-manipulation equipment integrated with a game joystick. Furthermore, a GUI (graphical user interface) is designed to allow direct configuration and control of all system devices. This GUI also includes utilities designed to speed up repetitive tasks.

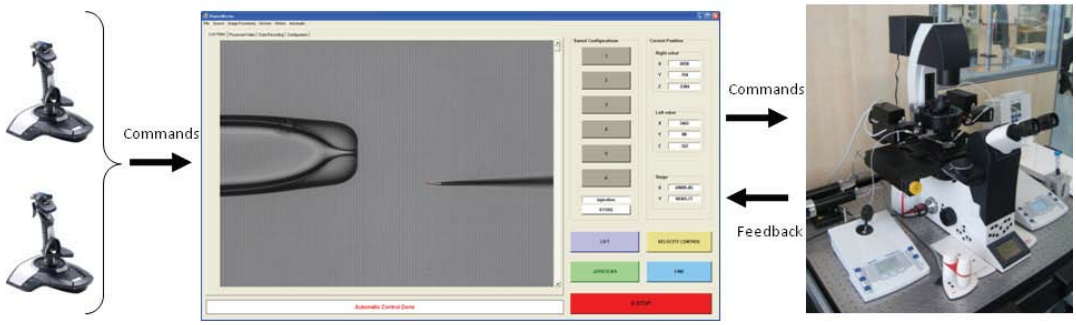

Figure 2.2 Teleoperated biomanipulation system introduced in [33].

Figure 2.2 demonstrates the system proposed for such a teleoperation platform. The joystick generates commands which are processed by the interface computer and sent to the micromanipulator. At the same time, a live video stream and other positioning signals are sent back to the computer for processing and display via the GUI. One disadvantage of such an approach is that the use of the joystick may not be intuitive. Control of the micropipette for cell injection using the joystick requires different skills than handheld needle insertion. Consequently, the expertise and skill of a trained bio-operator is not convenient for such a system.

The work presented in [36] reports a macro–micro teleoperation system using a piezoelectric actuator as the slave manipulator. The proposed system uses position to force mapping in a master/slave architecture. In this configuration, the master sends its position and velocity to slave, and the slave sends the force imposed on it to the master. Figure y depicts the micromanipulation master/slave architecture. A micro-positioning stage and a DC-servo are utilized as the master and the slave respectively (Figure 2.3).

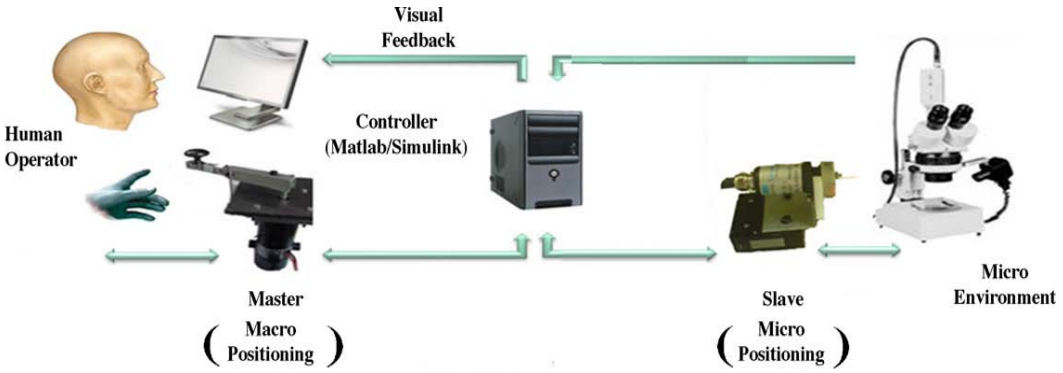

Figure 2.3 Master/slave architecture of macro–micro teleoperation system proposed in [36].

To compensate for the hysteresis of the piezoelectric actuator, an inverse model-based feed forward controller is proposed. Also, rather than using force sensors, sliding mode unknown input observers are utilized to estimate the human and environmental forces. The adaptive sliding mode control scheme is responsible for dealing with the adverse effects of parametric uncertainties and to ensure perfect position tracking and accurate force estimation. The main contribution of the paper is the adaptation law at the slave side which eliminates parametric uncertainty and operation despite force sensors. While the proposed design is novel and interesting from a control design point of view, it is limited to 1-DOF systems.

Teleoperated microinjection is able to enhance the cell injection operation to a certain extent given the reduced human involvement in directly performing the microinjection task. The performance of such a system is dependent on factors such as the master/slave feedback information (position, force, vision ...), resolution, motion mapping strategy and time delay.

2.1.1.2 Autonomous Microinjection

In the aim of increasing the success rate of the cell injection operation, several researchers have eliminated the human in the loop and proposed fully autonomous cell injection systems [19, 25, 37-38].

The work by [25] proposes an autonomous system for the injection of mouse embryos. A microrobotic system was developed capable of performing autonomous embryo pronuclei DNA injection. The system employed a hybrid visual-servo-control scheme, a high precision 3-DOF

microrobot to move the injection pipette, and a coarse manipulator to position the holding pipette (Figure 2.4).

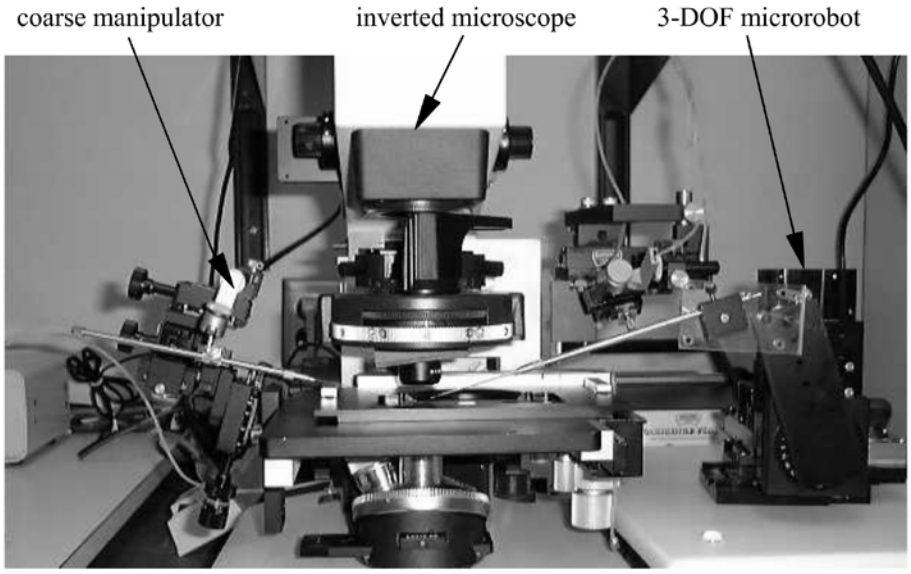

Figure 2.4 Autonomous mouse embryo injection system reported in [25].

Image processing is utilized to determine necessary cell parameters including the location of the cell nucleus and micropipette tip. The approach offers the benefits inherent to system autonomy and reduces the real-time involvement of the human operator.

Using "looking-then-moving" control scheme, a high-throughput automated system for zebrafish embryo injection is presented in [19]. Two 3-DOF microrobots are employed to position the embryo holding device and micropipette in parallel (Figure 2.5). Motion control of both microrobots is based on position feedback using a PID (proportional integral derivative) control law. An image processing algorithm is developed to identify target positions, and then the controller moves the microrobots to reach the target. This makes it a "looking-then-moving" system.

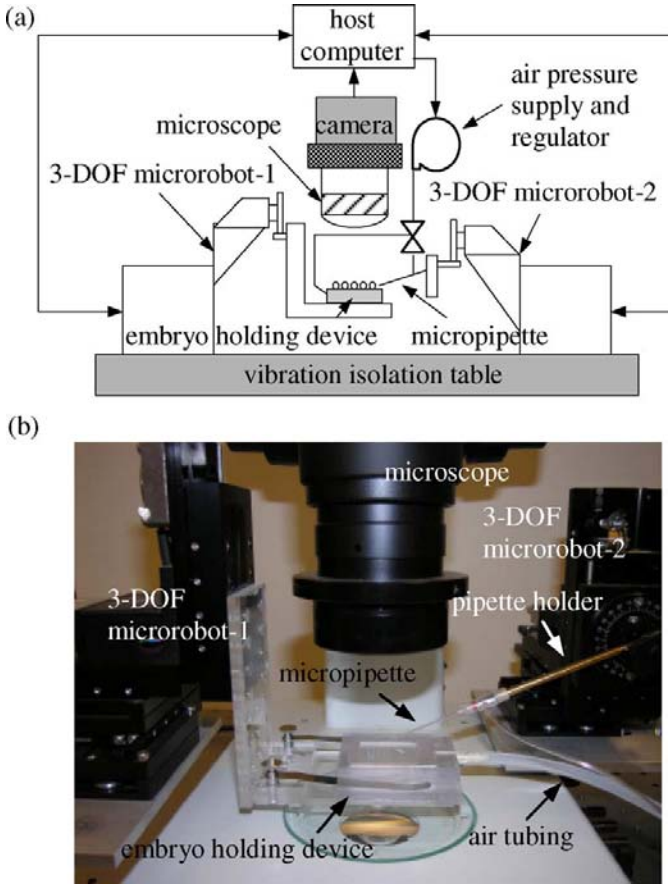

Figure 2.5 Automated zebrafish embryo injection system reported in [19]. (a) Schematic of the cell injection system architecture. (b) A picture of the actual setup.

An automated high-throughput Drosophila embryo injection system is reported in [39]. A single surface micromachined MEMS (microelectromechanical system) needle is used as an injector and two motorized xyz-stages move relative to each other for positioning (Figure 2.6). One stage carries embryos and the second is fitted with the microinjector chip. Using a similar principle and in order to achieve high-throughput parallel cell injection, the works reported in [40-44] present MEMS-based microneedle arrays.

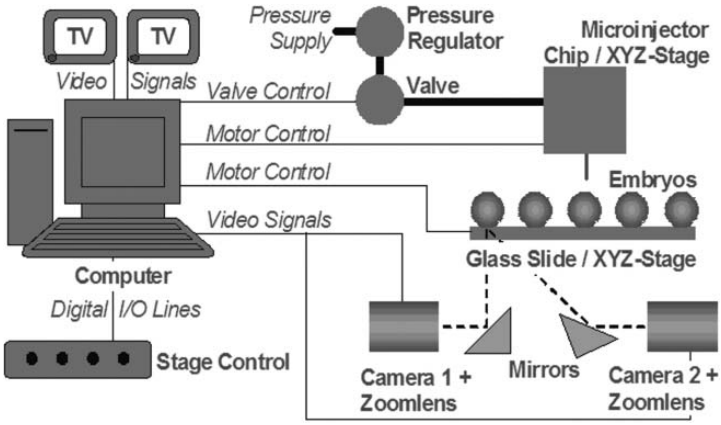

(a)

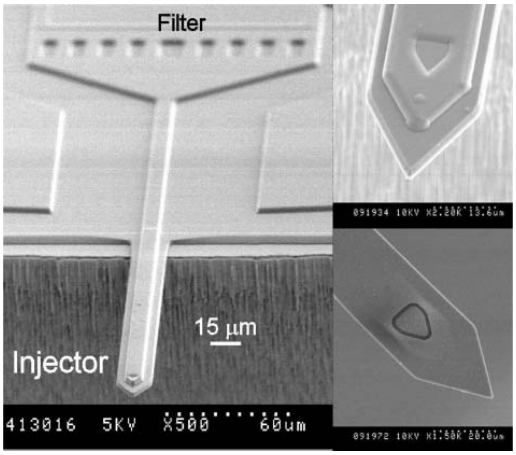

(b)

Figure 2.6 Automated MEMS-based Drosophila embryo injection system presented in [39]. (a) The overview of system architecture. (b) SEM images of the injector and close-ups of back and front side of the needle tip.

The drawback of these systems is the manual alignment of the injector and glass slide which can result in alignment errors. Such errors greatly influence injection performance. Also, given the low stiffness of the MEMS injector, the chorion (the outer membrane) needs to be removed before injection is conducted.

Autonomous systems may prove valuable in applications where complete knowledge of the cell is known and high-throughput cell injection is desirable. However, given the diversity of biological cells,

achieving autonomous intracellular injection presents distinct challenges in determining the required cell parameters.

2.1.2 HAPTIC MICROINJECTION

Haptics relates the sense of touch and feel and the term *haptic* originates from the Greek word *haptesthai* meaning to "contact" or "touch" [45]. Haptic related technologies provide a system with the ability to replicate the sense of touch to a user. A diverse body of research has investigated interaction with the human's haptic modality. Haptic technology offers wide reaching implications across many applications domains. Such research areas include haptic artwork [46], virtual museum exploration [47], procedural operator training [48], mobile robotic teleoperation [49-51] and medical simulation and training [52-55].

The ability to interact with the human operator's haptic modalities can contribute to achieving intuitive HMI (human-machine-interfaces) in a human-in-the-loop scheme. The ability to determine the force between the micropipette and the cell has been the focus of several recent works. Some researchers have also proposed the haptic display of measured force in real-time [18-21, 56]. The work presented in [57] proposes a vision-based system to measure cell injection forces using a polydimethylsiloxane (PDMS) sensor. Based on visually tracking of the deflections of the elastic low-stiffness PDMS supporting posts the imposed force of zebrafish embryos are obtained (Figure 2.7). An analytical mechanics model defines the relation of imposed force and deflection of posts.

An alternative approach is to utilize vision-based sensing and an appropriate cell model to determine cell injection forces.

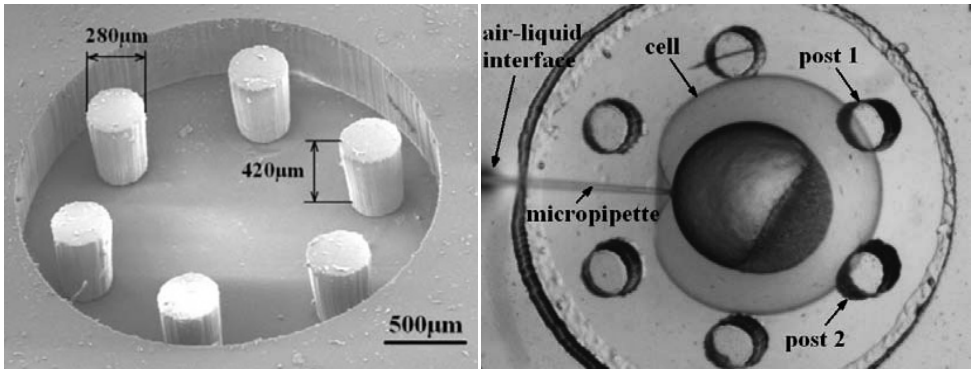

(a) (b)

Figure 2.7 PDMS cell holding device reported in [57]. (a) SEM image of the fabricated device. (b) Indentation forces applied by the micropipette cause the two supporting posts to deflect.

The work by [58] employs vision and a non-linear MSD-based (mass-spring-damper) cell model to estimate the force being exerted on the cell membrane during injection. The work also develops a FEM-based (finite element method) model of a mouse oocyte ZP. This model is then utilized to identify the parameters of proposed MSD-based cell model (Figure 2.8). The calculated force is then haptically displayed to the operator. The work

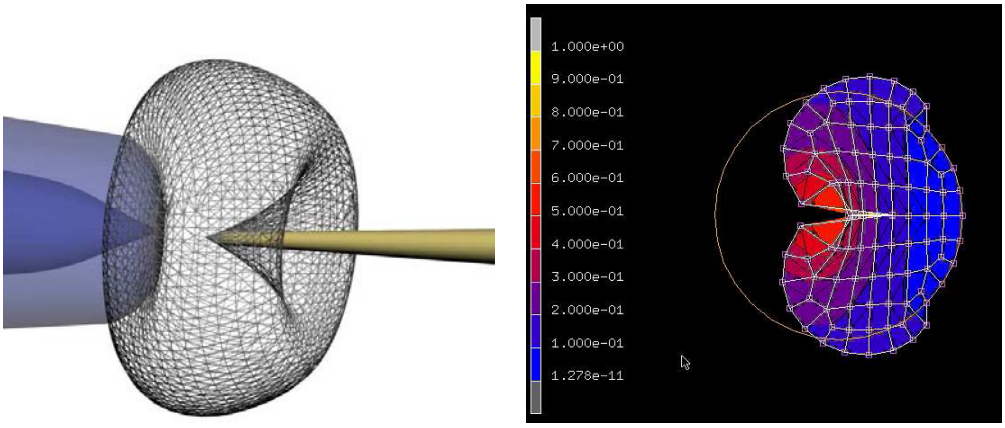

(a) (b)

Figure 2.8 Cell models response in injection operation introduced in [58]. (a) Mesh of MSD-based cell model. (b) FEM-based cell model.

demonstrates the ability of such haptic feedback to reduce the time taken to perform intracellular injection.

A similar approach is presented in [59] where vision-based sensing and a BEM-based (Boundary Element Method) model are utilized to determine the cell contact force which is haptically displayed to the operator (Figure 2.9). Unlike MSD-based models, the BEM-based model uses material parameters directly and is able to handle various interactions between micropipette and cell.

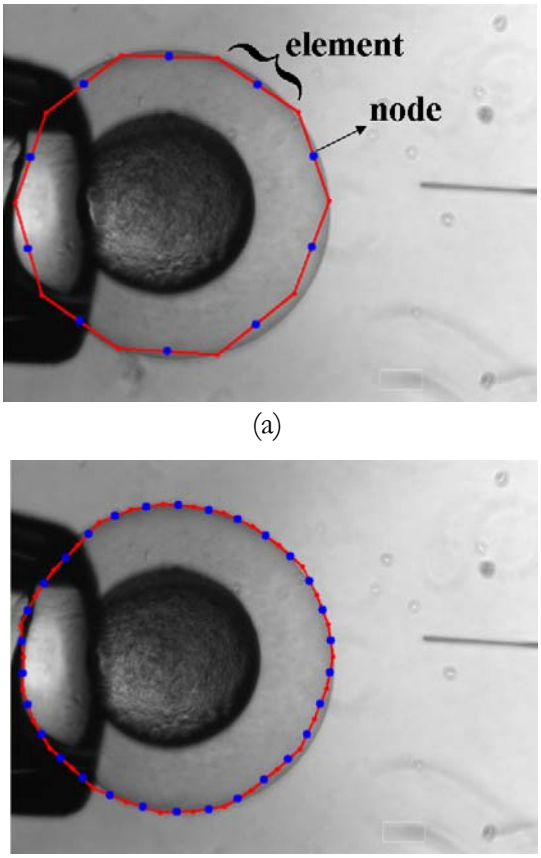

(a)

(b)

Figure 2.9 Two-dimensional BEM-based model proposed in [59] with line elements for (a) 10 nodes (b) and 30 nodes.

The limitation of such vision-based force estimation techniques is that they relay on the availability of appropriate cell-specific models. This is

problematic because the relationship between the geometrical and mechanical properties of cells remains largely unknown and there is no universal model to represent the relationship of cell mechanical properties, deformation and imposed force/stress.

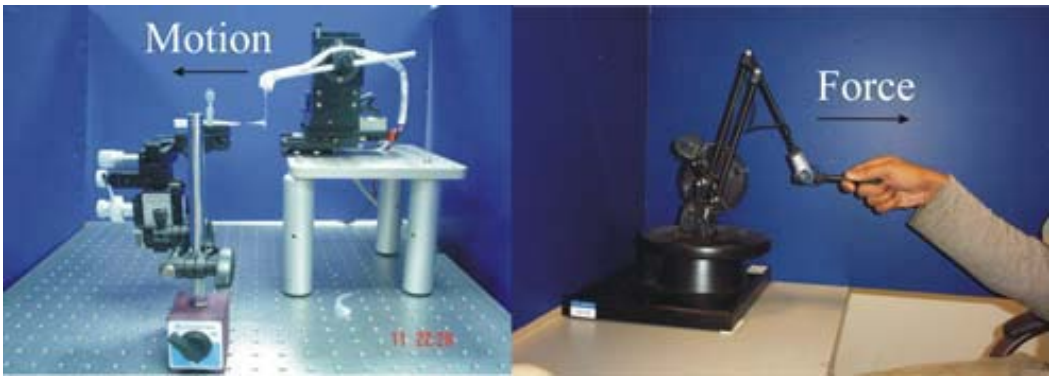

Figure 2.10 Force feedback interface for Cell Injection reported in [60]. A PVDF film is integrated with the micromanipulator and measured force is then feedback to the PHANToM haptic interface for display.

As another approach to measure the cell injection force, some works have proposed cantilever based force sensor structures using PVDF (Polyvinylidene fluoride) or piezoresistive materials [60-62]. In the work reported in [60], the micropipette is bonded to the free end of a PVDF-based cantilever. The cantilever base is mounted on the manipulator. Measured cell injection force is then displayed to the bio-operator hand through a haptic device in real-time (Figure 2.10).

Similar approach is taken in [37] to measure the force. The work presents a dynamic force-feedback system for automatic batch microinjection. In this system a machine vision algorithm is used to identify the number of embryos sorted in a batch; however, a piezoresistive micro-force sensor measures the penetration force (Figure 2.11). A position control strategy

with force feedback is used to control a positioning stage for batch injection.

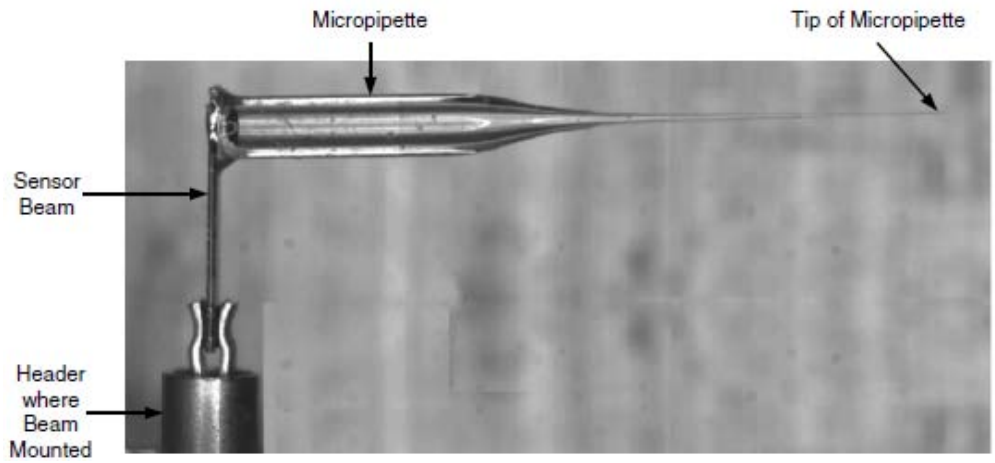

Figure 2.11 Cantilever based piezoresistive micro-force sensor reported in [37].

In practice, such sensor structures make it difficult to transfer the materials to be injected from the pressure tube to the micropipette. Furthermore, when the micropipette is connected to the pressure tube, the gravity of the pressure tube is far greater than the micro-Newton scale penetration force. The result is that the sensed signal is dominated by the measured gravity. This problem is overcome in [62] using a supported

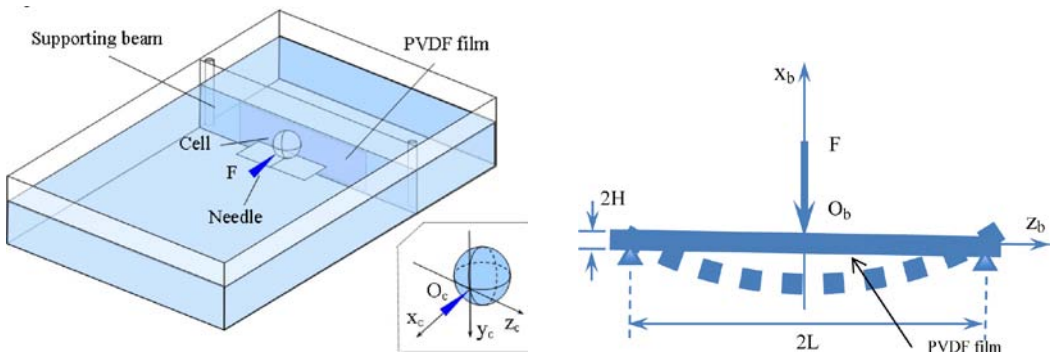

Figure 2.12 Force-sensing structure proposed in [62].

beam structure where a PVDF film senses the penetration force applied to the cell (Figure 2.12).

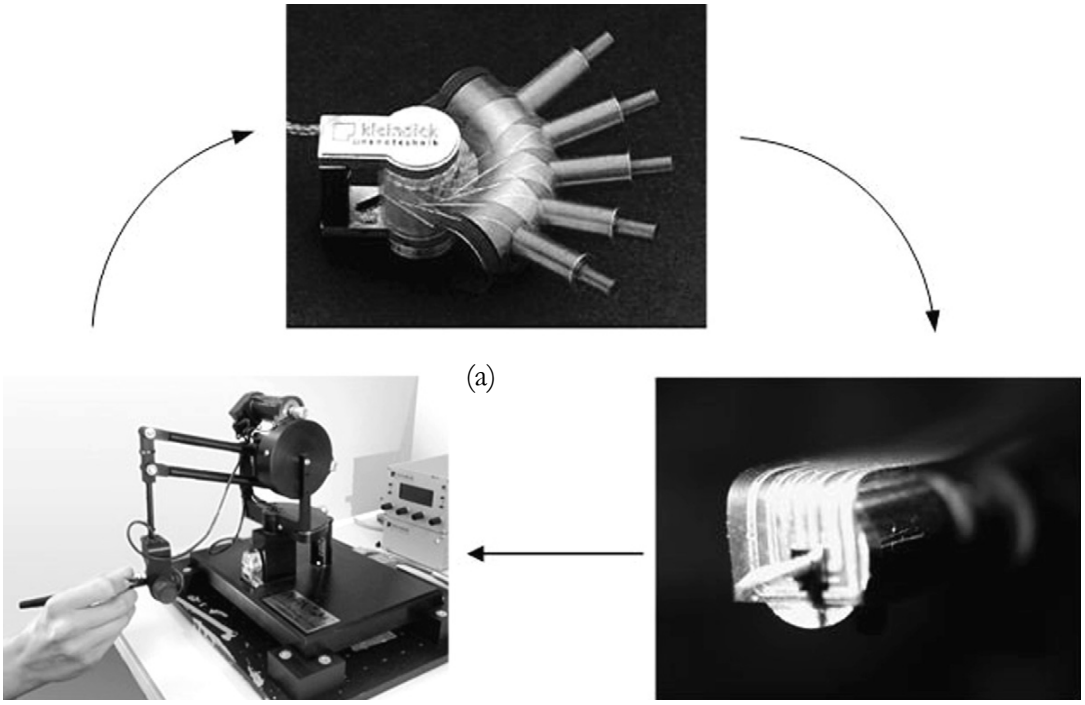

Figure 2.13 Biomanipulation platform with triaxial force feedback reported in [63]. (a) 3 DOF micromanipulator with subnanometric resolution. (b) Phantom haptic interface to provide the force feelling. (c) The triaxial force sensing device mounted onto an aluminum support.

An alternative to developing a force sensor is reported in [63] used MEMS (Microelectromechanical System) technology. The work presents a MEMS-based triaxial force sensing device which is mounted on a subnanometric resolution nanomanipulator with 3 DOF. The system is then integrated with a haptic input device allowing palpation and force feeling (Figure 2.13).

Utilizing AFM (atomic force microscopy) is another approach to measure the cell manipulation force reported in [64]. The work presents a haptic-enabled AFM system comprised of an AFM system to measure the force and a PHANToM haptic device to display it (Figure 2.14).

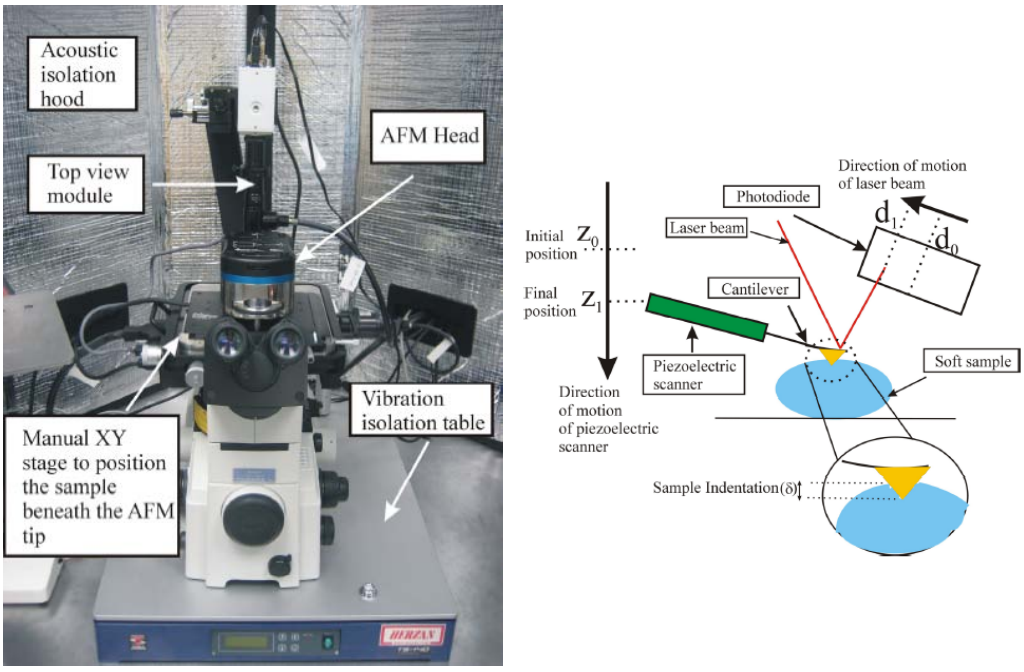

(a) (b)

Figure 2.14 Haptics-enabled AFM system proposed in [64]. (a) Experimental set-up. (b) Schematic of AFM cantilever interacting with a cell.

Given the micropipette as integral to cell injection operations, such MEMS-based and AFM-based works are not appropriate for cell force measurement. They do however remain useful for cell manipulation tasks such as poking, to investigate mechanical responses of cells, than injection operation.

The work in [65] takes one step further and utilizes the injection force to improve the controller performance rather than just displaying of it. It presents a vision-based impedance force control scheme for cell

injection. The control scheme is based on the dynamic modeling of a laboratory test-bed injection system. The injection force is first calibrated to derive the relationship between the force and cell deformation using the biomembrane point-load model [66]. Then a simplified relationship between the injection force and the injector displacement is derived for easy implementation (Figure 2.15). Using this estimated force, an impedance force control strategy is then proposed. The work demonstrates the effectiveness of the proposed impedance force control algorithm with capability of regulating the injection force during the cell injection.

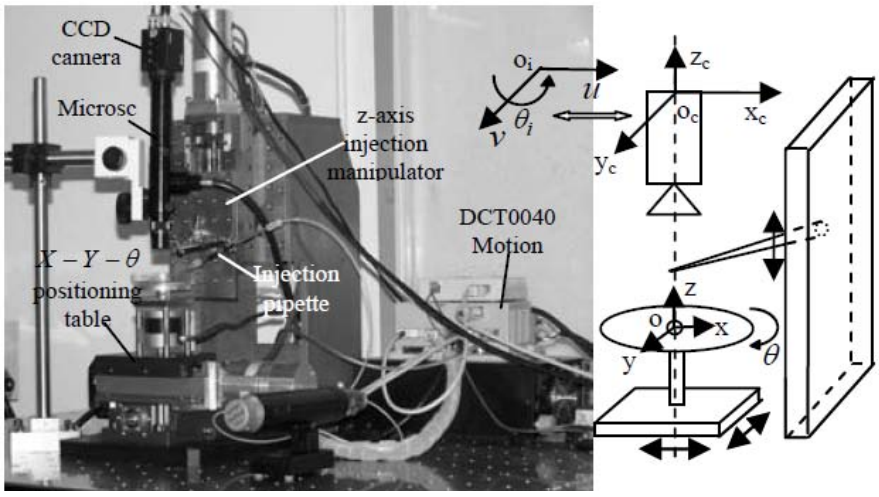

Figure 2.15 Vision-based impedance force control system presented in [65]. (a) Cell injection system laboratory test-bed. (b) Horizontal cell injection force calibration with cell biomembrane point-load model.

As discussed above, the majority of the ongoing research effort into haptic cell injection concentrates on the haptic display of the cell injection as measured using different techniques. It should be noted that passively presenting force information using this modality is not the advantage of haptic technology. It is the fundamentally bilateral nature of haptic technology which facilitates the operator to provide and receive information bilaterally and simultaneously. The capability to actively interact with haptically enabled interfaces obviously provides wide reaching advantages.

The aim of this thesis is not to replicate the research effort into the haptic display of cell injection forces but to address other haptic assistance for microrobotic cell injection. This includes; an understanding of bilateralism in haptics and the influence on the haptic device-micromanipulator mapping as well as resolution considerations, valuable haptic assistance other than cell injection forces and the ability to facilitate offline operator training.

The next section provides an overview of this thesis' second contribution to bio-micromanipulation.

2.2 VISION-BASED FORCE MEASUREMENT OF *C. ELEGANS* IN MOTION

Due to its relative simplicity in anatomy, Caenorhabditis elegans (*C. elegans*), a soil-dwelling multicellular eukaryotic nematode (Figure 2.16), is widely used as a model organism for studies in cellular differentiation, neural networking and molecular genetics. With a fully sequenced genome [67] and favourable gestation times, the semi-transparent *C. elegans* has

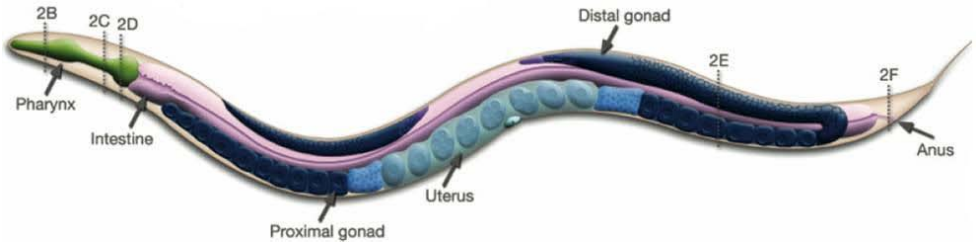

Figure 2.16 Structure of an adult hermaphrodite *C. elegans*, with the head facing toward the left (adapted from wormatlas.org).

been successfully established as an experimental genetic system regarding the relationship between genes and locomotive behavior [68-69]. In a normal environment, nematodes like *C. elegans,* exhibit a sinusoidal movement pattern provoked by waves of muscle contraction and local bending of the cuticle [70-71]. Changes in the locomotive behaviour of the nematodes can be induced by natural aging [72], structured environment [73], external exposure to toxins and drugs [74-76], or through the manipulation of specific genes [77-80].

Genetic modification in particular can be used to yield *C. elegans* mutants with different numbers of muscle arms, which are physical connections established between *C. elegans* muscles and the motor neurons via membrane extensions [81]. As muscle arms function as paths for muscles to receive stimulation from the nerve, their number is most likely to affect the motion pattern of the nematode. Determining the correlation between muscle arms and motion patterns can therefore be of specific implications in identifying the role of individual genes in locomotion, through the phenotypic locomotive behavior study [82]. On the smooth surface of agar plates, it is well understood that worms crawl on their sides and their sinusoidal waves are generated by a sequence of dorsal-ventral

muscular contractions that is opposed to a restoring force provided by the internal hydrostatic pressure of the worm [83]. These dorsal-ventral muscles push worms against their surroundings to generate force thrust. The number of muscle arms are found to be positively correlated to the amplitude of waves in *C. elegans* locomotion [84]. As the wave is generated by the contraction force, a very interesting question arises. Is there any positive correlation between the contraction force and the wave amplitude? Or, is there a positive relationship such that a mutant with more muscle arms generates greater motion forces? To answer these questions, a force sensor suitable for the small animal is required. As the nematode is tiny (~1 mm in length and <90 μm in width, invisible to the naked eye), the typical sensors used in millimeter and larger scales are unable to detect the micro-Newton-level force.

At the micro–nanoscale, mechanical measurements are often conducted using transducers based on MEMS (microelectro-mechanical systems), such as capacitive force sensors and piezoresistive cantilevers [85-89]. Compared to other cellular force measurement techniques, such as optical and magnetic tweezers [90-91], AFM (atomic force microscopy) [92-93], magnetic bead measurement [94] and micropipette aspiration [95], MEMS force sensors are more cost-effective and provide greater flexibility for system integration. However, the construction of MEMS force transducers typically depends on silicon micromachining that requires sophisticated equipment and increases the processing effort. Furthermore, issues such as biocompatibility and operation in aqueous environments often impose stringent requirements on MEMS design, material selection, and microfabrication.

Two decades ago, the flexible substrate method was introduced for characterizing mechanical interactions between biological cells and their surrounding environment [96]. More recently, an innovative alternative approach employing PDMS (microfabricated polydimethylsiloxane) post/pillar structures as force transducers was reported to visually measure traction forces generated by adherent cells (smooth muscle cells [97], epithelial cells [98], and cardiac myocytes [99]). Unlike flexible thin substrates, the post/pillar structure does not require heavily complex computations for calculating traction forces. Compared to silicon-based MEMS devices, PDMS-based devices are biocompatible and can be readily fabricated using soft-lithography techniques [100].

The last couple of years have seen a number of pioneering applications of PDMS devices to perform novel assays on *C. elegans*, including artificial dirt for sensory and motor behaviours [101], microfluidic chip for sub-cellular assay [102-103], clamps for immobilizing and imaging [104], maze for exploration and learning [105], and chambers for generating oxygen gradients [106], to name just a few. Biocompatibility, transparency, and easy fabrication render the popularity of PDMS and make it an ideal material for force sensing in *C. elegans* locomotion.

There have been few systems for measuring forces of *C. elegans*. A silicon piezoresistive cantilever [71] has been fabricated to characterize the mechanics of *C. elegans* body tissue (Figure 2.17). Constrained onto its culture surface or a testbed by the cantilever free end, the worm is not able to move freely, which excludes the sensor from sensing the dynamic force of moving *C. elegans*.

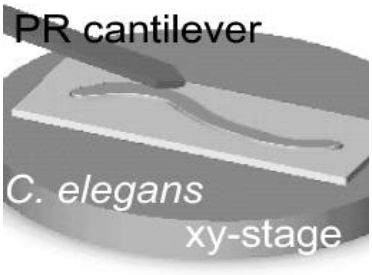

Figure 2.17 Schematic of silicon piezoresistive cantilever system to characterize the mechanics of *C. elegans* body tissue reposted in [71].

Very recently, a device with SU-8 based rising pillars [107] has been developed to measure dynamic forces, with each pillar having four 90-degree-spaced gold resistors as strain gauges, which were deployed on its bottom base (Figure 2.18). The resistance change of the strain gauges gives the force applied at the tip of the pillar.

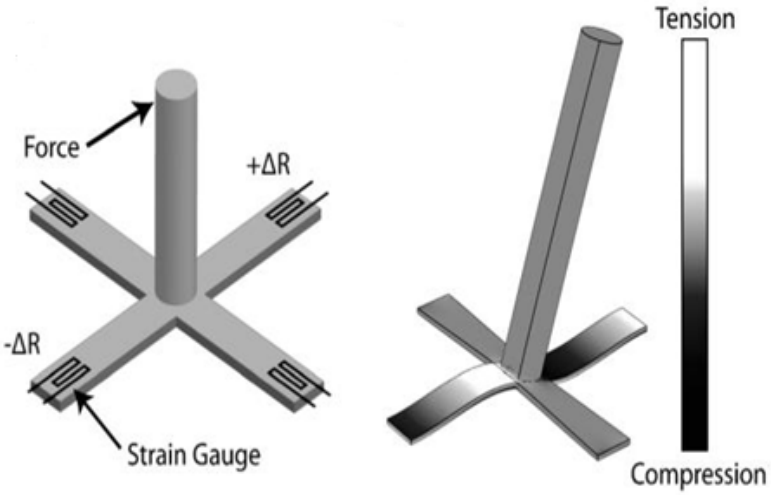

Figure 2.18 Schematic of pillar made of SU-8 with four gold resistors as strain gauges on bottom bases to measure dynamic forces of *C. elegans* presented in [107].

Three main drawbacks exist for this device: (i) use of the strain gauges complicates the microfabrication procedure and measuring

instrumentation, (ii) heat dissipated from the gold resistors is likely to affect the natural locomotion of temperature-sensitive nematode, (iii) the complicated structure of the device easily occludes a moving worm, causing unwanted barriers for studying worm locomotion.

To overcome these drawbacks, a simpler force sensor is highly desired. Chapters 6 and 7 of this work report on a micropillar-based on-chip system capable of constantly measuring force of *C. elegans* in motion. The system consists of a micropillar-based device made of PDMS only and a vision-based algorithm for resolving force from the deflection of the cantilever-like pillars. The microdevice, sub-pixel resolution for visual tracking the deflection, and the experimental technique form an integrated powerful system for measuring dynamic forces of moving *C. elegans* in high resolution. This will lead to a unique on-chip phenotypic screening framework for small animals like *C. elegans*.

2.3 HAPTIC MICROROBOTIC INJECTION AND *C.ELEGANS* FORCE MEASUREMENT SYSTEM

The completion of *C. elegans* genome sequence has been a major milestone in biology. Now, in this area, the focus of research is to discover how genetic information specifies the development, anatomy and behavior of *C. elegans* [108-111]. One of the most interesting aspects of such a behavioral study of the worm is spontaneous locomotion analysis of *C. elegans* [112-113]. As such, it is required to facile new reverse genetic tools for converting sequence information into functional information. One of which is delivering RNA to *C. elegens* by direct microinjection into the cytoplasm of the intestine (Figure 2.19), as the most effective method for blocking gene functions.

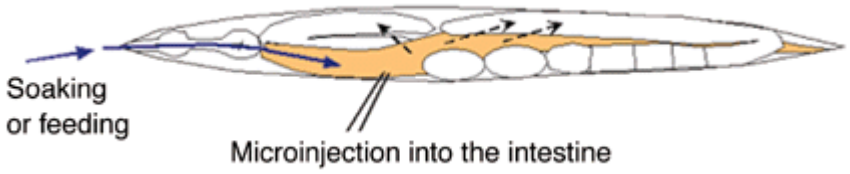

Figure 2.19 Microinjetion of RNA into cytoplasm of the intestine (orange organ) of *C. elegans* as described in [108].

Other examples would be microinjection of mutant DNA to produce transgenic worms (Figure 2.20) or deposition of a desired DNA construct into the syncytial gonad (cytoplasmic continuity between the constituent cells) of the hermaphrodite worm (Figure 2.21). It is a way of obtaining germ-line transformation of *C. elegans*

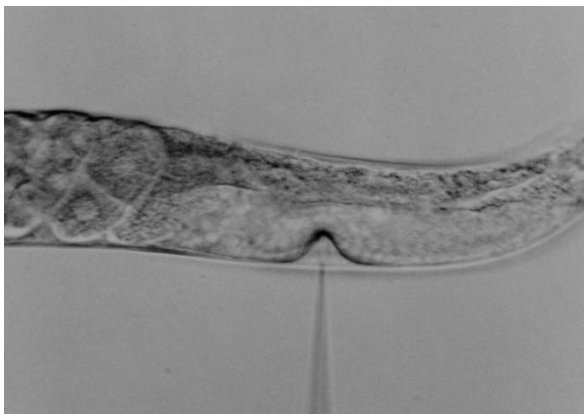

Figure 2.20 Microinjection of mutant DNA to produce transgenic *C. elegans* (adapted from www.lawrence.edu/fast/destasie/lab.html).

Efficient microinjection operations facilitate the recovery of *C. elegans* transformants and study the mechanism of *C.elegans* DNA and RNA transformation [114-115].

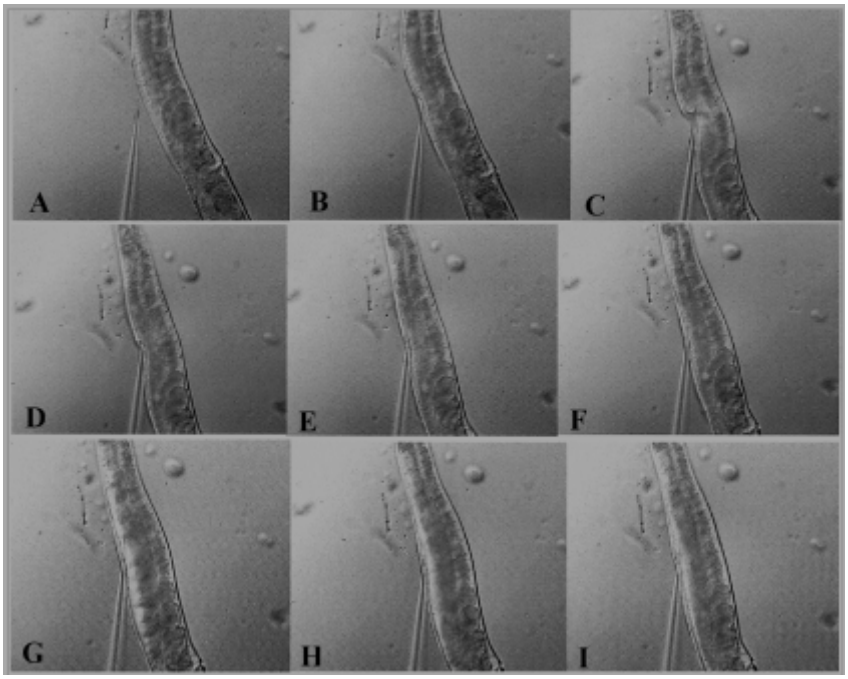

Figure 2.21 Different steps for the DNA microinjection of *C.elegans* in the gonad (adapted from the Jim Morley's movie, filmed in the Morimoto laboratory).

In this perspective, one of the exiting directions of this work would be the fusion of haptic microrobotic injection system with the *C. elegance* force measurement system. As a result, an integrated system of conducting precision microinjection and locomotion behavior analysis of *C. elegans* would be formed.

2.4 SUMMARY

The ability to manipulate individual biological cells is the subject of an increasing research interest. At present bio-operators perform cell injection manually and remain limited to their visual sense for task feedback. Research suggests that it takes approximately one year to adequately train an operator in the cell injection process and despite this, success rates remain low. Some works propose autonomous systems for the cell injection operation and such approaches offers the benefits

inherent to system autonomy. Such autonomous systems are suitable where complete knowledge of the cell can be obtained and high-throughput cell injection is desirable.

The aim of this thesis is not to replicate the research effort into the presented new cell injecton systems. The focus of the first major contribution of this thesis is the class of applications where high-throughput cell injection is unnecessary and it is desirable to retain the human-in-the-loop. Retaining the human-in-the-loop natively caters to flexibility, adaptation and utilization of human level judgment and intuition. That is not to say that autonomously determined actions should be neglected. Rather, autonomously determined actions (such as those which would control an autonomous system) are considered as haptic suggestions displayed to the bio-operator. Given the bilateral characteristic of the implemented haptic device, the operator is able to ultimately decide whether or not to conform to the haptic suggestions. When displayed, the haptic suggestions can be evaluated and, if desired, easily overridden to execute the operator's own control actions.

C.elegans is a microscale nematode, popular as an experimental genetic system in biological research. Review of the literature revealed that there have been several approaches to measuring forces of *C. elegans*. These include silicon-based MEMS devices, SU-8 based rising pillars or devices which immobilize the *C. elegans* for force measurement. These works however, either require complicated fabrication and measurement, or are bio-incompatible, or occlude motion forces due to immobilization. In order to address these issues, an efficient and simple force sensor for measuring the force of *C. elegans* in motion is required. Recently, PDMS pillar structures as force transducers are introduced. Due to their

transparency, it is possible to visually measure traction forces. In contrast to silicon-based MEMS devices, PDMS-based devices are biocompatible and can be readily fabricated using soft-lithography techniques. In addition, unlike flexible thin substrates, the post/pillar structure does not require heavily complex computations for calculating traction forces.

Accordingly, the second major contribution of this thesis is a PDMS-based micropillar structure and image processing technique for accurately tracking of micropillar deflections to measuring forces of moving *C. elegans*. The approach also provides the capability for batch force measurement of moving *C. elegans*.

"There's real poetry in the real world. Science is the poetry of reality."

Richard Dawkins
1941-present, English biologist

Chapter 3

HAPTIC MICROROBOTIC CELL INJECTION SYSTEM

Microrobotic cell injection is an area of increasing research interest. Currently, in manual cell injection the operator remains limited to their visual sense and is unable to adequately perceive the microscale environment. This results in extended training times as well as poor success rates and repeatability. This Chapter addresses a novel approach which integrates the operator's haptic sensory modality offering immense benefits over conventional techniques. It investigates haptic bilateralism and introduces a mapping framework resulting in an intuitive method allowing the operator to manoeuvre the micropipette in a manner similar to handheld needle insertion. Aside from enhancing the method by which to manoeuvre the microrobot, this mapping establishes the basis to render

haptic information to the operator facilitating simultaneous haptic guidance as well as cell indention force feedback during cell injection.

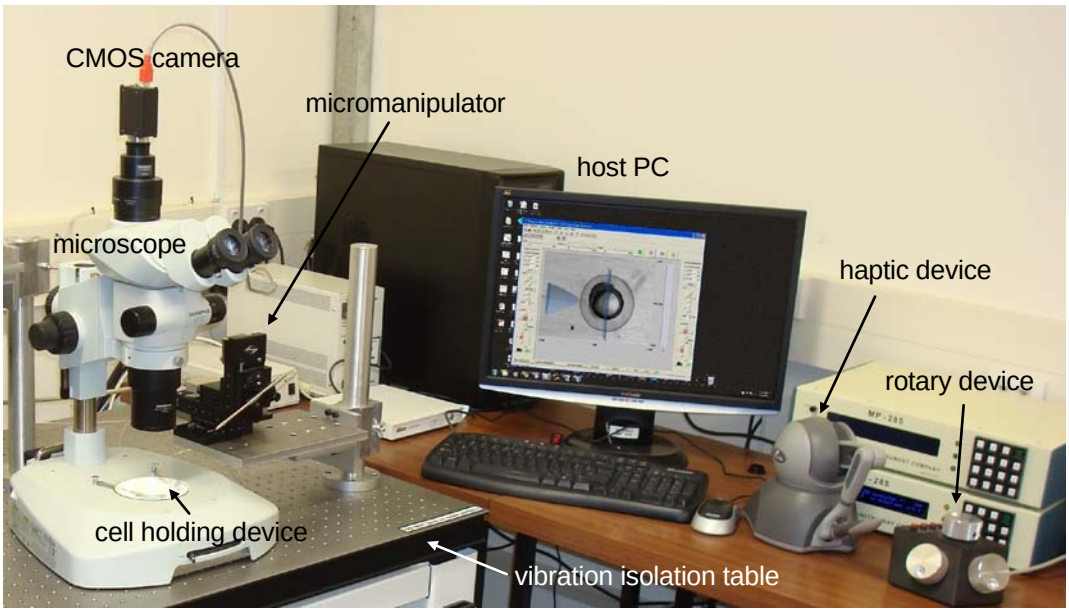

Figure 3.1 Haptic microrobotic cell injection system.

3.1 SYSTEM ARCHITECTURE

Figure 3.1 depicts the haptically assisted microrobotic cell injection system. The micromanipulator is the MP-285 from Sutter Instruments which provides 3 actuated Degrees of Freedom (DOF) and 2 manually adjustable DOF. The 3 actuated DOF provide a $25mm$ linear range and $0.04\mu m$ positioning resolution. Cell injection is achieved through a glass micropipette with an outside diameter of 25 μm at the tip end. A Venturi vacuum pump (UN816, KNF) provides negative pressure to immobilize the cell in a vacuum-based holding device [116]. The PMI-200 pressure micro-injection system (Dagan) with computer controlled injection trigger provides positive pressure for material deposition. The cell holding dish is in view of the microscope lens and the A601f-2 CMOS camera (Basler) is

mounted on top of the SZX2-ILLB optical microscope (Olympus). This provides the necessary visual information from the cell injection process. System control and monitoring is achieved using a PC (Intel Core Duo CPU 2.66GHz, 4GB RAM). The micromanipulator is interfaced to the PC using the PCI-6259 DAQ card (National Instruments). The Phantom Omni haptic device (Sensable Technologies) provides the interface for the operator to control the micromanipulator during cell injection. The setup (excluding the PC and the injection unit) are mounted on a vibration isolation table.

This thesis work focuses on enhancing human-in-the-loop cell injection while retaining the operator's human-level expertise, knowledge and intuition. Feedback from the cell injection process (such as that which would govern a completely autonomous system) is provided to the operator and the operator ultimately decides whether or not to act in accordance with such haptic suggestions. This capability is facilitated by the bilateral nature of the haptic interface. The result is that the operator is provided with system determined suggestions however retain the ability to override such suggestions and exercise their own judgment. Given the bilateral nature of the implemented haptic device, the introduction of haptic interaction necessitates two distinct components, namely;

- *The mapping framework* which enables the bio-operator to control the micromanipulator using the haptic device. This also results in an intuitive method for controlling the movement of the micropipette in a similar fashion to conventional handheld needle insertion.

- ***The haptic feedback/assistance*** (virtual fixtures and cell indentation force) which is haptically rendered to the bio-operator while performing the cell injection process.

Figure 3.2 graphically depicts the operation of the *mapping framework* and *haptic feedback/assistance* including the corresponding directions of

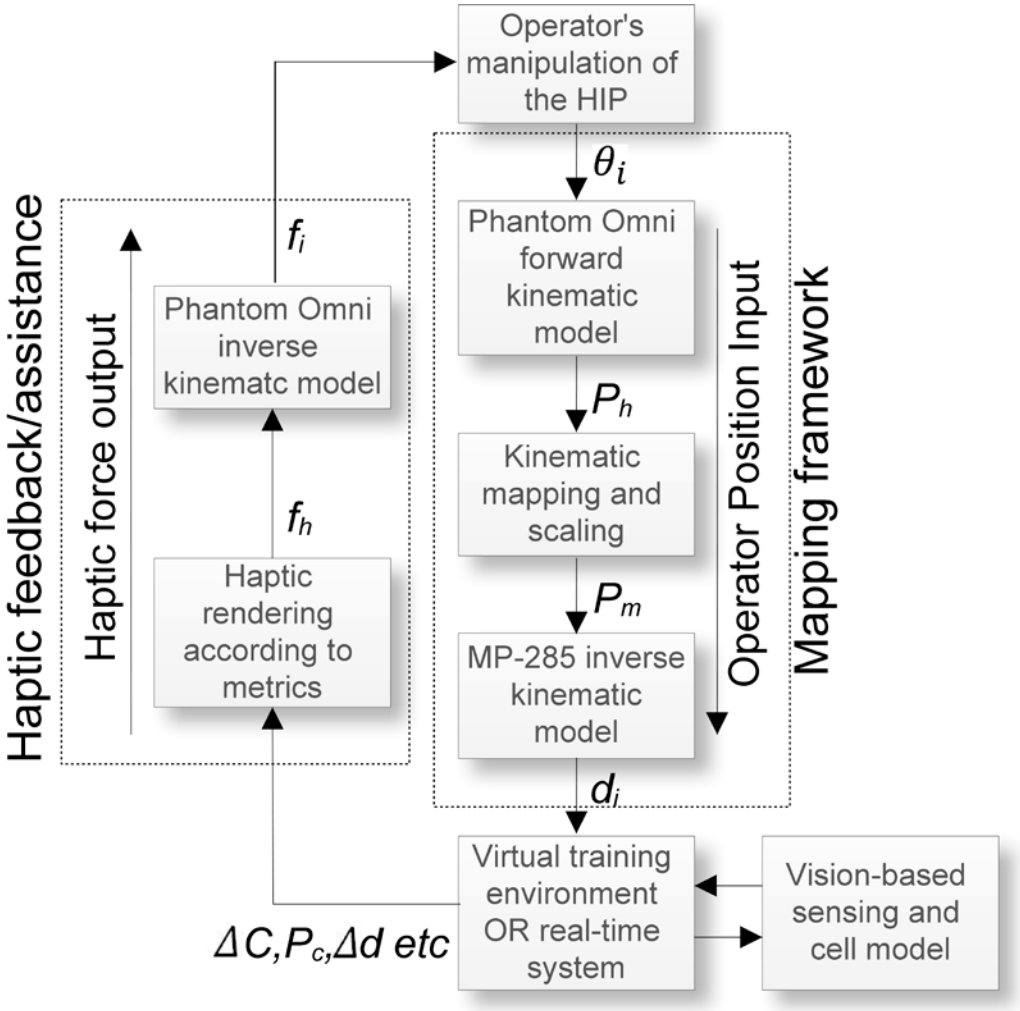

Figure 3.2 Architecture of the haptic cell injection system. θ_i denotes the operator's manipulation of the haptic stylus, P_h is the current position of the *haptic interaction point*, P_m is the position of the tip of the micropipette and possible sensed quantities include: ΔC cell deformation, P_c position of the cell and Δd depth of insertion.

information flow in a bilateral haptic system.

It is important to acknowledge that the bio-operator's movement of the haptic stylus (position input) and haptically rendered force (haptic force output) both occur simultaneously at the device's single haptic interaction point. As is discussed later, this bilateralism is the basis for the bio-operator to receive haptic assistance or feedback while retaining ultimate control of the micromanipulator during the cell injection task.

The ability for the operator to control the micromanipulator using the following mapping framework also lends itself to training the bio-operator offline. In such a scenario, the bio-operator/s can be trained within in a haptically enabled virtual environment. Haptic guidance can then be used to train the bio-operator in various aspects of the cell injection process, e.g. trajectory following, speed of insertion and accuracy training. After sufficient training, the bio-operator/s can move to the physical cell injection system and directly transfer their training experience to real cell injection using an identical mapping framework.

The control issues integral to achieving adequate control of the micromanipulator using the Phantom Omni haptic device are addressed in next Chapter.

The following section introduces the mapping framework enabling the operator to control the micromanipulator using the Phantom Omni haptic device. This also establishes the basis to provide haptic assistance or feedback to the operator during cell injection.

3.2 HAPTIC MAPPING FRAMEWORK

This section focuses on a 3D position-to-position kinematic mapping framework to provide the bio-operator with a method to control the micromanipulator (and micropipette) using the Phantom Omni manipulator-style haptic device. Conventionally the MP-285 micromanipulator is controlled using a rotary encoder device for each of the three axes of the micromanipulator independently (Figure 3.1). To aid in injection tasks, one rotary encoder can be used to control motion along a user specified virtual 4^{th} axis. Sutter Instruments also provides an alternative joystick to control the micromanipulator. The joystick control mode uses position-to-velocity mapping where the operator's roll, pitch and yaw joystick deflections correspond to commanded velocities of the micromanipulator.

The significance of the mapping framework introduced in this section is two-fold.

- Firstly, position-to-position mapping provides a logical simplified method for the operator to control the micromanipulator. In contrast to the two methods discussed above, the operator needs only position the haptic device in 3D space, the same as if physically positioning the micropipette's tip at the microscale. It is suggested that this is more intuitive for 3D manipulation.

- Secondly, such a mapping framework provides the necessary foundation to introduce intuitive haptic feedback/assistance directly to 3D space, which is not possible using the other methods.

In order to realize the position-to-position mapping, formulation of the system's kinematics is necessary, in particular an understanding related to the micropipette's longitudinal (insertion) axis and formulations for the kinematic control of the Phantom Omni haptic device.

3.2.1 MICROMANIPULATOR KINEMATIC

The MP-285 micromanipulator provides 3 actuated Degrees of Freedom (DOF) and 2 manually adjustable DOF. The 3 actuated DOF provide a $25mm$ linear range and $0.04\mu m$ positioning resolution. Table 3.1 presents MP-285 micromanipulator specifications. As the basis to utilize the micromanipulator in this work, the forward and inverse geometric models are required.

DOF – Actuated	3 DOF
DOF – Manual	2 DOF
Travel	25 mm on all three axes
Resolution	Coarse mode: 0.2 μm/step Fine mode: 0.04 μm/step
Maximum Speed	2.9 mm/sec.
Long Term Stability	<10 nm/hour at 24 deg C.
Drive Mechanism	Precision worm gear capstandrive
Serial Interface	RS-232, 9600 baud (1 start bit, 8 data bits, 1 stop bit)
Dimensions	11cm × 15cm × 16cm
Weight	1.7kg

Table 3.1 MP-285 Micromanipulator specifications [117].

The Denavit-Hartenberg (D-H) representation [118-119] assists in the formulation of the direct geometric model of the MP-285 micromanipulator in order to express the orientation and position of the micropipette's tip given the current joint variable states, θ_i for $i = 1$ *to* 6 as shown in Figure 3.3. The position of the micropipette's tip, is given by a three vector denoted by P_m, in the base frame, {M}. The modified D-H parameters for the MP-285 micromanipulator are presented in Table 3.2.

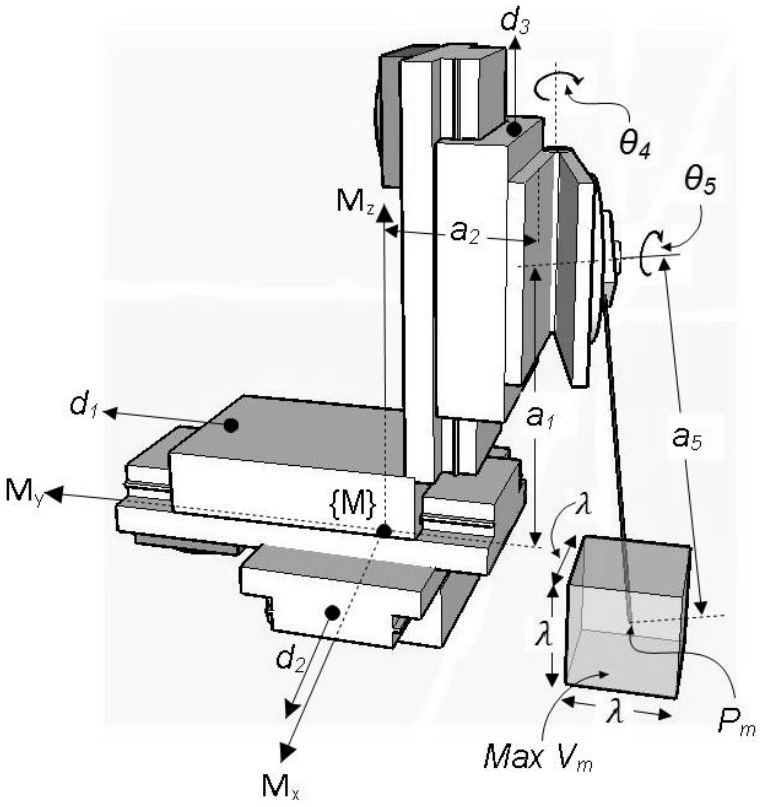

Figure 3.3 MP-285 micromanipulator and modified D-H kinematic notation. $\{M\}$ is the manipulator's global reference frame, P_m denotes the tip of the micropipette, V_m is the volume of the manipulators workspace and λ is the desirable workspace.

Given the D-H parameters presented in Table 3.2, the pose of the tip of the micropipette is given by

$$ {}^{M}_{6}T = \begin{bmatrix} R_6^M & P_{m_6}{}^M \\ 0 & 1 \end{bmatrix} \tag{3.1} $$

where P_m is a three vector expressing the location of the micropipette tip and R is a 3×3 matrix expressing the orientation of the frame {6} in the inertial frame {M}, given by

$$ P_m = \begin{bmatrix} m_x \\ m_y \\ m_z \end{bmatrix} = \begin{bmatrix} X_0 \\ Y_0 \\ Z_0 \end{bmatrix} = \begin{bmatrix} -140C_4C_5 + 29 - 29C_4 + d_2 \\ -140S_4C_5 - 77 - 29S_4 + d_1 \\ 140S_5 + 77 + d_3 \end{bmatrix} \tag{3.2} $$

and

$$ R_6^M = \begin{bmatrix} -C_4C_5 & C_4S_5 & -S_4 \\ -S_4C_5 & S_4S_5 & C_4 \\ S_5 & C_5 & 0 \end{bmatrix} \tag{3.3} $$

Joint i	α_{i-1}	a_{i-1}(mm)	d_i(mm)	θ_i
1	$-\pi/2$	0	d_1	$-\pi/2$
2	$-\pi/2$	77	d_2	$-\pi/2$
3	$-\pi/2$	-102	d_3	$\pi/2$
4	0	-29	0	θ_4
5	$\pi/2$	29	0	θ_5
6	0	140	0	0

Table 3.2 Denavit-Hartenberg (modified) kinematic parameters for the MP-285 micromanipulator. Joint i for $i = 1$ *to* 3 are the three *active* prismatic joints; Y-translation, X-translation and Z-translation respectively, a_i are the link lengths from joint i to joint $i+1$, α_i is the twist from joint i to joint $i+1$, d_i is the offset from joint $i-1$ to joint i and θ_i is the angle between joint $i-1$ to joint i expressed in radians. Joint 6 represents the tip of the micropipette.

where C_i and S_i represent the $cos(\theta_i)$ and $sin(\theta_i)$ functions respectively, θ_i represents the angle between joint $i-1$ to joint i expressed in radians, d_i for $i = 1$ to 3 are the distances of actuation of the three prismatic joints, X_m, Y_m and Z_m are with respect to the inertial reference frame $\{M\}$, and the columns of R are unit vectors representing the orientation of the x, y, z axes of the 6^{th} reference frame (at the micropipette's tip) respectively, with respect to $\{M\}$.

The above analysis expresses the location and orientation of the micropipette's tip within the micromanipulator's global reference frame, $\{M\}$. The orientation of the micropipette's longitudinal axis is given by the unit vector for the x-axis of the 6th reference frame (first column of rotation matrix R).

In order to determine the appropriate joint displacements as a function of the desired position of the micropipette's tip, the inverse geometric model of the MP-285 manipulator is given by

$$d(P_m) = \begin{bmatrix} d_1 \\ d_2 \\ d_3 \end{bmatrix} = \begin{bmatrix} 140S_4C_5 + 77 + 29S_4 + Y_m \\ 140C_4C_5 - 29 + 29C_4 + X_m \\ -140S_5 - 77 + Z_m \end{bmatrix} \tag{3.4}$$

where θ_4 and θ_5 (depicted by Figure 3.3) can only be adjusted manually, and as is case with conventional cell injection, are assumed to be constant throughout system operation.

In order to implement the mapping framework between the haptic interface and micromanipulator, the usable workspaces of the two devices needs to be considered. The workspace of the micromanipulator is demonstrated in Figure 3.3 where $\lambda_{(max)} = 25mm$.

3.2.2 HAPTIC INTERFACE KINEMATIC

The Phantom Omni haptic device (Sensable Technologies) provides the interface for the operator to control the micromanipulator during cell injection. In order to formulate the mapping framework an understanding of the current position of the HIP (haptic interaction point) is necessary. Furthermore, in order to display haptic feedback/assistance to the operator a method to display the appropriate force at the HIP is required.

The Phantom Omni can be considered as a back drivable, cable driven robotic manipulator providing zero backlash, low inertia and near zero friction. The device provides 6-DOF motion input with 3-DOF capable of force feedback. The 3-DOF of the device's spherical wrist are passive and intersect at the HIP as shown in Figure 3.4. It represents a cost-efficient technology and its specifications are listed in Table 3.3.

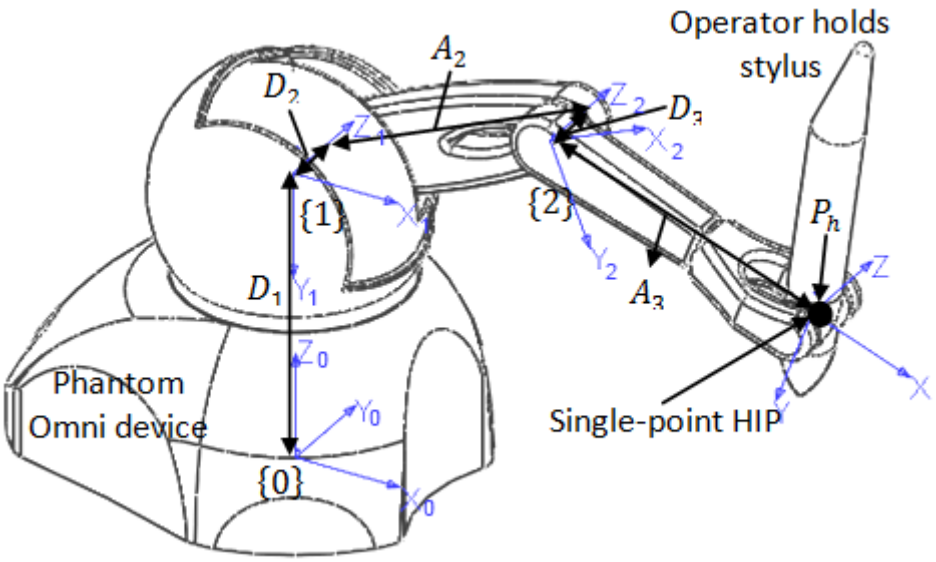

Figure 3.4 Forward geometric analysis of the Phantom Omni. z_{0-2} are the axes of rotation of the three actuated joints of the device, P_h is the current position of the HIP, D_1, D_2, A_2, D_3 and A_3 are standard D-H parameters as listed in Table 3.4.

DOF – Motion Tracking	6 DOF
DOF – Force feedback	3 DOF
Maximum Exertable Force (nominal orthogonal arms position)	3.3 N
Force Feedback Workspace	See Figure 3.5, 3D haptic workspace analysis
Base Footprint	≈ 168 W x 203 D mm
Device Weight	1.78 kg
Positional Resolution - Nominal	≈ 0.055 mm
Stiffness	X-axis 1.26N/mm Y-axis 2.31N/mm Z-axis 1.02N/mm
Inertia at tip	0.045kg
Interface	IEEE 1394 Firewire

Table 3.3 Phantom Omni specifications [120].

The ability for the bio-operator to interact with the Phantom Omni haptic device to control the micromanipulator and receive haptic assistance/ feedback is a foundation for this work. As such, a thorough discussion of the acquisition of the HIP's position and the display of the force vector at the HIP is necessary. The below presented formulations and kinematic control achieve this capability independent of a reliance on the Phantom Omni API black box. This proves valuable to those implementing this work with a kinematically altered Phantom Omni [121] or a similar serial link structured device.

As this point it is worth reemphasizing that the MP-285's last two DOF, i.e. θ_4 and θ_5 (depicted by Figure 3.3) can only be adjusted manually

and are not directly controllable by the system. The result of this is that operator can only control the position of the micropipette, P_m, and cannot manipulate the orientation of the micropipette, i.e. R_6^M, in real-time. This is also the case for conventional or automated cell injection using such a micromanipulator. Therefore, the cell and micropipette are pre-arranged appropriately so it is possible to perform injection in the direction of the micropipette's longitudinal axis.

Given that the Phantom Omni's last 3-DOF are passive about a single point, the HIP is formed at the center of the device's spherical wrist (Figure 3.4). Haptic information can only be displayed to the operator at this HIP. Given the inability to control the orientation of the micropipette, as discussed above, and the desire to provide the operator with haptic feedback/assistance it is logical to consider only the Phantom Omni's actuated 3-DOF in the control of the micromanipulator. The position of the HIP is a function of the actuated joint's angles (θ_i for $i = 1$ *to* 3).

The position of the HIP with respect to the device's global coordinate system, {0}, is given by a forward geometric model based on the standard D-H notation. The *manipulator-type* haptic device offers three *active* (haptic feedback capable) DOF, namely; the waist (*frame* {1}), shoulder (*frame* {2}) and elbow (*frame* {3}). There are also three *passive* DOF (no haptic feedback) forming a spherical wrist. Figure 3.4 depicts our D-H frame assignment for the Phantom Omni haptic device. The D-H parameters corresponding to the Phantom Omni frame assignments of Figure 3.4 are presented in Table 3.4.

Joint i	A_i	α_i	D_i	θ_i
1	0	$-\pi/2$	$133.35\ mm$	θ_1
2	$133.35\ mm$	0	$-18\ mm$	θ_2
3	$133.35\ mm$	0	$18\ mm$	θ_3

Table 3.4 Denavit-Hartenberg geometric parameters for the Phantom Omni. Joint i for $i = 1$ *to* 3 are the three *active* joints; waist, shoulder and elbow respectively, A_i are the corresponding link lengths, α_i are the link twists, D_i are the link offsets and θ_i are the joint variables.

Given the D-H coordinate frames and geometric parameters presented in Figure 3.4 and Table 3.4 respectively, the position and orientation of the *HIP* is given by

$$ {}^{0}_{3}T = \begin{bmatrix} R^0_3 & P_{h_3}{}^0 \\ 0 & 1 \end{bmatrix} \tag{3.5} $$

where R is a $3x3$ matrix expressing the orientation of frame {3} in the inertial frame {0} and P_h is a three vector expressing the location of the Phantom Omni's HIP given by

$$ P_h(\theta) = \begin{bmatrix} h_x \\ h_y \\ h_z \end{bmatrix} = \begin{bmatrix} X_o \\ Y_0 \\ Z_0 \end{bmatrix} = \begin{bmatrix} 133.35C_1(C_2 + C_{23}) \\ 133.35S_1(C_2 + C_{23}) \\ 133.35(1 - S_2 - S_{23}) \end{bmatrix} \tag{3.6} $$

where $\theta \in \mathbb{R}^3$ is a vector of joint positions, C_i and S_i represent the $cos(\theta_i)$ and $sin(\theta_i)$ functions respectively, s_{ij}represents $sin\ (\theta_i + \theta_j)$ and C_{ij} represents $cos\ (\theta_i + \theta_j)$, h_x, h_y and h_z are with respect to the inertial reference frame {0}. At this point it is worthwhile to reconsider the *passive* nature of the three DOF in the wrist of the Phantom Omni, i.e. joint i, for $i = 4$ *to* 6. The axes of these DOF intersect at the HIP and the current

orientations of these joints, i.e. θ_i for $i = 4$ *to* 6, are fully dependent on the user's manipulation of the haptic stylus. Given that the HIP is a single-point of arbitrary orientation, and in the interests of space, R_3^0 is not presented.

This work considers the bio-operator's bilateral haptic interaction with the Phantom Omni's HIP as the basis for both control of the micromanipulator (mapping framework) and haptic feedback/assistance. While P_h provides the necessary location of the HIP within the reference frame $\{0\}$, a method to display the haptically rendered forces to operator is required. Joint torques can be directly applied to the force feedback capable joints (joint space) of the Phantom Omni's serial kinematic structure; however a method to display the desired force vector at the HIP (task space) is required. As is common practice, given the low inertia, zero backlash and near-zero friction present in the Phantom Omni, we utilize kinematic control to display the appropriate force at the HIP. The static relationship between joint space torques, τ, and the haptic force in task space, F_{haptic} can be expressed by

$$\tau = J^T(q)F_{haptic} \tag{3.7}$$

where $\tau = [\tau_1 \quad \tau_2 \quad \tau_3]^T$ is of Nm units, $F_{haptic} = [F_x \quad F_y \quad F_z \quad 0 \quad 0 \quad 0]^T$ is in Newtons and $J(q)$ represents the $6x3$ Jacobian matrix of the Phantom Omni's three actuated joints given by

$$J(q) = \begin{bmatrix} -lS_1(C_2 + C_{23}) & lC_1(C_2 + C_{23}) & -lC_1S_{23} \\ lC_1(C_2 + C_{23}) & -lS_1(S_2 + S_{23}) & -lS_1S_{23} \\ 0 & -l(C_2 + C_{23}) & C_1(dS_1 - lC_1C_{23}) - S_1(dC_1 + lS_1C_{23}) \\ 0 & -S_1 & -S_1 \\ 0 & C_1 & C_1 \\ 1 & 0 & 0 \end{bmatrix} \quad (3.8)$$

where $l = D_1 = A_2 = A_3 = 0.13335\,m$, q is a vector of joint variables and $d = -D_2 = D_3 = 0.018\,m$.

3.2.3 WORKSPACE ANALYSIS

The above kinematic analysis expresses the location of the HIP within the reference frame, {0}. When investigating the mapping framework, the usable workspaces of both the haptic device and micromanipulator need to be considered.

The maximum usable cubic workspace for the Phantom Omni haptic device was empirically determined to be $\tau = 125\,mm$ (Figure 3.3) where $hy_1 = 124\,mm$ and $hz_1 = 80\,mm$, as depicted by Figure 3.5.

When specifying the corresponding workspaces it is worthwhile to consider the ability of the micromanipulator (slave) to adequately track the motion of the haptic device (master) as well as the achievable control resolution. The following section considers the implications of the chosen workspace for the Phantom Omni device and MP-285 micromanipulator.

In order to constrain the operator's manipulation of the HIP to the specified workspace (τ), the boundaries of the workspace limits are haptically rendered to the operator as demonstrated by Figure 3.6.

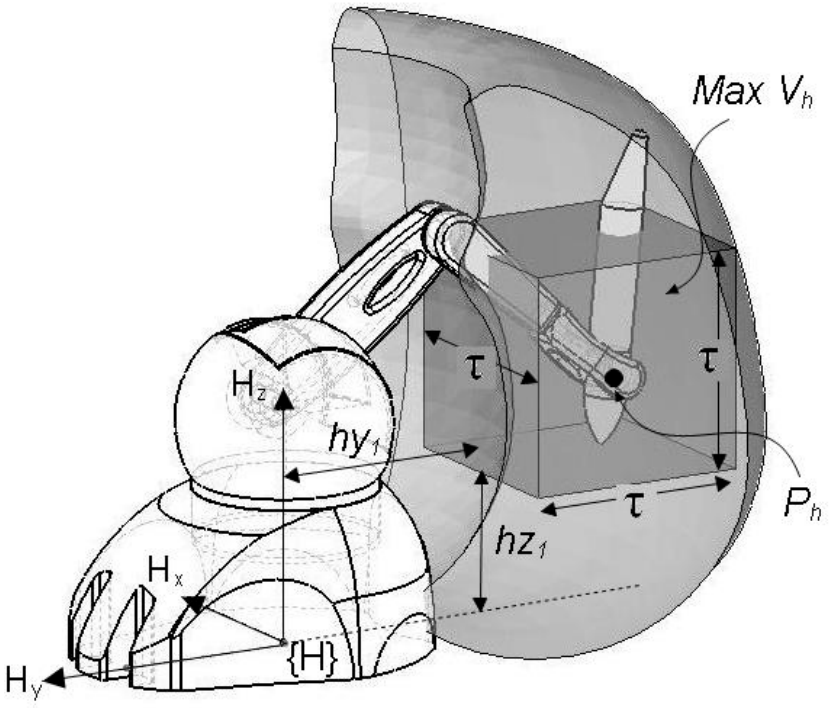

Figure 3.5 Workspace analysis of Phantom Omni haptic device. V_h is the volume of the maximum usable cubic workspace and hy_1 and hz_1 are the offsets of the workspace from the respective world reference frame axes.

Given a desired workspace defined by τ, the operator's manipulation of the HIP is subject to the following workspace constraints

$$-\tau/2 \leq h_x \leq \tau/2 \tag{3.9}$$

$$-hy_1 - 62.5 - \tau/2 \leq h_y \leq -hy_1 - 65.5 + \tau/2 \tag{3.10}$$

$$hz_1 + 62.5 - \tau/2 \leq h_z \leq hz_1 + 62.5 + \tau/2 \tag{3.11}$$

Given the above defined constraints, the haptic rendering of the desirable workspace boundaries requires two considerations: namely a) *collision detection* and b) *force response and control.*

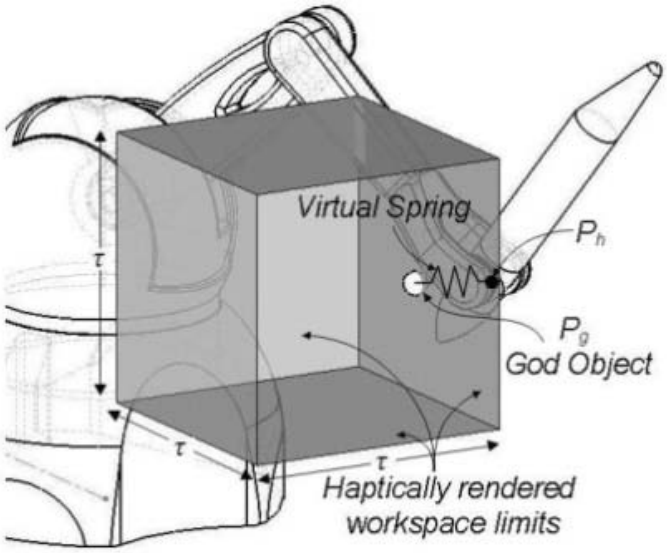

Figure 3.6 Haptic rendering of the workspace limits using the god-object algorithm and virtual spring.

The *collision detection* component of the haptic rendering requires the determination of the current position of the HIP, P_h, given expression (3.6). If P_h does not satisfy the conditions of the allowable workspace, expressions (3.9)(3.10)(3.11) , then collision/penetration of the HIP with the virtual workspace limits can be assumed. In this case, *force response and control* is necessary to constrain the operator's manipulation of the *HIP* to the allowable workspace.

The god-object algorithm [122] specifies that the god-object cannot penetrate the virtual surface and that it moves along the virtual surface so as to minimise the distance from the HIP. A vector originating at the HIP (P_h) and terminating at the god-object (P_g) specifies the direction of the haptic force to be rendered. The minimum distance specification ensures that the planar limits (Figure 3.6) are rendered as frictionless haptic surfaces. Inside the allowable workspace, the god-object and HIP exist at the same point in space. As the HIP exceeds the allowable workspace, a

displacement between $P_g$and P_h exists, forming the basis for the haptic rendering. Spring models are commonly used in haptic rendering [45] and relates the desired position, P_g, with the current position, P_h, according to Hooke's law. The haptically rendered force is given by

$$F = \begin{cases} 0 & P_h = P_g \\ K(P_h - P_g) & P_h - P_g \neq 0 \end{cases} \tag{3.12}$$

where K is specified appropriately.

It is worth acknowledging that the maximum exertable force for the Phantom Omni is $3.3N$, so the haptically rendered force for distances greater that $3.3/K\ mm$ will be constant.

3.2.4 DETERMINATION OF SCALING FACTOR

The above sections discuss the necessary kinematic and workspace analysis of the Phantom Omni haptic device and the MP-285 micromanipulator. This provides the foundation for position-to-position kinematic mapping allowing the operator to control the position of the micropipette's tip using the Phantom Omni's single HIP. The operator also receives visual information from the microscope's mounted camera.

C_h and C_m are taken to be the centers of the Phantom Omni and micromanipulator's specified workspaces respectively. In order to facilitate the kinematic mapping between the two devices, $P_h^{'} = [X_0{}' \ Y_0{}' \ Z_0{}' \ ]^T$ and $P_m{}' = [X_M{}' \ Y_M{}' \ Z_M{}' \ ]^T$ are considered with respect to C_h and C_m. In other words, $P_h{}'$ and $P_m{}'$ are translations of P_h and P_m to have origins at the centers of the respective Phantom Omni and micromanipulator

workspaces. The mapping framework between the Phantom Omni haptic device and MP-285 micromanipulator is given by

$$\begin{bmatrix} X_0{}' \\ Y_0{}' \\ Z_0{}' \end{bmatrix} = \begin{bmatrix} K_S & 0 & 0 \\ 0 & K_S & 0 \\ 0 & 0 & K_S \end{bmatrix} \begin{bmatrix} X_M{}' \\ Y_M{}' \\ Z_M{}' \end{bmatrix} \tag{3.13}$$

where scalar K_S is a scaling factor of micromanipulator motion for given haptic device movement.

Given the mapping defined by expression (3.13), the workspaces of the both the Phantom Omni and the micromanipulator need to be considered. It is apparent that the scaling factor, K_S, will directly affect the operator's control resolution, i.e. the achievable minimum movement of the micromanipulator corresponding to the operator's minimum movement of the Phantom Omni haptic device. For example, if the maximum workspaces of the haptic device ($125mm$) and micromanipulator ($25mm$) are utilized, then $K_S = 5$. While this would allow the operator to utilize the entire workspace of the micromanipulator, it results in reduced control resolution for the operator. In this situation, a $1cm$ movement of the haptic device would correspond to a $2mm$ movement of the micromanipulator. When performing micromanipulation a higher control resolution is desirable.

In this work, control resolution refers to the minimum movement of the micromanipulator corresponding to the operator's minimum achievable movement of the the haptic device. This is considered as distinct to system resolution which is discussed later.

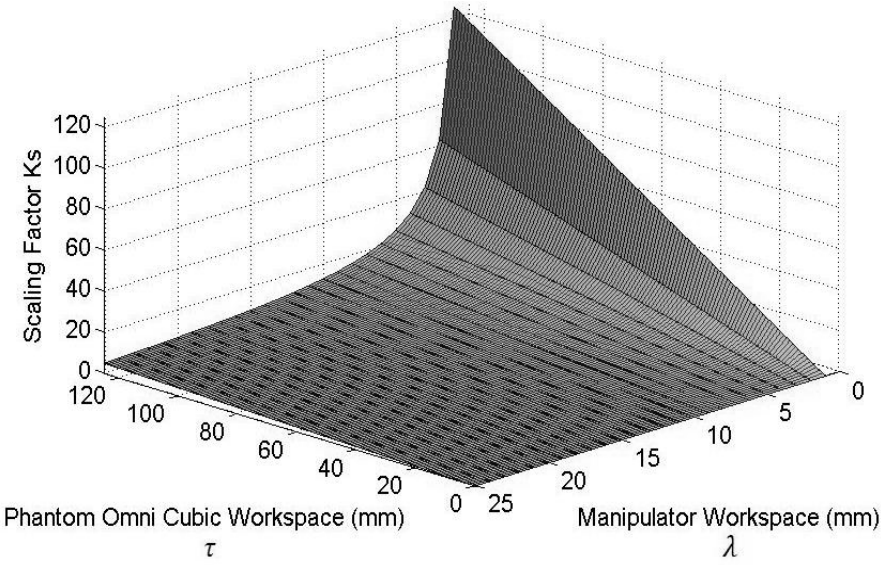

Figure 3.7 Tradeoff of the usable Phantom Omni (τ), micromanipulator workspace (λ), and scaling factor (K_s).

Given that the haptic device's workspace volume, V_h, is finite, the workspace of the micromanipulator, V_m, can be reduced in order to achieve higher control resolution for the operator. The choice of K_S then becomes a trade-off between the usable micromanipulator workspace and the operator's control resolution in manoeuvring the manipulator.

Figure 3.7 demonstrates the ability to reduce the workspace of the micromanipulator (λ) in order to achieve higher resolution manipulator control (higher K_S).

3.2.5 TRACKING DELAY

When K_S decreases, MP-285 micromanipulator (slave) needs to move faster to be able to track the mapping trajectory from the Phantom Omni haptic device (master). The MP-285 micromanipulator offers coarse and fine modes providing $0.2\,\mu m/step$ and $0.04\,\mu m/step$ resolutions

respectively. The coarse mode provides a faster maximum speed of $2.9\ mm/sec$ while maximum speed in fine mode is $470\ \mu m/sec$.

Tracking delay arises from different sources such as communication ports, micromanipulator driver and computer processing time. Several experiments conducted by setting a combination of commanded velocities and targeted positions to measure the time period beginning when the command is sent to the micromanipulator from the master side and ending when an acknowledge is sent back from micropositioning controller, confirming the positioning is performed.

For any set of commanded velocity and targeted position, a time from calculation, t_c, and a measured time, t_m, from the experiment is derived.

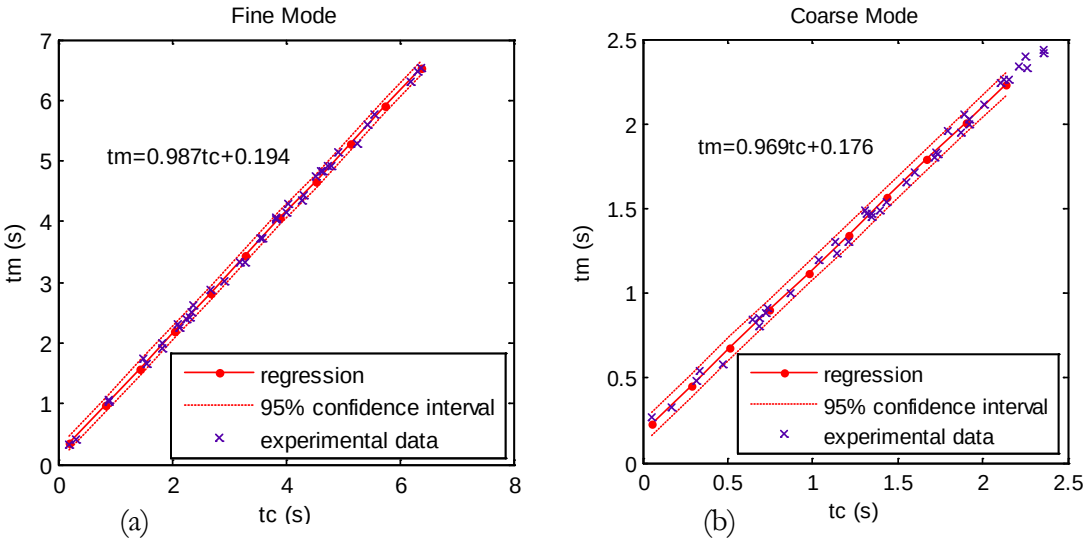

Figure 3.8 Time to execute commands with different targeted positions and commanded velocity. (a) Micromanipulator in fine mode with commanded velocity of $307\ \mu m/sec$. (b) Micromanipulator in coarse mode with commanded velocity of $810\ \mu m/sec$.

Figure 3.8 (a) depicts the time to execute commands with different targeted positions and commanded velocity of $307\,\mu m/sec$ while micromanipulator is set to fine mode. It indicates a linear behaviour with the fitted line expression of $t_m = 0.987t_c + 0.194$. The line slope relates the commanded velocity to the true velocity and the line constant represents the time delay. The delay was determined to be $194 \pm 1\,ms$ for all velocities in fine mode as long as velocity is set below $470\,\mu m/sec$.

Similar set of experiments conducted in coarse mode. Figure 3.8 (b) shows time to execute commands in coarse mode while commanded velocity was set to $810\,\mu m/sec$ with fitted line expression of $t_m = 0.969t_s + 0.176$. The delay was found to be $176 \pm 1\,ms$ for all velocities in coarse mode as long as velocity does not exceed $2.9\,mm/sec$.

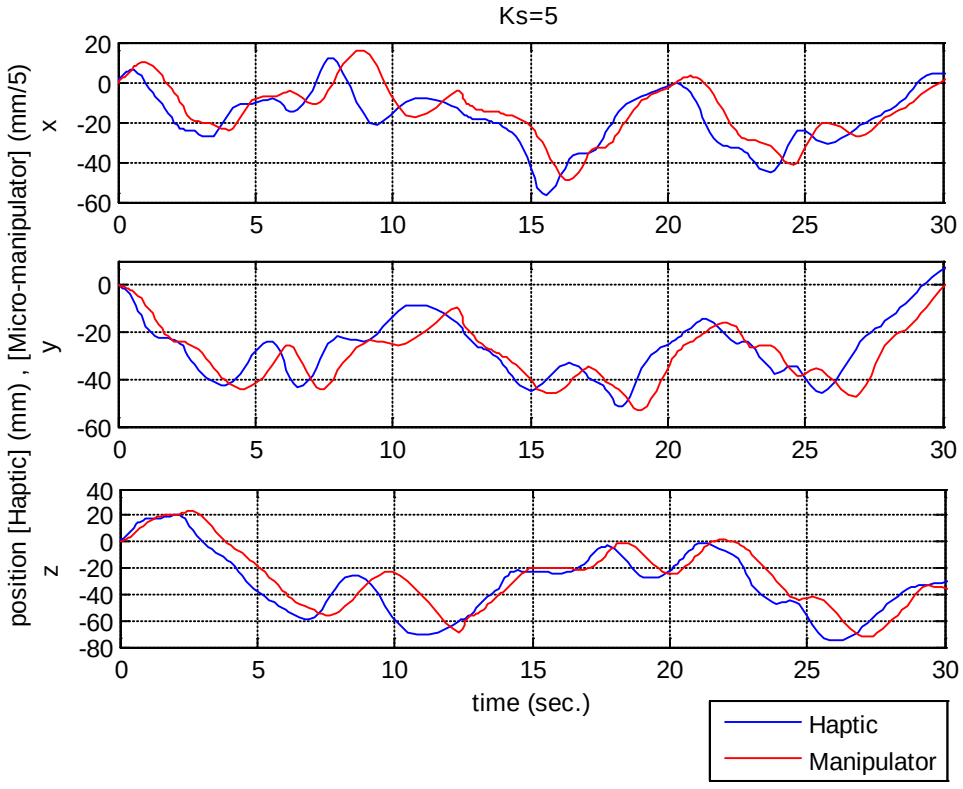

Figure 3.9 Position-to-position mapping framework performance with $K_s = 5$.

This study demonstrates tracking delay would stay bounded and independent of value of K_S as long as the micromanipulator is not obligated to exceed maximum speed of corresponding mode.

Figure 3.9, Figure 3.10, and Figure 3.11 depict the experiments of position-to-position mapping framework performance using three different scaling factors. When $K_S = 5$ and the micromanipulator is set to coarse mode, it tracks the position of the haptic device with a significant delay (Figure 3.9). This delay results from the limited maximum speed of micromanipulator when attempting to track the operator's hand movement. When K_S is increased to $K_S = 250$, the micromanipulator delay decreases significantly and drops to the derived coarse mode time delay (Figure 3.10(a)).

As Figure 3.10(b) shows, the micromanipulator velocity does not exceed the maximum speed of the micromanipulator in coarse mode while tracking the operator's hand movement. When K_S is increased to $K_S = 1000$ and the micromanipulator is set to fine mode, its delay remains bounded to the derived fine mode time delay (Figure 3.11(a)). In this case, the micromanipulator is not required to exceed the maximum speed of micromanipulator's fine mode in order to track the operator's hand movement (Figure 3.11(b)).

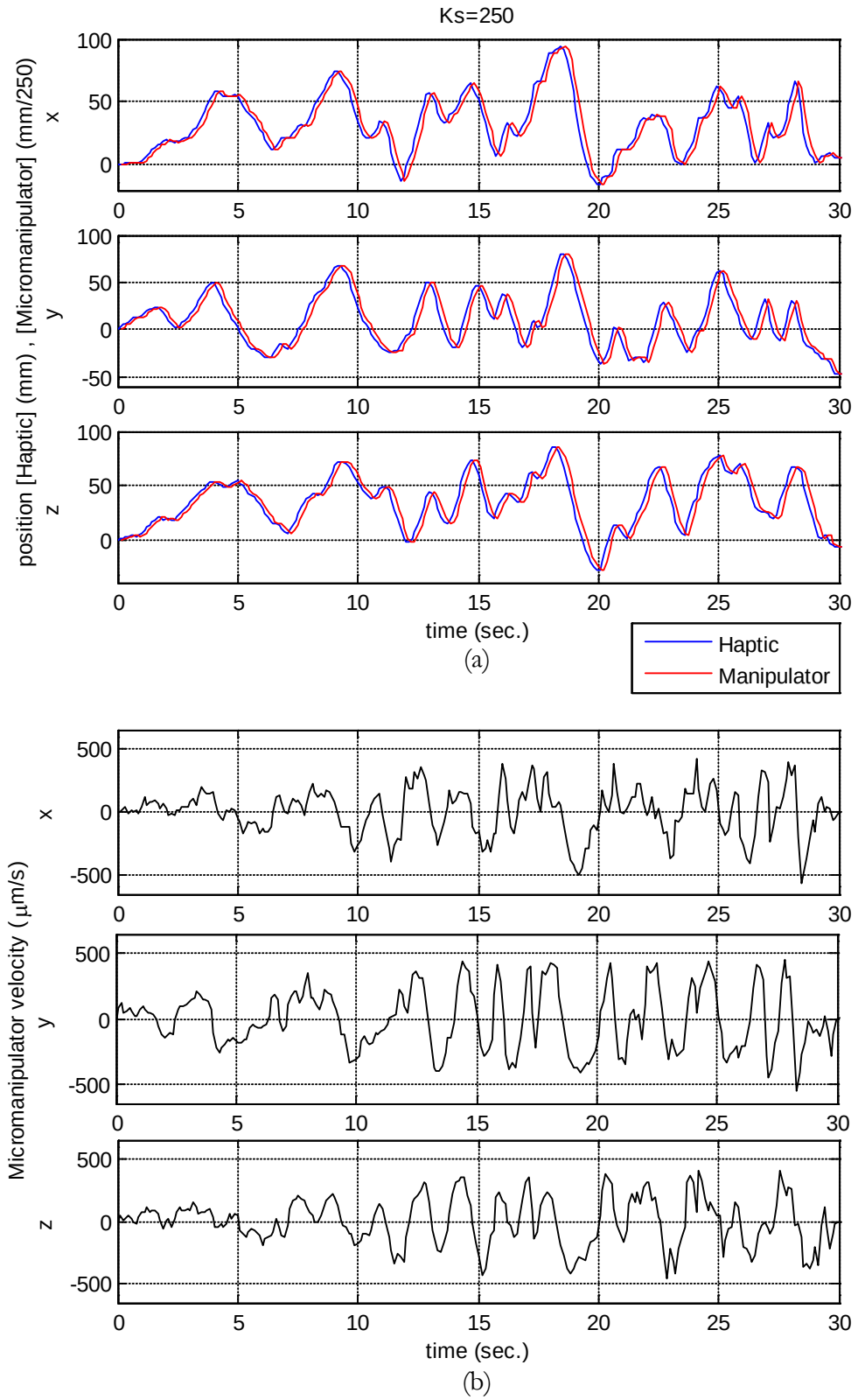

Figure 3.10 Position-to-position mapping framework performance with $K_s = 250$. (a) Position of HIP and tracking trajectory of micromanipulator along x, y and z axes. (b) Corresponding micromanipulator's velocity along x, y and z axes.

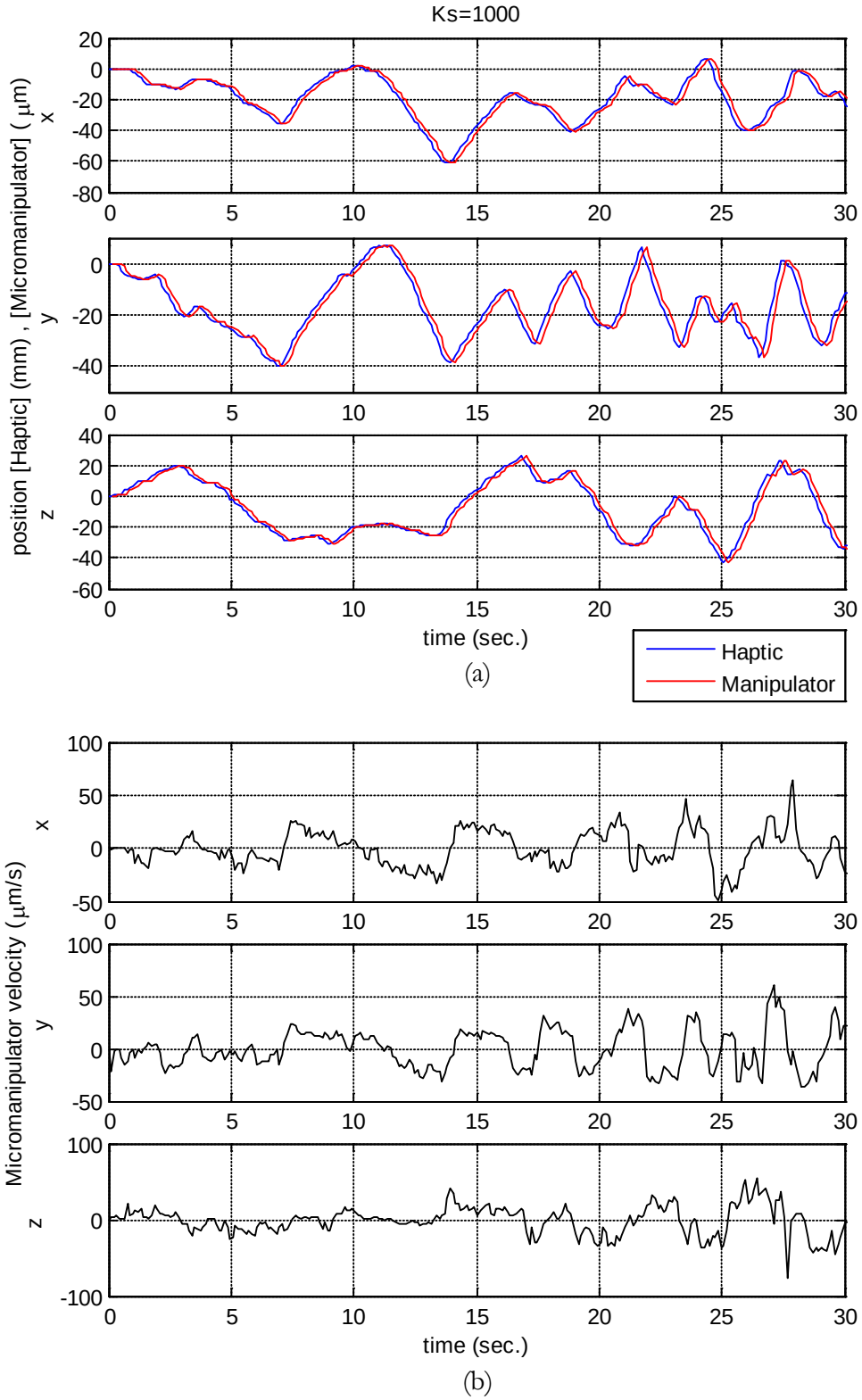

Figure 3.11 Position-to-position mapping framework performance with $K_s = 1000$. (a) Position of HIP and tracking trajectory of micromanipulator along x, y and z axes. (b) Corresponding micromanipulator's velocity along x, y and z axes.

3.2.6 SYSTEM RESOLUTION

The system resolution refers to the overall resolution of the haptically assisted microrobtic system subject to the resolution limitations of the MP-285 micromanipulator and Phantom Omni haptic device. The Phantom Omni haptic device utilizes digital encoders for position sensing corresponding to a nominal position resolution of approximately $0.055mm$ [120]. The MP-285 offers high (fine) and low (coarse) resolution modes providing $0.2\mu m$ and $0.04\mu m$ resolutions respectively [117].

Given the haptic device's fixed resolution of $0.055mm$ when $K_S < 275$ the achievable micromanipulator resolution (system resolution) is dependent on K_S and lies on the curves of Figure 3.12. Both curves of

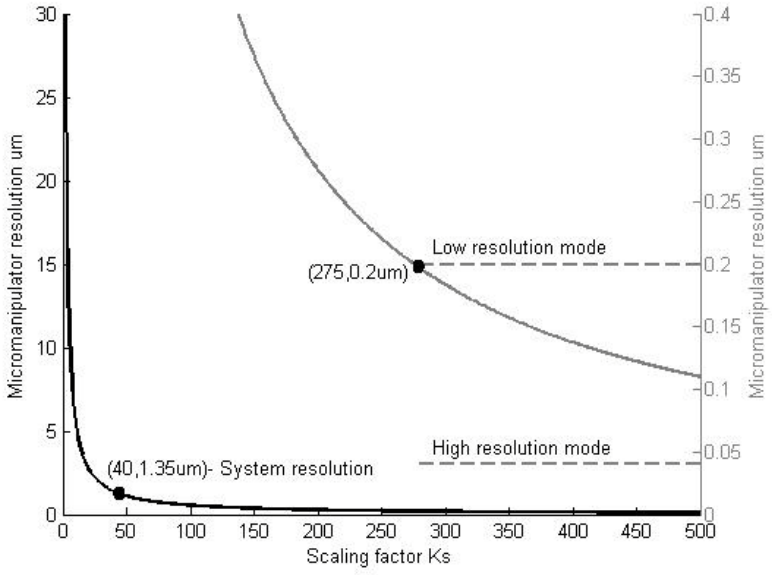

Figure 3.12 Micromanipulator resolution against K_s. When $K_S < 275$ the system resolution is dependent on K_s. Lower left curve shows micromanipulator resolution for values of K_S. Upper right curve, which provides a zoon-in view, shows the system resolution in the range of the micromanipulator's high and low resolution modes. When $K_S \geq 275$ the achievable resolution is governed by the resolution limits of the MP-285 micromanipulator.

Figure 3.12 are the same however the grey curve is for a lower vertical axis range. When operating in the low resolution mode (coarse mode), and $K_S \geq 275$ the achievable system resolution becomes a constant $0.2\mu m$ due to the resolution limits of the micromanipulator, as indicated by the dashed line in Figure 3.12.

The left vertical axis represents micromanipulator resolutions (black curve) down to $K_S = 1.83$ and the right hand vertical axis shows manipulator resolutions approaching those of the manipulator alone.

In order to achieve the highest possible system resolution for a particular application, the following procedure determines a suitable value K_S:

a) Determine the minimum operable cubic volumetric workspace for the micromanipulator (denotes a curve of the Figure 3.7 surface in the $\tau - K_S$ plane)

- Example: With about $500\,\mu m$ radius cell, $3.125\,mm^3$ was established as a suitable volumetric workspace.

b) Determine the maximum practical active cubic workspace for the haptic device (denotes a point on the curve Figure 3.7). This is of particular importance with large workspace haptic devices.

- Example: The entire workspace of the Phantom Omni haptic device ($125mm^3$).

c) The maximum achievable K_S can be determined using expression (3.13). If then desired, K_S can be reduced by reducing the Phantom Omni's workspace.

- Example: $K_s = 40$ corresponds to a $1.35\mu m$ system resolution.

The maximum speed of the micromanipulator is $2.9\, mm/sec$ (achievable in the coarse mode). Observing Figure 3.12, if $K_S < 275$, it is logical to use coarse mode and utilize the maximum micromanipulator speed.

3.3 VIRTUAL TRAINING ENVIRONMENT

Aside from improving real-time operator performance using the physical system, a novel characteristic of the haptic cell injection system introduced in this thesis is also the ability to facilitate virtual offline operator training. Haptic operator training has been explored in many

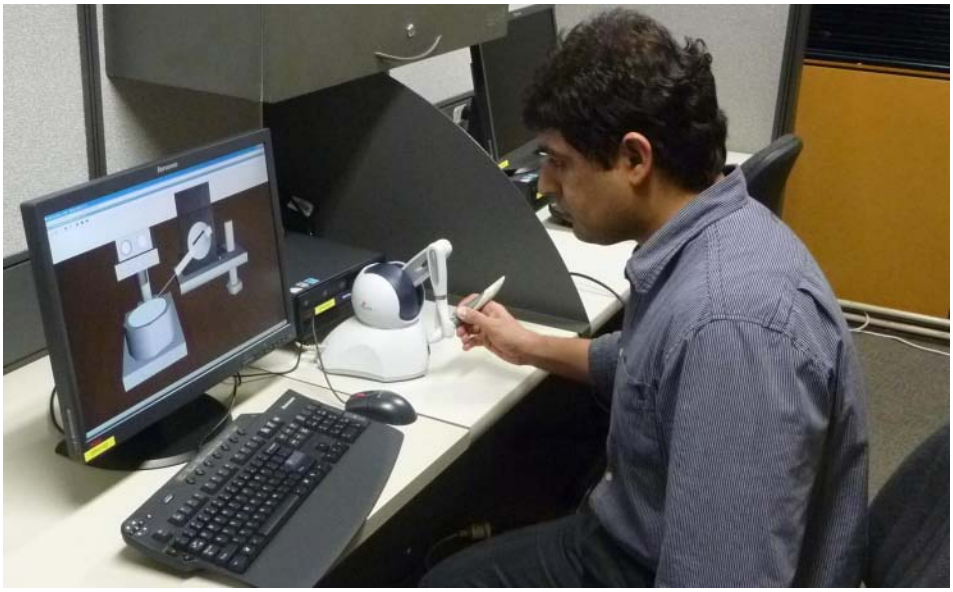

Figure 3.13 Operator training offline using the virtual training environment.

domains including machining tasks [48], surgical training [53-54, 123] and rehabilitation [55]. In this regard, offline training for cell injection can be highly beneficial too. This is facilitated through utilizing the addressed

haptic mapping framework and replicating the micromanipulator and biological cells in a virtual environment. Figure 3.13 shows a bio-operator training with the virtual environment system.

The mapping framework utilized is identical to that of the physical system. The virtual environment was developed in Webots [124] running on Windows 7 PC. The virtual environment is configured for real-time simulation. Figure 3.14 demonstrates the screen shot of the virtual environment.

Figure 3.14 Virtual training environment.

The novelty of the approach is that the virtual environment utilizes the same mapping framework as the physical system addressed in this Chapter, allowing the bio-operator to be trained off-line with similar expericece of operating the real system. After sufficient training, the bio-operator would be moved to the physical cell injection system to utilize his/her training experience to perform a real cell injection operation.

3.4 SUMMARY

This Chapter introduced a haptically enabled microrobotic cell injection system. The approach aims to improve operator performance through the integration of haptic interaction to the cell injection process. Firstly, an experimental setup and the high-level system architecture were presented. Then, a 3D position-to-position kinematic mapping strategy was introduced to provide the operator with the ability to move the micropipette intuitively during intracellular injection. Then the kinematic and workspace analysis of the Phantom Omni and micromanipulator were discussed and the scaling between the two devices was considered. Next, the tracking delay and resolution of the introduced system were analysed. Then, the performance of the approach was examined and the importance of the scaling factor to tracking performance was demonstrated. Finally, a novel approach to replicating the physical cell injection system by a virtual environment was introduced. The addressd mapping framework provides an intuitive method to control the microrobot as well as laying the foundation for rendering haptic guidance to the bio-operator while conducting the cell injection task.

"Love is that condition in which the happiness of another person is essential to your own."

Robert A. Heinlein
1907-1988, American writer

Chapter 4

NEURO-FUZZY MODELING AND CONTROL

The previous Chapter introduced the haptically enabled cell injection system. In order to achieve adequate control of the system, this Chapter focuses on achieving precision control of the micromanipulator.

The manipulator drive positions the micromanipulator by setting a destination position and a fixed velocity which cannot be changed during the positioning task. However, in order to implement the desired position-to-position kinematic mapping, it is necessary to continually reposition the micromanipulator from the current position to the desired position. Achieving this requires the micromanipulator control system to track the trajectory of the haptic device of constantly varying velocity. This Chapter

presents a control system designed to continually reposition the micromanipulator's three actuated axes whilst maintaining micro precision.

In order to design such a controller, an accurate model of the system is required. The micromanipulator system exhibits non-linear behavior and has an unknown internal structure. To overcome these limitations nonlinear system identification methods with black box approaches were investigated. Given the nature of the proposed system, the model required micron resolution accuracy. Non-linear system identification techniques such as Hammerstein-Wiener's blind model identification approach [125] were investigated but found ineffective in achieving desired accuracy.

ANNs (artificial neural networks) and FISs (fuzzy inference systems) are universal approximators. NFSs (neuro-fuzzy systems) which combine the advantages of fuzzy and neuro-learning have become a popular solution to modeling problems. Integration of ANN and FIS combines the advantages of symbolic and numerical processing [126].

NFS was first introduced in the late 1980s and the 1990s saw the development of diverse approaches. These approaches can be categorized to three classes of cooperative, concurrent and fused [127]. The most common class is the fused NFS which employs an ANN to train internal parameters of a fuzzy structure. Notably Jang [128] introduced a fused NFS architecture ANFIS (adaptive neuro-fuzzy inference system) able to approximate linear and non-linear functions (universal approximator).

Intelligent control has proven to be a practical alternative to conventional control schemes [129]. This is because fuzzy control and neural network-based control systems are able to deal more effectively with variations of parameters, uncertainty and the unknown structure of

the system under control. This results in improved robustness of the control system. A fuzzy control scheme can be enhanced to an adaptive network controller (ANFIS) providing the advantages of ANNs and fuzzy control schemes[130].

This Chapter addresses neuro-fuzzy modeling and control of the microrobotic system based on ANFIS, Adaptive Neuro-Fuzzy Inference System. As ANFIS has a ruled based structure, compare to conventional ANN, it is easier to be implemented in low level programming and is computationally more efficient in real-time. In addition, by taking advantage of its network based structure and hybrid learning method, a self-structuring and training platform is formed. It provides a systematic method to create and train the network from selecting the best input set, choosing optimum number of fuzzy rules, nodes and parameters to well tuning of network parameters.

4.1 ADAPTIVE NEURO-FUZZY INFERENCE SYSTEM

4.1.1 ARCHITECTURE

ANFIS presents an appropriate combination of ANN and FIS. The theory relating to FISs propose that different fuzzification and defuzzification methods as well as different rule bases can propose diverse solutions to a particular task [131]. Consider the two fuzzy rules of Takagi and Sugeno-type FIS as:

Rule 1: If x is A1 and y is B1, then f1 = p1x+q1y+r1.

Rule 2: If x is A2 and y is B2, then f2 = p2x+q2y+r2. (4.1)

where, x and y are inputs, f is the output, $\{A_i, B_i\}_{i=1,2}$ is linguistic label set, and $\{p_i, q_i, r_i\}_{i=1,2}$ is the parameter set. Then, type-3 ANFIS architecture with first-order Sugeno fuzzy inference system [132] would be illustrated as Figure 4.1 (a).

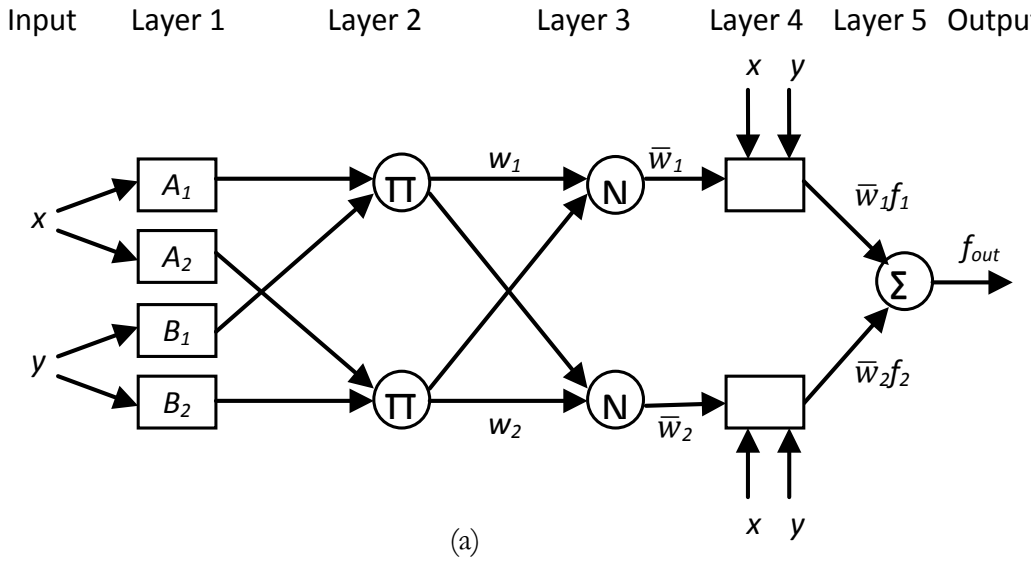

(a)

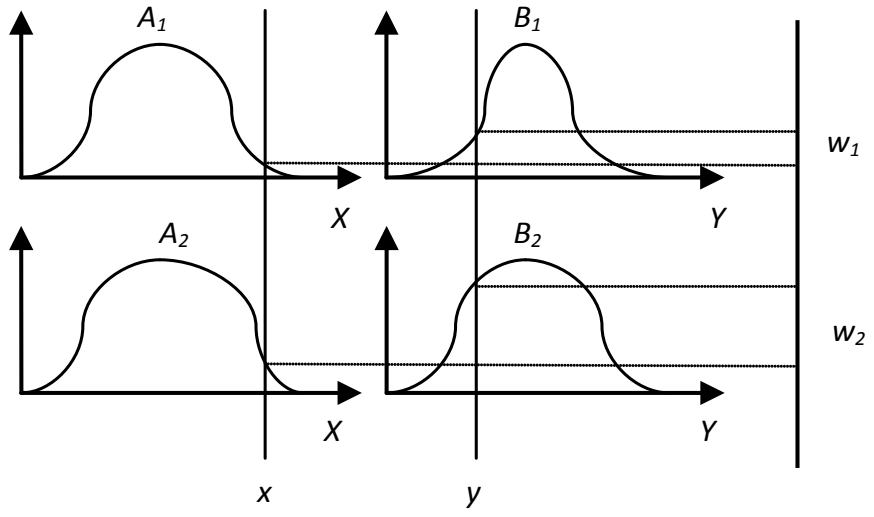

(b)

Figure 4.1 ANFIS architecture. (a) The ANFIS model using Sugeno's fuzzy inference method for two rules. Π multiplies the incoming signals and sends the product out; N normalizes the weights; Σ sums up the incoming signals and produces the overall output. (b) Fuzzy inference mechanism.

Figure 4.1 (b) demonstrates the fuzzy reasoning mechanism which infers the output f from the input vector [x , y]. The firing strengths w_1 and w_2 are calculated as a product of the membership grades of the parameters. The system output is then obtained as the weighted average of each rule's output. More precisely, the output f can be calculated as

$$f = \frac{w_1 f_1 + w_2 f_2}{w_1 + w_2} = \bar{w}_1 f_1 + \bar{w}_2 f_2 \tag{4.2}$$

substituting from (4.1)

$$f = \frac{\mu_{A_1}(x)\mu_{B_1}(y)(p_1 x + q_1 y + r_1) + \mu_{A_2}(x)\mu_{B_2}(y)(p_2 x + q_2 y + r_2)}{\mu_{A_1}(x)\mu_{B_1}(y) + \mu_{A_2}(x)\mu_{B_2}(y)} \tag{4.3}$$

where $\mu_{A_1}(x), \mu_{B_1}(y), \mu_{A_2}(x)$, and $\mu_{B_2}(y)$ are membership grades of A_1, B_1, A_2 and B_2 respectively.

The ANFIS network is comprised of 5 layers. Square and circle node symbols represent functional and operational nodes respectively. Network lines do not carry any weight and are simply transfer values to the next layer. Node functions in the same layer are of the same function family. Layers are defined as follows:

- *Layer-1:* Each node i in this layer is a square type which generates membership grades of a linguistic label:

$$O_i^1 = \mu_{A_i}(x) \tag{4.4}$$

$\mu_{A_i}(x)$ represents the MF (membership function) of the linguistic label A_i. In this thesis, membership functions have to be bell-shaped with the range of $[0,1]$:

$$\mu_{A_i}(x) = \left[1 + \left|\frac{x - c_i}{a_i}\right|^{2b_i}\right]^{-1} \tag{4.5}$$

where x is the input node i, A_i is the linguistic label corresponding to this node function and $\{a_i, b_i, c_i\}$ is the parameter set that changes the shape of MF. Parameters in this layer are referred as *premise parameters*.

- *Layer-2:* Each node in this layer is a circular node labeled $\prod$. The firing strength of each node is calculated through multiplication:

$$O_i^2 = w_i = \mu_{A_i}(x)\mu_{B_i}(y) \tag{4.6}$$

- *Layer-3:* Each node in this layer is a circular node labeled *N*. The *i*th node of this layer calculates the ratio of the *i*th rule's firing strength to the sum of all rule's firing strengths:

$$O_i^3 = \bar{w}_i = \frac{w_i}{w_1 + w_2}, \qquad i = 1,2 \tag{4.7}$$

Output of this layer is referred to as *normalized firing strengths*.

- *Layer-4:* Each node in this layer is a square node with a node function:

$$O_i^4 = \bar{w}_i f_i = \bar{w}_i(p_i x + q_i y + r_i) \tag{4.8}$$

where $\bar{w}_i$ is the output of preceding layer, and $\{p_i, q_i, r_i\}$ is the parameter set. Parameters in this layer are called *consequent parameters.*

- *Layer-5:* The single node in this layer is a circle node labeled $\sum$. It calculates the overall output as the summation of all incoming signals:

$$O_i^5 = overall\ output = \sum_i \bar{w}_i f_i = \frac{\sum_i w_i f_i}{\sum_i w_i} \tag{4.9}$$

A five layered adaptive network which functions as a type-3 fuzzy inference system has been developed. In summary, layer 1 calculates the membership grades; layer 2 combines them to form the firing strengths; layer 3 normalizes them; layer 4 constructs the contribution from each rule; and layer 5 generates the final output.

4.1.2 HYBRID LEARNING ALGORITHM

Assume an adaptive network with single output:

$$output = F(\vec{I}, S) \tag{4.10}$$

$\vec{I}$: set of input variables

S: set of parameters.

If there exists a function H such that the composite function $H\ o\ F$ is linear in some of the elements of S, then these elements can be identified by the

LSE (least squares estimate) method [128]. More explicitly, if the parameter set S can be decomposed into two sets

$$S = S_1 \oplus S_2 \tag{4.11}$$

where $\oplus$ represents direct sum, such that $H\ o\ F$ is linear in the elements of S_2, after applying H to expression (4.10) , we have

$$H(output) = HoF(\vec{I}, S) \tag{4.12}$$

which is linear in the elements of S_2. Now using the element values of S_2, training data can be supplied into expression (4.12) to obtain a matrix equation:

$$AX = B \tag{4.13}$$

where X is an unknown vector whose elements are parameters in S_2. The sequential formulas can be employed to calculate the LSE of X [133].

It can be shown that in an ANFIS network, given the values of premise parameters, the overall output can be rewritten as a linear combination of the consequent parameters. From expression (4.12)

$$f = \overline{w}_1 f_1 + \overline{w}_2 f_2 \tag{4.14}$$

$$= (\overline{w}_1 \mathrm{x})p_1 + (\overline{w}_1 \mathrm{y})q_1 + (\overline{w}_1)r_1 + (\overline{w}_2 \mathrm{x})p_2 + (\overline{w}_2 \mathrm{y})q_2 + (\overline{w}_2)r_2$$

This clearly indicates that f is linear in the consequent parameters $\{p_i, q_i, r_i\}_{i=1,2}$. As such, from expression (4.11) where

S = set of total parameters,

S_1 = set of premise parameters,

and S_2 = set of consequent parameters,

H and F are the identify and fuzzy inference system functions respectively.

In summary, linear parameters which exist in layer 4 are identified using the LSE method. In contrast, layer 1 parameters are nonlinear and back-propagation gradient decent is used to update them. This reflects the hybrid learning algorithm concept which combines the gradient decent and the LSE methods to train the ANFIS network. Each epoch of the learning algorithm is performed in two passes:

- *Forward pass:* input data is supplied and functional signals go forward up until layer 4 to calculate each node output until the matrices A and B in expression (4.13) are obtained, and the parameters in S_2 (consequent parameters) are identified by LSE method.

- *Backward pass:* error rates propagate backward and the premise parameters are updated by the gradient descent method.

4.2 NEURO-FUZZY MODELING

The micromanipulator's 3 actuated DOF provide a travel range of 25 mm along the corresponding Cartesian axes (Table 3.1). They can be positioned independently and, as such, the micromanipulator is modelled for each individual axis.

Figure 4.2 illustrates the control system architecture. The controller sends commands to the micromanipulator through a DAQ NI card in the form of voltage level (in range of -2.5 to 2.5 V) and receives the position feedback through the PC serial port.

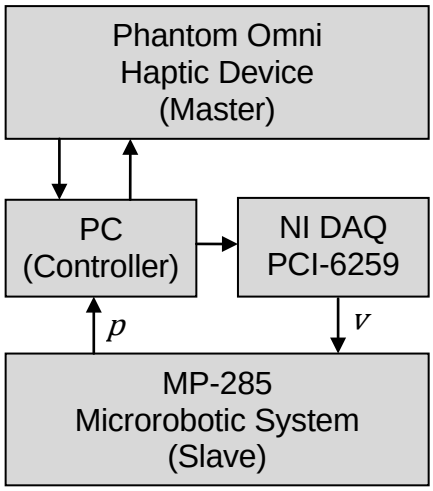

Figure 4.2 Control system architecture. v and p are the voltage level and position feedback respectively.

The system identification problem is to model the behavior of the microrobotic system where voltage and position along each axis are designated as the system input $u(t)$ and output $y(t)$ respectively. As the micromanipulator operates in different modes (fine and coarse), an independent model needs to be considered for each mode.

Figure 4.3 shows the microrobotic system's response for one axis when the voltage increases linearly from -2.5 to 2.5 V over 1000 ms. The system is in the fine operating mode and the Figure demonstrates the nonlinear behavior of the system.

The first step in system identification is to collect input-output data pairs which represent the behavior of the system as best as possible. The

input was chosen to be a random binary signal shifting between -2.5 and 2.5 V. 3134 input-output data pairs with sampling time of 19.2 ms were collected from the system. Figure 4.4 and Figure 4.5 show these input-output data pairs in the fine and coarse modes respectively. The collected data pairs were split into two equal sets with an equal amount of data for training and checking.

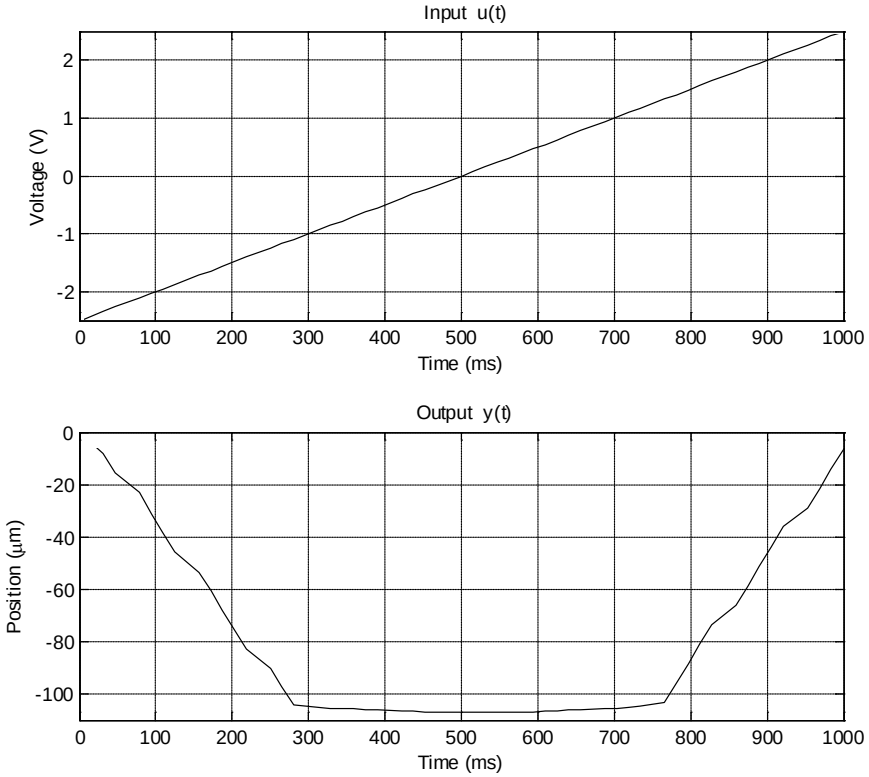

Figure 4.3 Microrobotic system response p to the input voltage v.

The next step is input selection for the ANFIS model. It is necessary to determine which variables should constitute the input arguments to the ANFIS model. The objective of the system identification is to extract a dynamic process model to predict the output $y(t)$. To achieve this some historical input and output system data is considered as well. The input candidates are partitioned into two disjoint sets as follows:

$$Y = \{y(t-1), y(t-2), y(t-3), y(t-4)\} \tag{4.15}$$

$$U = \{u(t-1), u(t-2), u(t-3), u(t-4), u(t-5), u(t-6)\} \tag{4.16}$$

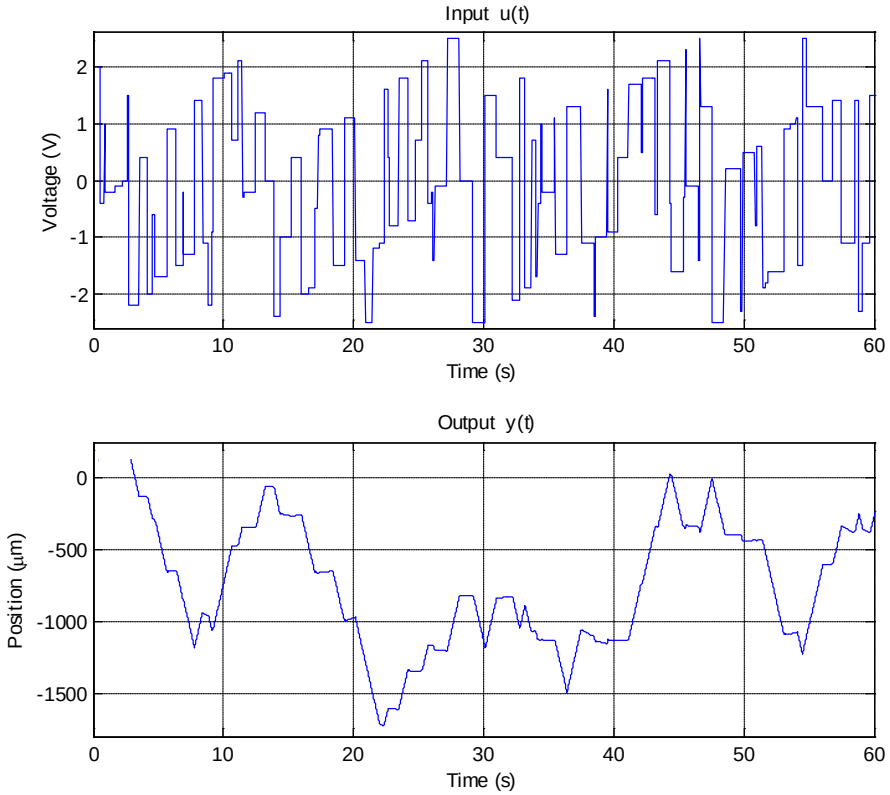

Figure 4.4 Input-output data pairs while the micromanipulator is set to fine mode.

As discussed in the previous section, ANFIS uses the hybrid learning method which combines gradient descent and LSE methods. The LSE method is the major contribution to fast training. In contrast, the gradient descent slowly changes the underlying membership functions which create the basis functions for the LSE method. As a result the ANFIS is able to achieve relatively satisfactory results even after the first training epoch (immediately after the first application of LSE).

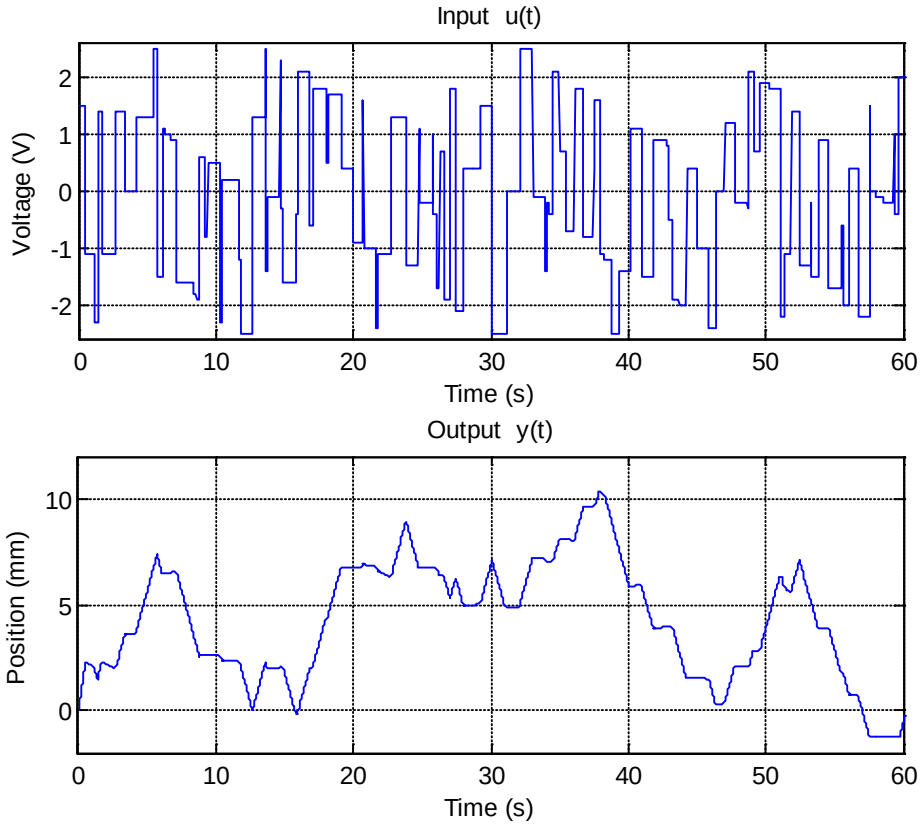

Figure 4.5 Input-output data pairs while the micromanipulator is set to coarse mode.

The LSE method is computationally efficient allowing the construction of ANFIS models with various combinations of input candidates, to run a single training epoch, and to select the one with the best performance based on smallest RMSE (root mean square error).

Two approaches are employed to select appropriate inputs: heuristic and exhaustive searching on all possible combinations of the input candidates [134].

In the heuristic approach, all input candidates are treated equally and the best input arguments are selected sequentially. Because there are 10 input candidates, first, 10 ANFIS models with single input of each were

constructed. Then, the single input model with the smallest training error was selected. Next, the best model out of 9 possible two-input ANFIS models were chosen.. It was observed the three-input ANFIS model provided reasonably low RMSE where beyond this number of inputs, the RMSE did not decrease considerably. As such, the optimum three-input ANFIS model was selected. Next step was to train the network in order to obtain the form of input space partitioning, the members and type of membership functions.

For the model inputs, two generalized bell membership functions (expression (4.5)) were assigned. Grid partitioning method was employed to tune the membership functions. The number of fuzzy rules was 2^n where n is the number of input arguments. Each ANFIS model was trained for a single epoch to identify consequent parameters. These parameters indicated each rule's output equation. When n reached to 3, the smallest RMSE of 1.2444 and 0.0113 in fine and coarse modes respectively was obtained. It was observed, by proceeding, the RMSE did not decrease considerably any more. As such, the training stopped at this point to avoid unnecessary increase of the input dimension.

Figure 4.6 illustrates error curves for the input selection process for the heuristic approach. The selected inputs are listed according to the order of decreasing training errors.

The exhaustive approach, as its name indicates, performs an exhaustive search of all possible combinations of input candidates. To find the most influential 3 inputs out of 10 candidates (to be the inputs to the ANFIS) in expressions (4.15) and (4.16), $C_3^{10} = 120$ ANFIS models were

constructed and trained with a single epoch. It was found the result is quite identical to the heuristic approach.

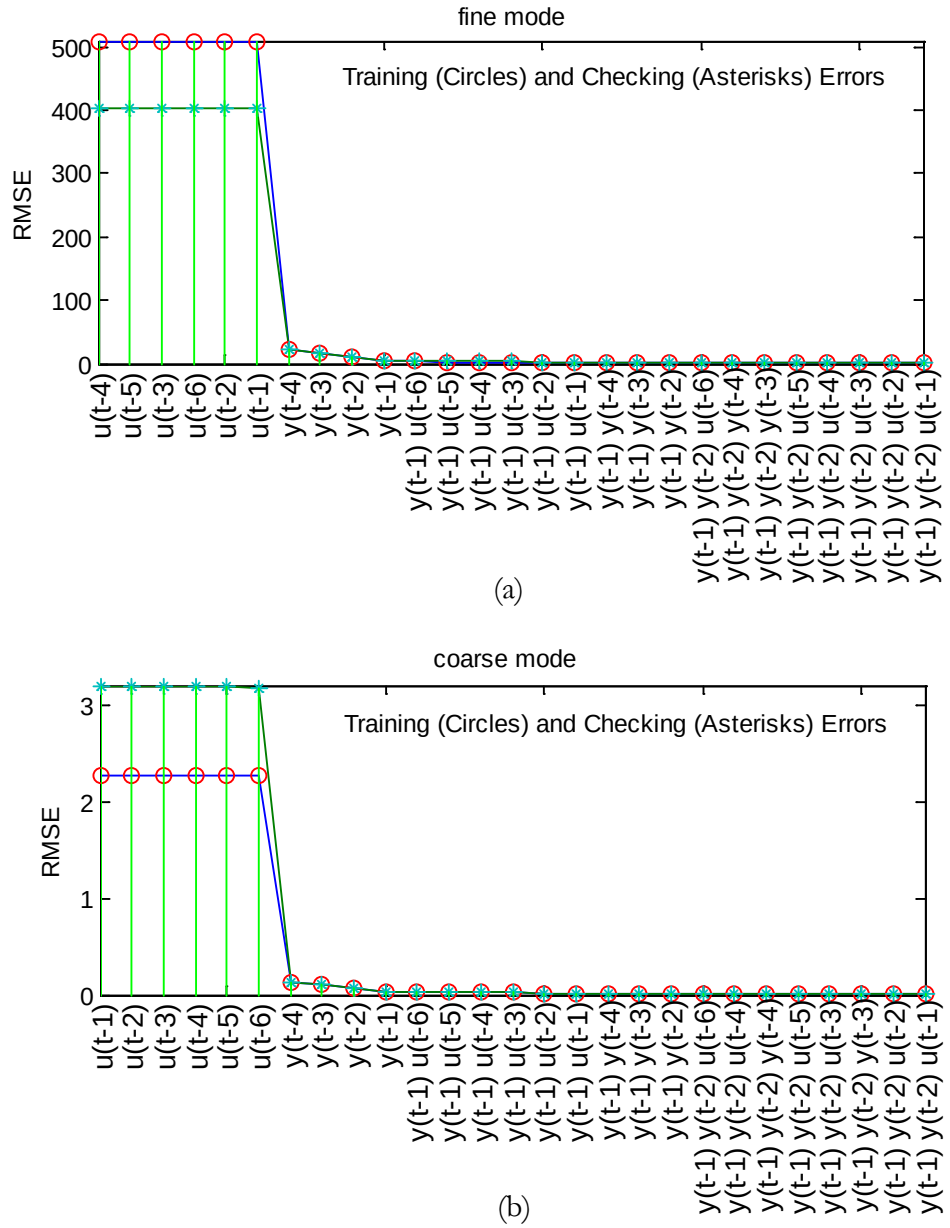

Figure 4.6 Error curves for input selection in heuristic approach while the micromanipulator is operating in (a) fine mode, and (b) coarse mode.

Figure 4.6 demonstrates the performance of the 36 ANFIS models of the heuristic approach ordered based on decreasing training errors for both the fine and coarse modes.

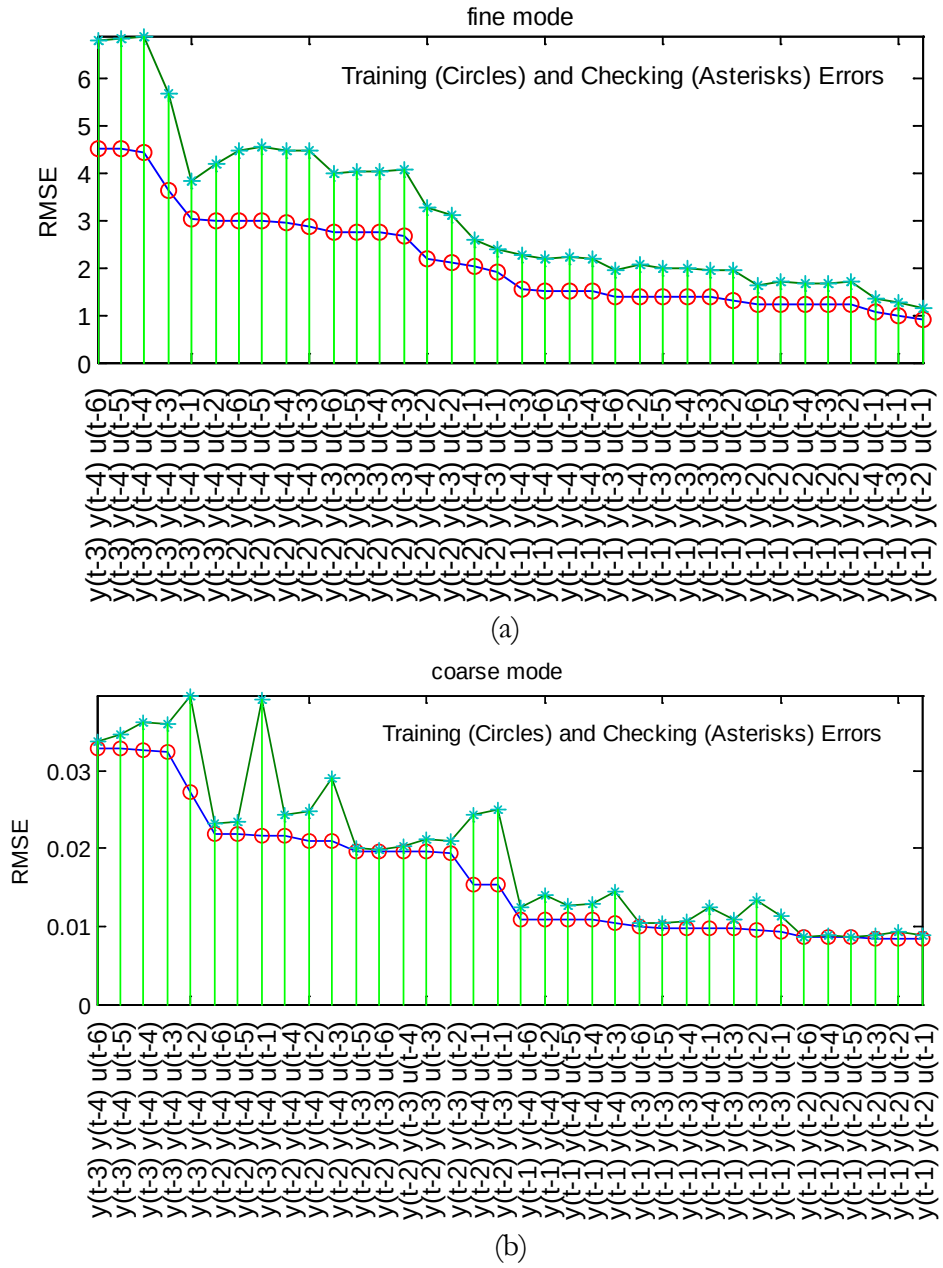

Figure 4.7 Error curves for input selection in exhaustive approach while the micromanipulator is operating in (a) fine mode, and (b) coarse mode.

Figure 4.7 shows same input selection procedure using the exhaustive approach where the last 36 ANFIS models are shown and ordered based on decreasing training errors.

As the figures indicate, the ANFIS model with the input set of $\{y(t-1), y(t-2), u(t-1)\}$ had the smallest error. As such it was selected

as the ANFIS model of the system. The selected model had 8 fuzzy rules, 34 nodes, 32 consequent parameters and 18 premise parameters. The input selection procedure took 56 and 51 seconds on a PC (Core i7, 1.6 GHz and 6 GB RAM) for the fine and coarse modes respectively.

The next step of the ANFIS model training is to tune premise parameters using the hybrid method. Training stop criteria is defined as the point which convergence occurs and by continuing the training, RMSE does not reduce anymore. In fine mode, it was observed that after epoch number 5366, RMSE for training data set converged which was considered as the training stop point. At this point, RMSE for training and checking data set were reduced from 0.9163 to 0.8412 and from 1.0953 to 1.0228 respectively. In coarse mode, RMSE for training data set converged at epoch number 50107. At this point, RMSE for training and checking data set were reduced from 0.008432 to 0.008343 and from 0.0113 to 0.0108 respectively. Figure 4.8 illustrates the response of the model in fine mode. Figure 4.8 (a) shows the response of the model to the training data set. The corresponding prediction error is very small and is presented in Figure 4.8 (b). Figure 4.8 (c) demonstrates that while checking data is applied, the trained ANFIS model was able to predict system response precisely. Figure 4.8 (d) shows the corresponding perdition errors. As the results indicate, the developed model was able to precisely predict the microrobotic system's response with RSME of 1.0224 μm when the microrobot was set to fine mode and was moving in a cm range (10^4 times). Figure 4.9 illustrates the model's response when the microrobot was operating in the coarse mode. It is demonstrated that the model provides a RSME of 0.0083426 mm in response to the training data (Figure 4.9 (a)) and 0.010777 mm to the checking data (Figure 4.9 (c)). The corresponding

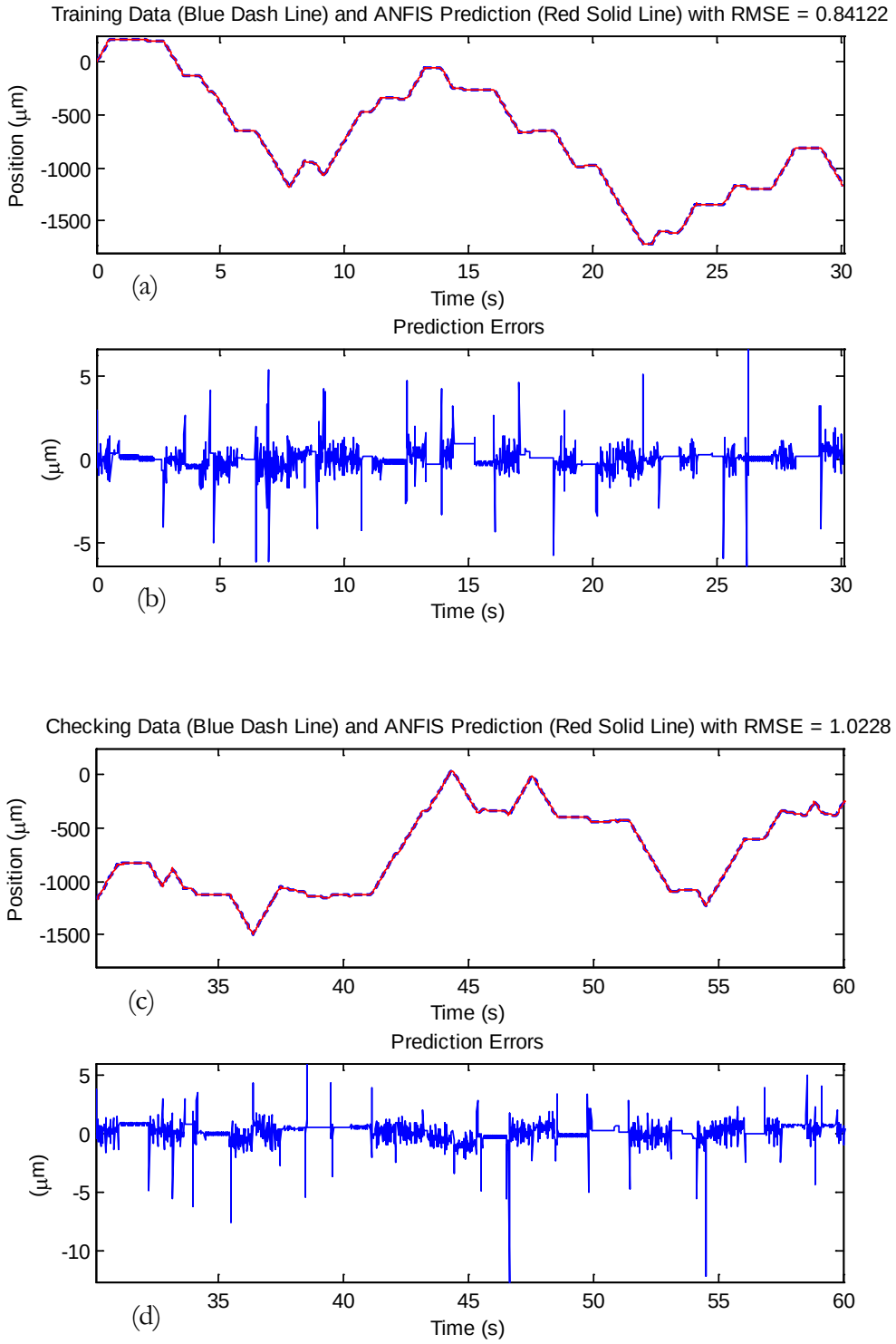

Figure 4.8 Trained ANFIS model response and corresponding prediction error in fine mode. (a) Training data (blue dash line) and position prediction of trained ANFIS (red solid line). (b) Corresponding prediction error. (c) Checking data and position prediction of trained ANFIS. (d) Corresponding prediction error.

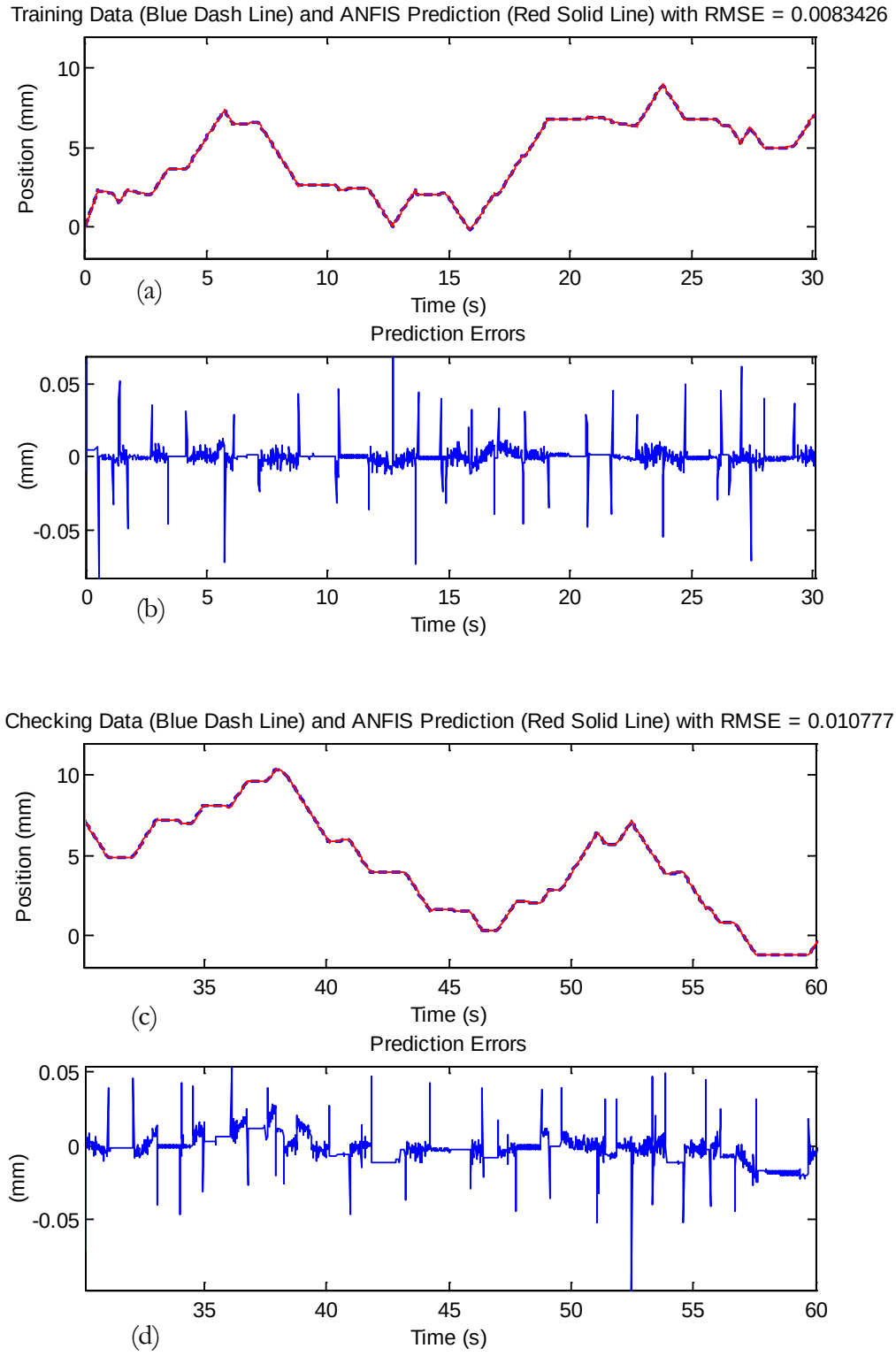

Figure 4.9 Trained ANFIS model response and corresponding prediction error in coarse mode. (a) Training data (blue dash line) and position prediction of trained ANFIS (red solid line) (b) Corresponding prediction error. (c) Checking data and position prediction of trained ANFIS. (d) Corresponding prediction error.

prediction errors are shown in Figure 4.9 (b) and Figure 4.9 (d) respectively.

These results suggest that the developed model is accurate for both fine and coarse modes of operation. This is a necessary step in the design of an accurate controller for the microrobotic system.

4.3 NEURO-FUZZY CONTROL

To design the controller, the direct inverse learning method [135-136] was employed. Inverse learning or general learning for control was performed in two phases:

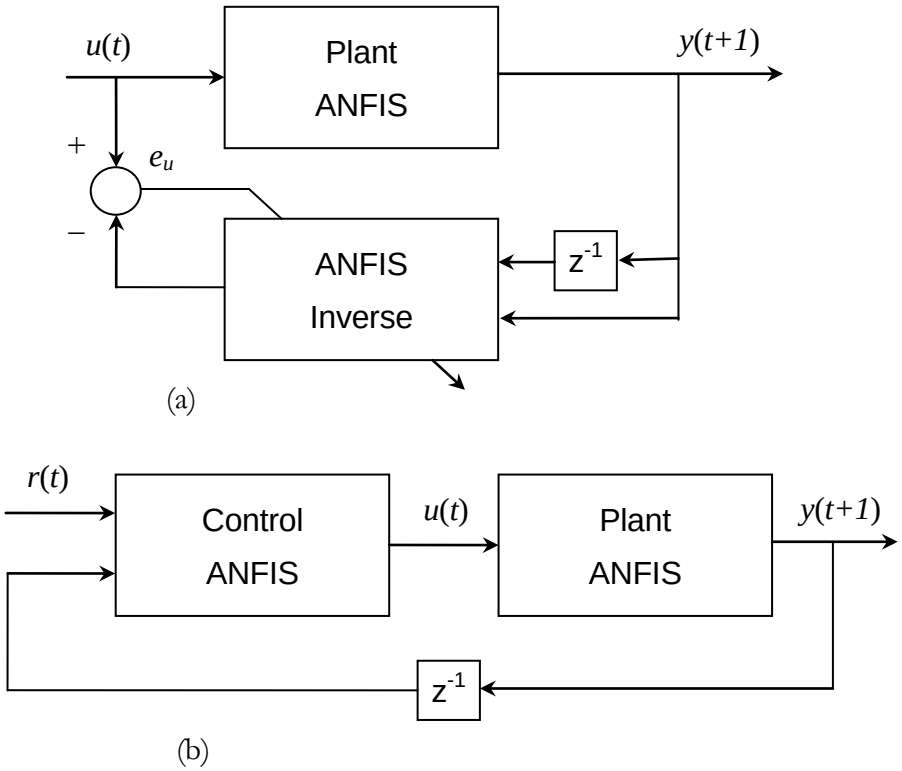

Figure 4.10 Block diagram of inverse control method. (a) training phase (b) application phase.

- *Learning phase:* the plant ANFIS inverse model was derived based on input-output data pairs generated from the plant ANFIS (Figure 4.10 (a)).

- *Application phase:* the obtained ANFIS inverse model was used to generate the control action as depicted in Figure 4.10 (b).

These two phases was proceeded simultaneously aligning with classical adaptive control schemes.

For the offline mode, a set of training data pairs was collected and the ANFIS network was then trained in the batch mode. For the online mode, in order to deal with time varying dynamics and model inaccuracies, the control actions were generated every *n* time steps while online learning occurs at every time step. Alternatively, it is possible to generate the control sequence at every time step and apply only the first component to the plant. The overall control structure is illustrated in Figure 4.11.

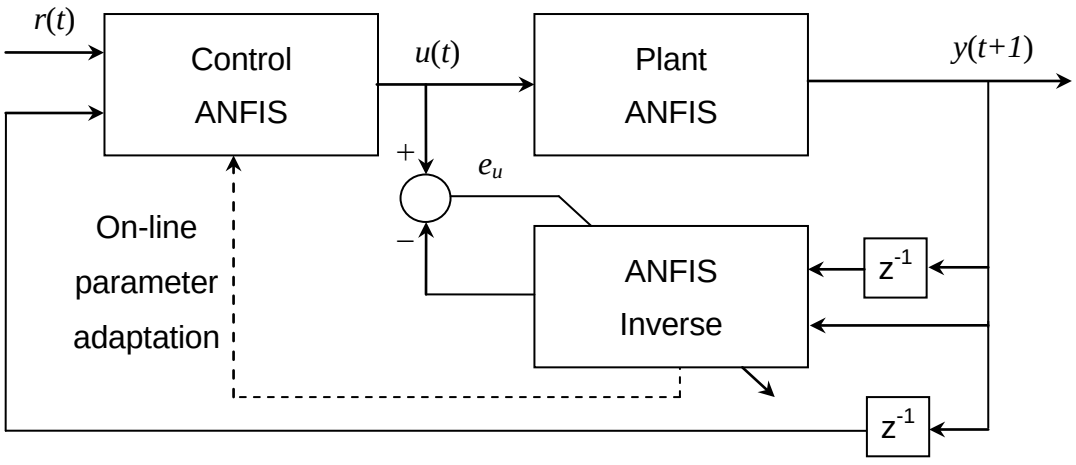

Figure 4.11 Block diagram of adaptive learning. On-line learning of ANFIS inverse model occurs at each time step to fine-tune the membership function parameters of ANFIS controller.

The premise of inverse control is to drive the plant with a signal from a controller whose transfer function is the inverse of the plant itself. As such, the role of inverse method is to adjust the ANFIS controller parameters to create the plant's inverse ANFIS model.

The plant can be described by

$$y(t+1) = f\,(y(t\,), u(t\,)) \tag{4.17}$$

where $y(t+1)$ is the plant state at time $t+1$, $y(t)$ is the system state at time t, and $u(t)$ is the control signal at time t. Accordingly, the state vector at time $t+2$ is

$$\begin{aligned} y(t+2) &= f\,\big(y(t+1), u(t+1\,)\big) \\ &= f\,\big(f\big(y(t), u(t\,)\big), u(t+1\,)\,\big) \end{aligned} \tag{4.18}$$

In general

$$y(t+n) = F\,(y(t\,), U) \tag{4.19}$$

where n is the order of the plant, F is a multiple composite function of f, and U holds the control actions from t to $t+n-1$

$$U = (u(t\,), u(t\ +1), \ldots, u(t+\ n\ -1))^T \tag{4.20}$$

The updating expression (4.19) for y indicates that the sequence of control inputs drives $y(t)$ to $y(t+n)$ in n time steps. With the assumption of the plant model inverse existence, then U can be expressed as a function of $y(t)$ and $y(t+n)$

$$U = G\,(y(t\,), y(t+n)) \tag{4.21}$$

The problem is to find the inverse model G. The ANFIS network is then used to learn the inverse of the plant, G, by fitting the data pairs $(y(t), y(t\ +1); u(t\,))$. Then, the training data pairs would be

$$\{\, y(t), y(t+n); U^T\}. \tag{4.22}$$

The learning phase is used to approximate G with G_{est} where the training data set (4.22) is collected and applied to train the ANFIS network. After the neuro-fuzzy controller is trained to approximate the inverse dynamic of G, if $y(t)$ and the desired reference $r(t+n)$ are given, the neuro-fuzzy controller generates a sequence of control actions

$$U_{est} = G_{est}(y(t), r(t+n)) \tag{4.23}$$

This control sequence brings $y(t)$ to the desired reference $r(t+n)$ after n steps. 1500 training data sets and 1500 checking data sets were used to develop the ANFIS inverse model for the fine and coarse modes. The ANFIS inverse model has 8 fuzzy rules, 34 nodes, 32 consequent parameters and 18 premise parameters. For the fine mode, after epoch number 4366, RMSE for the training data set converged. At the end of the learning phase, the RMSE for training and checking data set were reduced from 0.8296 to 0.7462 and from 1.0847 to 1.0153 respectively. For the coarse mode, the RMSE for the training data set converged at epoch number 50107. In this mode, the RMSE for training and checking data set reduced from 0.009611 to 0.008758 and from 0.0156 to 0.0124 respectively. This indicates that the inverse model does exist and the direct inverse learning method is capable of accurate approximation.

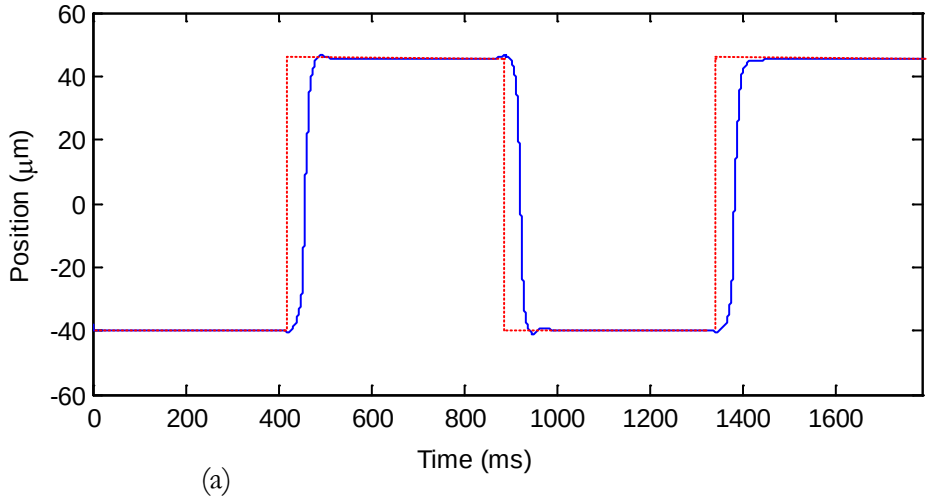

(a)

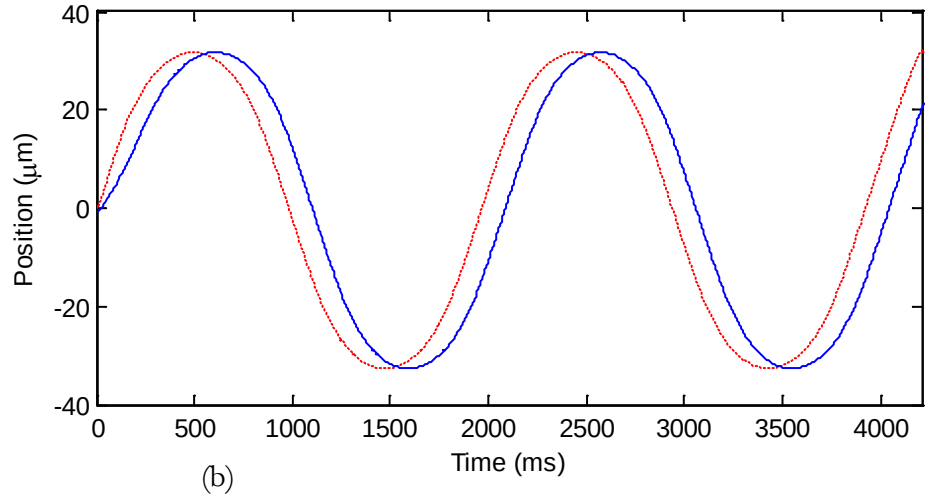

(b)

Figure 4.12 Control system response to the desired trajectory. (a) Square wave response in coarse mode. (b) Sinusoidal wave response in fine mode. Dashed red line and solid blue line indicate desired trajectory and control system actual responses respectively.

The developed control scheme was utilized for each of the manipulator's three actuated axes. The control system was implemented on the PC within the VC++ environment deployed from MATLAB©. The controller sends commands to the manipulator through a DAQ NI card in the form of voltage levels and receives the position feedback through the PC's serial port. Figure 4.12 depicts the controller's real-time response to

the desired square and sinusoidal wave trajectories. The control system needs to approach the desired position as fast as possible with high precision while minimising the overshoot and undershoot. The results indicate the high performance of the control system when approaching the desired position.

Prior to development of the introduced neuro-fuzzy controller, a PID controller was designed and was tuned using the Ziegler-Nichols' (ZN) method. Table 4.1 and Table 4.2 compare the PID and NF (neuro-fuzzy) controllers' transient-response characteristics in coarse and fine modes when moving the micromanipulator from P_1 to P_2 as follows

$$\begin{aligned} P_1 &= \left(P_{1x}, P_{1y}, P_{1z}\right) = \ (696, 162.7, 388)\ \mu m \\ P_2 &= (P_{2x}, P_{2y}, P_{2z}) \ = \ (429.3, 312, 578.6)\ \mu m \end{aligned} \tag{4.24}$$

As indicated by Table 4.1 and Table 4.2, the neuro-fuzzy controller achieves higher performance for all transient response characteristics in both the coarse and fine modes. Also, the settling time of the neuro-fuzzy controller is much less than the PID controller. This corresponds to faster positioning and provides less delay for master/slave architecture subject to different scaling factors. The MPO (Maximum Percent Overshoot) is also smaller corresponding to more control precision. The neuro-fuzzy controller shows much higher performance, especially in fine mode, as indicated by Table 4.2. Given these considerations the neuro-fuzzy controller is the superior choice for micropositioning in this work.

Controller	Axis	P_1 (μm)	P_2 (μm)	$\lvert P_1 - P_2 \rvert$ (μm)	MPO (%)	t_d (ms)	t_r (ms)	t_s (ms)
PID	x	696	429.3	266.7	4.01	180	370	580
NF					2.03	120	230	270
PID	y	312	162.7	149.3	2.54	130	260	440
NF					1.05	100	190	230
PID	z	388	578.6	190.6	3.67	160	320	440
NF					2.01	110	210	240

Table 4.1 Transient-response characteristics comparison of the PID and NF controllers in coarse mode. P_1 is the start position, P_2 is the desired position, MPO is the Maximum Percent Overshoot, t_d is the delay time (the time required for the response to reach half the desired value), t_r is the rise time (the time required for the response to reach the desired value) and t_s is the settling time (the time required for the response to reach and stay within %2 of the final value).

Controller	Axis	P_1 (μm)	P_2 (μm)	$\lvert P_1 - P_2 \rvert$ (μm)	MPO (%)	t_d (ms)	t_r (ms)	t_s (ms)
PID	x	696	429.3	266.7	2.81	1300	1390	2690
NF					1.42	930	530	770
PID	y	312	162.7	149.3	1.78	1000	710	1820
NF					0.74	810	280	530
PID	z	388	578.6	190.6	2.57	1180	1080	1820
NF					1.41	870	400	590

Table 4.2 Transient-response characteristics comparison of the PID and NF controllers in fine mode.

4.4 SUMMARY

The haptically enabled system is required to manipulate the microrobot with high accuracy. This requires a control strategy capable of continually repositioning the microrobots' actuated axes whilst maintaining micro precision. This Chapter addressed the design of a precision control system for the microrobotic cell injection system. As the microrobotic system has

an unknown internal structure with nonlinear behaviour, an intelligent dynamic modelling and control scheme was developed. An ANFIS (neuro-fuzzy inference system) and direct inverse learning method were adapted for system identification and control. It was demonstrated that the developed ANFIS model can predict the system's response precisely. Experimental results indicated that the designed intelligent controller provides adequate control characteristics in term of precision and speed which are both important for haptic microrobotic system to perform the cell injection task. This provides the suitable platform for 3D position-to-position kinematic mapping of the haptic/microrobotic system.

"Life is what happens to you while you're busy making other plans."

John Lennon
1940-1980, English musician & singer

Chapter 5

HAPTIC GUIDANCE

Previous Chapters focused on the underlying capabilities necessary to haptically augment the bio-operator's control of the cell injection process. This is the basis for the bio-operator to receive haptic assistance/feedback while retaining ultimate control of the micromanipulator during the cell injection task.

This Chapter builds upon these capabilities, allowing the bio-operator to intuitively control the micropipette's motion while virtual fixtures provide haptic guidance during the cell injection task.

5.1 HAPTIC VIRTUAL FIXTURES

Virtual fixtures aim to guide operator motions within a virtual environment, including conforming to a range of geometries and influencing motion along a desired trajectory. Haptic virtual fixtures operate by applying appropriate forces to the operator's hand in order to achieve the desired guidance. Two classes of virtual fixtures are considered; *Guidance virtual fixtures* (GVF) which guide the operator to follow a desired trajectory or surface, and *Forbidden-region virtual fixtures* (FRVF) which prevent the operator from exceeding a defined geometry workspace and entering a forbidden region [137].

Haptic virtual fixtures have been utilized in a diverse range of applications in the robotics domain. Studies suggest that the operator performance can increase by as much as 70% through virtual fixture guidance [138]. The works by [138-140] propose virtual fixtures for cooperative manipulators where the operator directly interacts with a robotic device to manipulate an environment. In [141-144], the operator controls a master robot, while receiving assistance by virtual fixtures, to command the slave robot to manipulate the environment.

In telemanipulation systems it is essential to provide the operator with an adequate level of transparency between the operator's control of the master device and the slave environment [145]. As such, a large body of work focuses on improving the fidelity between the operator (master side) and the environment (slave side) [146-147]. Haptic virtual fixtures impose haptic intervention to the operator's hand (master side) in order to guide their control according to some predefined criteria. This haptic intervention is virtually imposed upon the operator and may not directly

derive from the slave environment. In this context, virtual fixtures contrast the concept of full transparency.

In the case where the virtual fixture can be overpowered by the operator, this constitutes the ability of the teleoperator to have the *ultimate control* of the of the slave microrobotic manipulator. In this work, the haptic virtual fixtures are considered as assistance, where the operator is able to physically override the virtual fixtures. In practice this is achieved by limiting the maximum exertable haptic force to $< 3.3N$. In real terms this amounts to the bio-operator remaining in ultimate control of the microrobot while receiving assistance as to appropriate control behaviour. The addressing approach to haptic microrobotic cell injection lends itself to assisting the bio-operator in real-time intracellular injection or for offline virtual procedural training. Haptic virtual fixtures perform similar roles in either case, i.e. to guide/train the bio-operator in the cell injection process according to predefined criteria.

5.2 HAPTIC ASSISTANCE FOR CELL INJECTION

The micro cell injection process involves approaching a single immobilised cell with a micropipette, puncturing the chorion, penetrating the cytoplasm and then stopping at a designated location inside the cytoplasm for deposition.

The zebrafish is an important model organism for genetic studies and drug discovery. The zebrafish offers external fertilisation and development, a short development period, transparent embryos offering ease of observation of individual cells during development as well as having similar major organs to humans [148]. As such, the zebrafish embryo is the focus of this work to haptically guided cell injection. The zebrafish embryo

consists of the chorion, cytoplasm membrane and cytoplasm. Figure 5.1(a) depicts a zebrafish embryo.

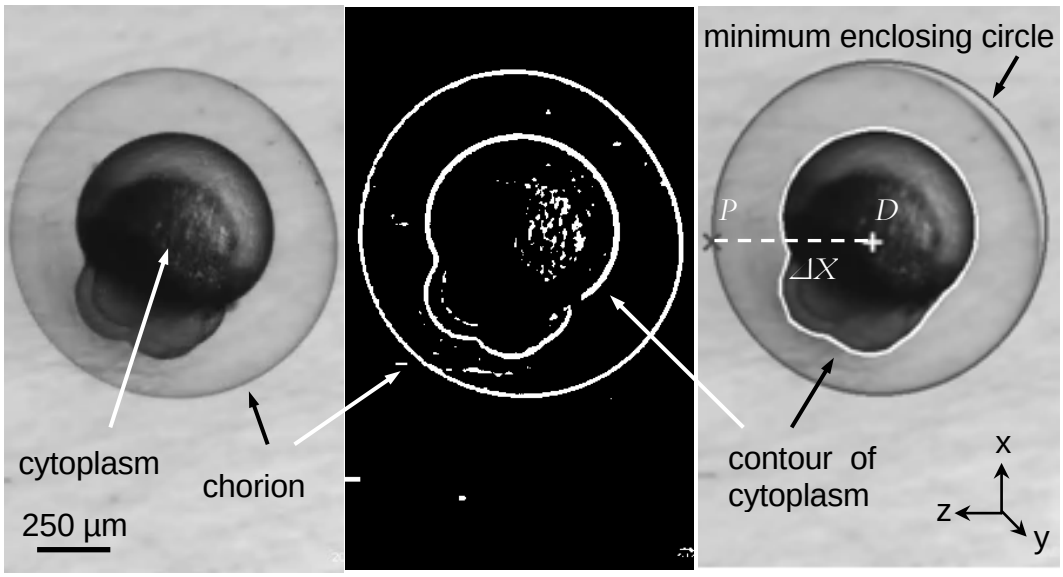

(a) (b) (c)

Figure 5.1 Image processing of zebrafish embryo structures to determine the penetration point and deposition target for the zebrafish embryo.(a) Zebrafish embryo. (b) Pre-processing. (c) Recognised membranes, deposition target D (cytoplasm center), penetration point P and depth of insertion ΔX. (c) Recognised deposition target D (cytoplasm center), penetration point P and depth of insertion ΔX.

The task can be defined by four objectives:

a) Guiding the operator to penetrate the cell at a desired penetration point.

b) Injecting along the longitudinal axis of the micropipette.

c) Stopping the micropipette's tip at a deposition target.

d) Depositing the material at the target point.

In this perspective, three haptic virtual fixtures are intoduced in order to guide the bio-operator to approach the cell, inject appropriately and to stop the micropipette after reaching the deposition point within the cytoplasm. The first is a planar virtual fixture attempting to prevent the bio-operator from exceeding the desired deposition point depth. The second is an axial virtual fixture provides the operator with the option to constrain the micropipette's trajectory to the direction of the longitudinal axis. The last is a novel haptic virtual fixture scheme based on potential force field analysis which guides the micropipette tip's motion within a volumetric symmetric shape, as well as recommending the desired path for optimal injection.

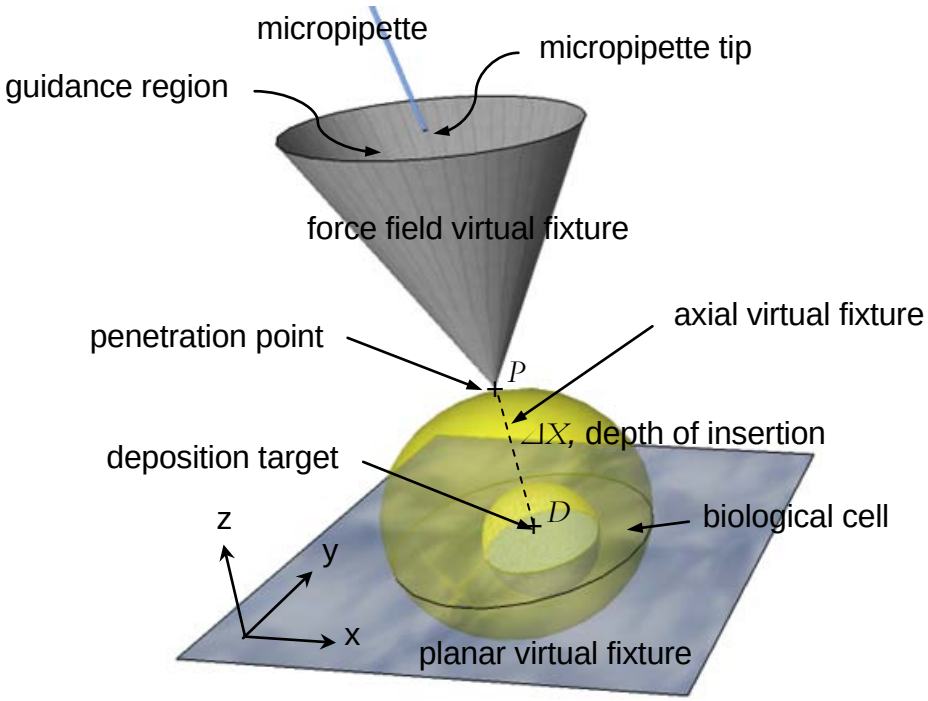

Figure 5.2 Introduced virtual fixtures for cell injection.

Figure 5.2 graphically depicts the virtual fixtures for guiding the bio-operator according to the defined objectives. *P* denotes the desired

location for the initial micropipette-chorion contact and insertion, D is the deposition target location and ΔX is the penetration depth given by $\Delta X = D - P$. The determination of these parameters (P and D) using vision [149] is demonstrated by Figure 5.1 (b) and Figure 5.1 (c). P would be a point on the minimum enclosing circle (Figure 5.1 (c)), where a vector joining P to D (the penetration depth), is parallel with the micropipette.

The operation of each of the virtual fixtures is as follows:

- **Planar virtual fixture** where the operator is prevented from penetrating the plane and exceeding the desired insertion depth. The virtual plane is orthogonal to the force field's axis of symmetry and the deposition target location lies within the plane.

- **Axial virtual fixture** which can be enabled by the operator using either of the buttons on the haptic device's stylus. When enabled (only available when the micropipette tip is within the cell - after paraboloid and cell indentation forces are no longer active) this virtual fixture attempts to restrict the user along the direction of the micropipette's longitudinal axis.

- **Volumetric virtual fixture** where a force field within the volumetric shape applies forces to the operator's hand so as to guide (suggest) the desired trajectory to point P. The penetration point P is located at the volumetric shape vertex. Aside from guiding the operator to point P, large repulsive forces near the volumetric shape surface attempt to prevent the operator from allowing the micropipette tip to penetrate the virtual surface. The micropipette tip is considered as the point of reference.

The operation of these virtual fixtures results in the operator being subject to one of the following modes:

- **No guidance mode** where the bio-operator is controlling the micromanipulator with no force being applied to his hand.

- **Guidance mode** where the micropipette's tip has entered the guidance region within the force field. *The guidance force guides/suggests the desired path to the bio-operator's hand*

- **Forbidden mode** where the micropipette's tip attempts to penetrate virtual fixture surfaces (force field or plane) or deviate from the axial virtual fixture. *Haptic forces attempt to prevent the bio-operator from allowing the micropipette tip to exceeding the virtual fixtures.*

The planar, axial and force field virtual fixtures are discussed in more detail in the following subsections.

5.2.1 PLANAR VIRTUAL FIXTURE

The planar virtual fixture attempts to prevent the operator from exceeding the desired insertion depth. The plane is orthogonal to the paraboloid's axis of symmetry and the deposition target location, D, lies within the plane. The plane can be defined by its normal vector (paraboloid axis of symmetry) and a reference point P, the penetration point. The vector $\overrightarrow{DP}$ with the initial point, D (deposition target location) terminating at P (penetration point) represents the normal vector of the planar virtual fixture where D lies in the plane. As such, the planar virtual fixture is given by

$$\overrightarrow{DP} \cdot (X - D) = 0 \tag{5.1}$$

where $\cdot$ denotes the dot product and X is the position vector of any point (x, y, z) lying in the plane.

Let's recall that the HIP is denoted by P_h and represents the point of haptic device-operator interaction. The haptic forces rendered to the bio-operator are realized at the HIP and its motion is mapped to the motion of the micropipette's tip. In order to haptically render the virtual fixture plane two considerations must be met, namely, *collision detection* and *force response and control* [45]. The *collision detection* component of the haptic rendering first requires the determination of the current position of the HIP, P_h and the virtual plane. If the position of the HIP has exceeded the virtual fixture defined by expression (5.1), then collision/penetration of the HIP with the virtual plane can be assumed. In this case, *force response and control* is necessary to render the appropriate forces to the operator at the HIP. The depth of penetration of the planar virtual fixture forms the basis for the haptic rendering. A spring model is used [45] and relates the distance of surface penetration to the haptic force according to Hooke's law.

5.2.2 AXIAL VIRTUAL FIXTURE

The axial virtual fixture provides the operator with the option to constrain the micropipette's trajectory to the direction of the longitudinal axis. The direction of the micropipette's longitudinal axis is given by column 1 of expression (3.3).

As the HIP exceeds the longitudinal axis, a displacement between P_d (desired position lying in the longitudinal axis) and P_h (HIP position)

exists, forming the basis for the haptic axial virtual fixture. Similar to expression (3.12), spring models are used to relate the desired position, P_d, with the current position, P_h, according to Hooke's law. The haptic axial virtual fixture force is given by

$$F = \begin{cases} 0 & P_h = P_d \\ K(P_h - P_d) & P_h - P_d \neq 0 \end{cases} \tag{5.2}$$

where K is specified appropriately.

Invoking this virtual fixture is suitable after penetrating the cell membrane and when no longer subject to the force field virtual fixture.

5.2.3 VOLUMETRIC VIRTUAL FIXTURE

This section discusses the volumetric virtual fixtures based on potential field models. The volumetric virtual fixture haptically guides the bio-operator's manipulation of the micropipette to approach the penetration point, *P*. This section investigates different geometries for the potential field-based virtual fixtures.

Potential fields have been widely used for robotic trajectory planning [150-151]. Potential fields generate a force field which can be used to guide robots towards target points while avoiding collision with obstacles or geometric constraints. Such approaches are equally suitable for haptically enabled systems where force fields can be used to guide the operator to target locations. A potential field can be considered as a scalar function, $u(x, y, z)$ and the gradient of this potential field provides a corresponding force field. In such a force field, the attraction forces can attract the robot

towards target points while the repulsive forces can prevent the robot from colliding with obstacles.

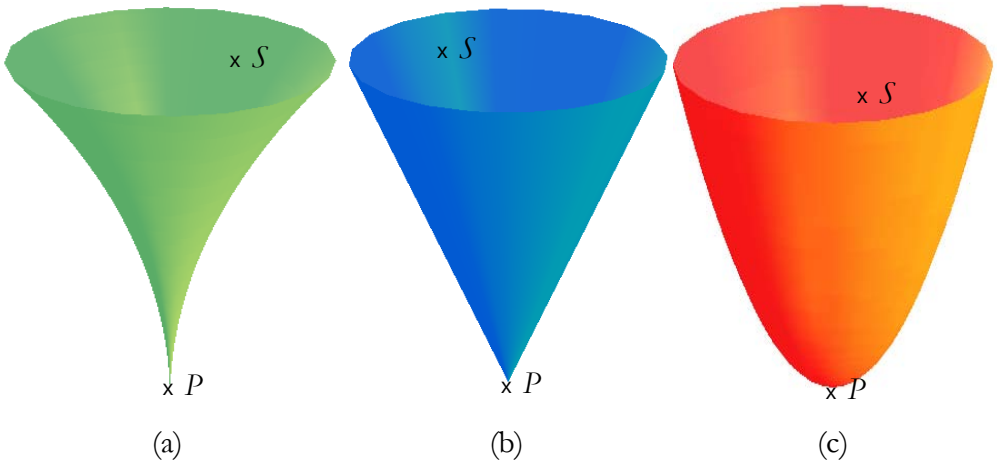

Figure 5.3 Symmetric volumes for volumetric haptic virtual fixtures. *S* denotes the start point and is located inside the volume, *P* denotes the penetration point at the vertex and (a) is the neiloid (n>2) (b) the cone (n=2) and (c) the paraboloid (0<n<2).

For cell injection, the force field within the virtual fixture guides the operator's manipulation of the micropipette tip to approach the penetration point, *P*. As indicated by Figure 5.2, a suitable geometry for this purpose would comprise a relatively large region for the micropipette tip to initially enter, then narrowing to a vertex point to guide to the penetration point on the cell surface. Three symmetric candidates for this purpose are the neiloid, cone and paraboloid as depicted by Figure 5.3. To form the volumetric virtual fixture, the surface is assumed to be a constant positive charge with a large negative charge point at the vertex.

The force field inside the volume is based on electrostatic model of potential fields. To form the virtual fixture, the surface of the shape is assumed as a constant negative charge with a positive charge point at the

vertex. The force field inside the shape can be represented by the Laplace equation of

$$\nabla^2 u(x,y,z) = \frac{-\rho(x,y,z)}{\varepsilon} \tag{5.3}$$

where $u(x,y,z)$ is a scalar potential function, ε is the permittivity within the shape and $\rho(x,y,z)$ is charge distribution function and $\rho(x,y,z)$ is defined by

$$\rho(x,y,z) = \begin{cases} -Q\delta(x)\delta(y)\delta(z) & \textit{virtual fixture vertex} \\ \rho_s & \textit{virtual fixture surface} \\ 0 & \textit{elsewhere} \end{cases} \tag{5.4}$$

where Q is the charge, $\delta(x)$, $\delta(y)$, $\delta(z)$ are Dirac functions and ρ_s is the planar charge density.

If the symmetric shape is considered as an integration of circles with centers along the z-axis, then the electric field of any point, r, anywhere in the xz-plane (Figure 5.4), can be derived as follows [152]

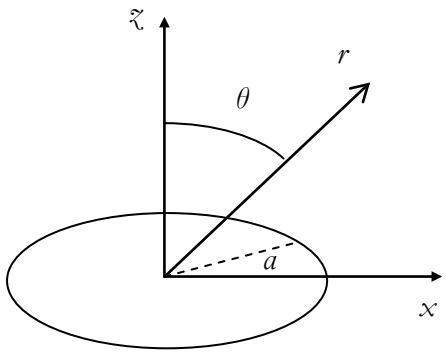

Figure 5.4 Schematic of the charged ring generating an electric field at *r*.

$$E_x = \frac{1}{4\pi\varepsilon_0}\frac{Q}{\pi a^2}\left\{\frac{\xi \sin\theta}{(1+\xi^2)^{\frac{3}{2}}} f_1(\mu) - \frac{1}{(1+\xi^2)^{\frac{3}{2}}} f_2(\mu)\right\} \tag{5.5}$$

$$E_z = \frac{1}{4\pi\varepsilon_0}\frac{Q}{\pi a^2}\left\{\frac{\xi \cos\theta}{(1+\xi^2)^{\frac{3}{2}}} f_1(\mu)\right\} \tag{5.6}$$

where E_x and E_z are electric fields along x and z axis respectively, a is the ring radius and

$$\xi = \frac{r}{a} \tag{5.7}$$

$$\mu = \frac{2\xi}{1+\xi^2} sin\theta \tag{5.8}$$

$$f_1(\mu) = \int_0^{\pi} \frac{d\alpha}{(1-\mu\cos(\alpha))^{3/2}} \tag{5.9}$$

$$f_2(\mu) = \int_0^{\pi} \frac{\cos\alpha\, d\alpha}{(1-\mu\cos(\alpha))^{3/2}} \tag{5.10}$$

The field is symmetric across α direction. Thus, while moving across α, the electric filed can be calculated as

$$\begin{aligned} E_{xc} &= E_x \cos(\alpha) \\ E_{yc} &= E_x \sin(\alpha) \\ E_{zc} &= E_z \end{aligned} \tag{5.11}$$

The drawback with this model is the computational complexity in real-time.

In order to make it computationally efficient in run-time, a good estimation of the proposed model can be obtained using a multi-charged particle system model. Let's consider the symmetric surface of the shape with uniform distribution of n circles with k charge points where each point represents a static negative charge on a circle and a large positive static charge point at the vertex. The potential field can then be obtained discreetly by

$$u(x,y,z)=\sum_{n}\sum_{k_n}\frac{1}{4\pi\varepsilon}\frac{Q_{k_n}}{\sqrt{(x-x_{k_n})^2+(y-y_{k_n})^2+(z-z_{k_n})^2}} + \frac{1}{4\pi\varepsilon}\frac{-Q_0}{\sqrt{x^2+y^2+z^2}} \tag{5.12}$$

where Q_0 is the large negative charge at the shapes 's vertex, Q_{k_n} is the positive charge located at $(x_{k_n}, y_{k_n}, z_{k_n})$ on the n^{th} circle as illustrated by Figure 5.5.

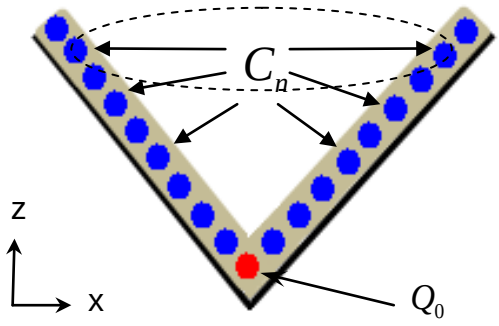

Figure 5.5 Multi-charged particle system model for a cone shape. Q_0 denotes the large negative charge at the cone apex (vertex) and C_n denotes the n^{th} circle on the cone surface where discrete positive charge Q_{k_n} denotes distributed on it uniformly.

To prevent infinite potential at target point (vertex), a constant l with appropriate value should be added to the dominator of the second term. Thus, expression (5.12) would be rewritten as:

$$u(x,y,z)=\sum_{n}\sum_{k_n}\frac{1}{4\pi\varepsilon}\frac{Q_{k_n}}{\sqrt{(x-x_{k_n})^2+(y-y_{k_n})^2+(z-z_{k_n})^2}} + \frac{1}{4\pi\varepsilon}\frac{-Q_0}{\sqrt{x^2+y^2+z^2}+l} \tag{5.13}$$

The force field is then given by the gradient of $u(x,y,z)$ from expression (5.13).

Given the symmetric property of the virtual fixture, the real-time computational efficiency of the multi-charged particle structure can be improved further. The symmetric virtual fixture (vertex at the origin) can be represented by the expression

$$z^n=\frac{x^2}{a^2}+\frac{y^2}{b^2} \tag{5.14}$$

where a and b are constants specifying the level of curvature in the x-z and y-z planes respectively. Depending on the value of n, the resulting geometry of the virtual fixture (VF) is (Figure 5.3):

$$VF=\begin{cases} paraboloid & ,0<n<2 \\ cone & ,n=2 \\ neiloid & ,n>2 \end{cases} \tag{5.15}$$

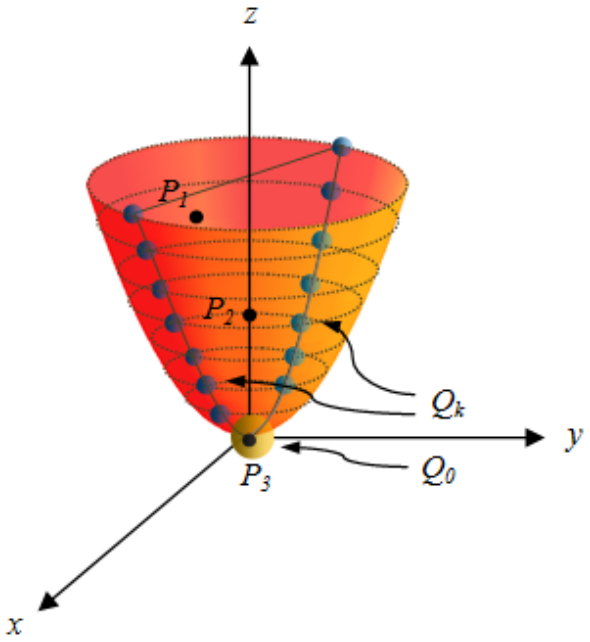

Figure 5.6 Schematic of multi-charged particle system model of the parabola. P_1, P_2 and P_3 denote HIP, any point on the z-axis and the paraboloid's vertex at (0,0,0) respectively. Q_0 is the large negative charge at the paraboloid's vertex, Q_k is the positive charge located at (x_k, y_k, z_k).

Figure 5.6 depicts a paraboloid with its vertex and focus located at the origin and on the z-axis respectively. Then, at any time, given a HIP, P_1, (off the z-axis), and any point on the z-axis P_2, and the vertex P_3, then only one plane can include all three points. The plane can be represented as

$$Ax + By + Cz + D = 0 \tag{5.16}$$

where the plane's normal is the vector (A, B, C). Given three points $P_1 = (x_{HIP}, y_{HIP}, z_{HIP})$, $P_2 = (0,0,z_0)$ and $P_3 = (0,0,0)$, plane parameters would be derived as $A = y_{HIP}z_0, B = -x_{HIP}z_0$, $C = 0$, $D = 0$. Therefore, such a plane can be described by

$$x = k_1 y \tag{5.17}$$

where

$$k_1 = \frac{x_{HIP}}{y_{HIP}} \tag{5.18}$$

In cases where the HIP, P_1, is on the z-axis, any plane including the z-axis can be considered. The cross section between this plane and the symmetric virtual fixture in 3D space is given by

$$z^n = k_2 x^2 = k_3 y^2 \tag{5.19}$$

where

$$k_2 = \frac{1}{a^2} + \frac{1}{(k_1 b)^2} \tag{5.20}$$

$$k_3 = k_1^2 k_2 \tag{5.21}$$

The cross sections (CS) shown in Figure 5.7, given by expression (5.19), differ according to the value of n, and is

$$CS = \begin{cases} parabola & ,0 < n < 2 \\ Vshape & ,n = 2 \\ semicubical\ parabola & ,n > 2 \end{cases} \tag{5.22}$$

(a) (b) (c)

Figure 5.7 The cross section between the plane and the virtual fixture in forms of (a) semicubical parabola, (b) two lines making a V shape, and (c) parabola where the uniform distribution of k charge points would lay on them.

A uniform distribution of k charge points on the cross section (parabola, lines or semicubical parabola) of the virtual fixture forms the optimized multi-charged particle model. Figure 5.6 depicts the paraboloid case. Each point represents a static positive charge with a large negative static charge point at the vertex. The potential field can then be obtained by

$$u(x,y,z) = \sum_k \frac{1}{4\pi\varepsilon} \frac{Q_k}{\sqrt{(x-x_k)^2+(y-y_k)^2+(z-z_k)^2}} + \frac{1}{4\pi\varepsilon} \frac{-Q_0}{\sqrt{x^2+y^2+z^2}+l} \tag{5.23}$$

where Q_0 is the large negative charge at the virtual fixture's vertex and Q_k is the positive charge located at (x_k, y_k, z_k).

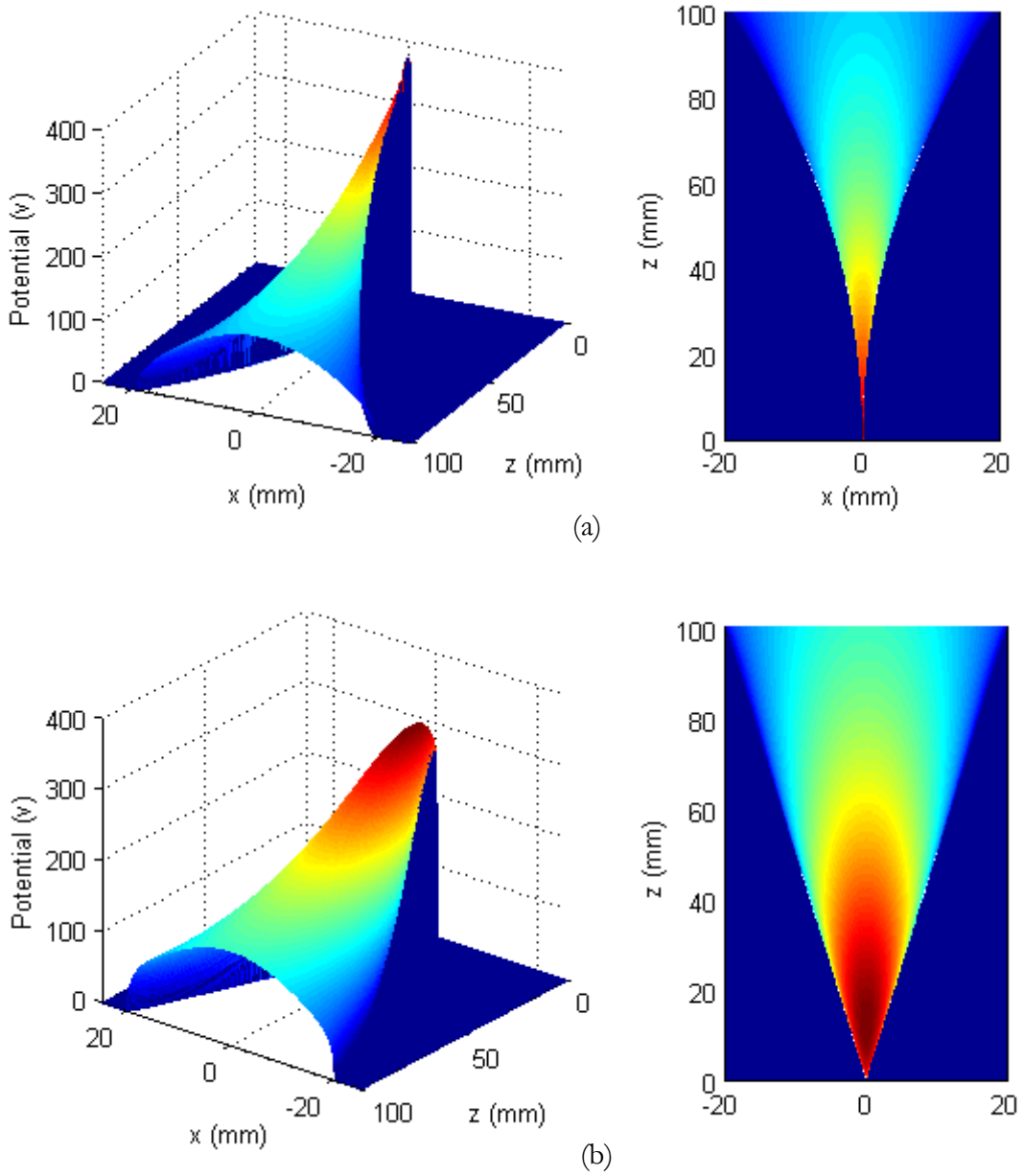

Figure 5.8 3D and x-z plane projection view of the potential fields and force vectors. (a) potential field inside the neiloid (b) potential field inside the cone.

The force field is given by the gradient of $u(x, y, z)$. Comparing expressions (5.13) and (5.23), is apparent that the latter is less computationally expensive while maintaining the same functionality.

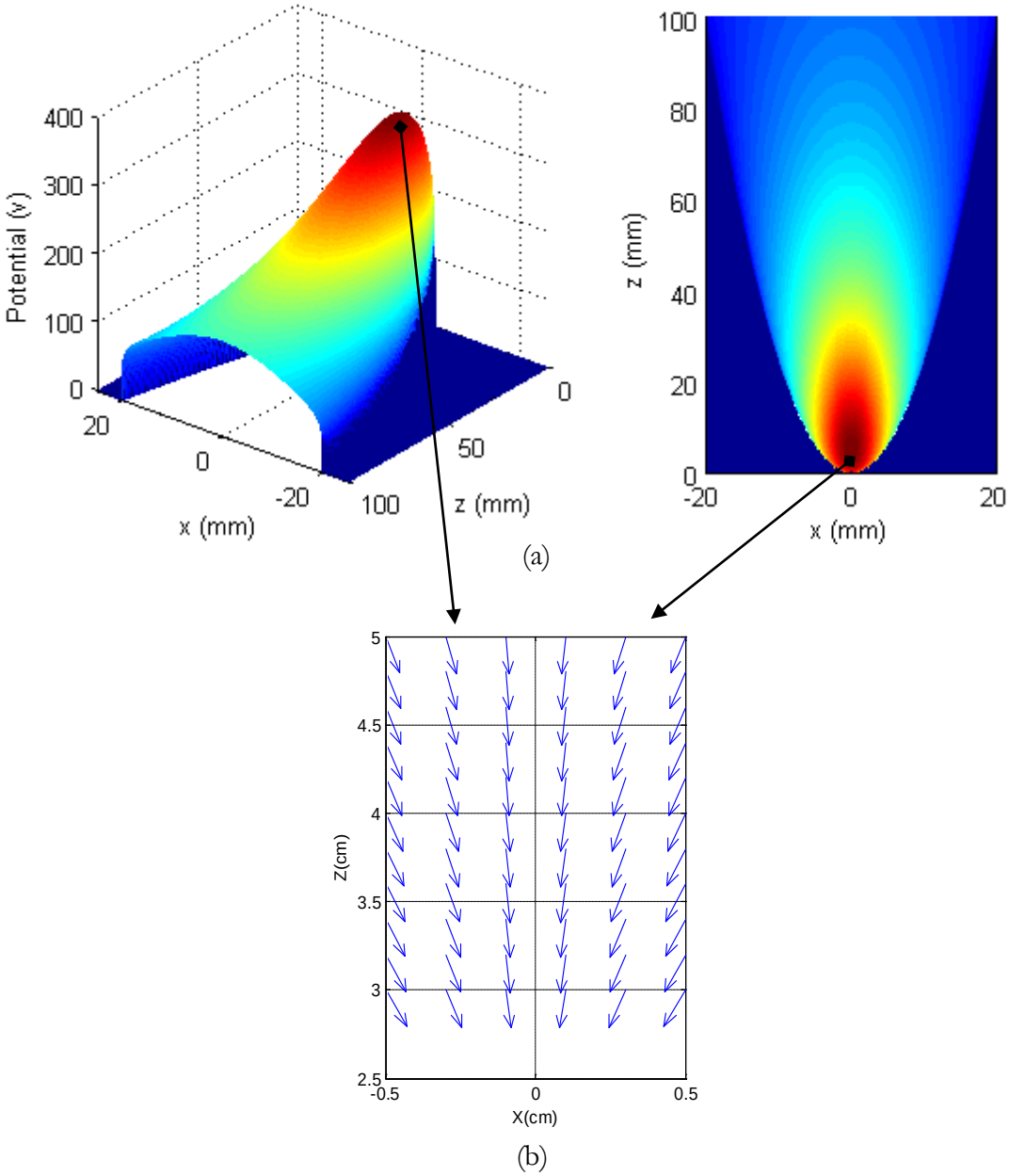

Figure 5.9 3D and x-z plane projection view of the potential fields of parabaloid and force vectors. (a) potential field inside the paraboloid (b) a selected region of the paraboloid potential field demonstrating corresponding force vectors projected in x-z plane.

Figure 5.8 and Figure 5.9 demonstrate the potential fields generated by the multi-charged particle models for the neiloid, cone and paraboloid. As can be observed, when approaching the target location at the virtual

fixture's vertex the potential increases. The gradient of this potential provides the haptic guidance force applied to the bio-operator's hand.

It is worth acknowledging the steep gradient of the potential field profile close to the virtual fixture surface. The purpose of this steep gradient is to attempt to prevent the operator from moving the micropipette's tip past the virtual fixture's surface. However, excessively sharp haptic forces may cause instability and oscillation to the user's hand and should be avoided.

As indicated by Figure 5.8 (a) the neiloid virtual fixture has the steepest gradient near its surface while the paraboloid (Figure 5.9 (a)) is the smoothest. Figure 5.9 (b) provides a zoom view of a selected region of the paraboloid virtual fixture's potential field and the corresponding force field vectors. As can be deduced, all force vectors (corresponding to haptic guidance) are directed towards the paraboloid's vertex (penetration point). Force vectors in close proximity to one another have relatively similar lengths corresponding to a smooth and continuous guidance force.

5.2.4 SYSTEM EVALUATION

While three introdueced volumetric potential field virtual fixtures all meet the requirement of converging to a vertex, the degree of smoothness of the generated force field should also be considered. Abrupt changes in force levels within the force field will correspond to sharp haptic forces applied to the user's hand. This in turn may cause instability and oscillation and affect the operator's performance of the cell injection task. In the aim of designing virtual fixtures which avoid such behaviour, this section evaluates performance of three volumetric virtual fixturs for haptically

assisting the bio-operator in penetrating the biological cell at the desired location.

As the basis to evaluate and compare the three virtual fixtures, an emulation environment was developed to mimic real human user inputs and monitor the corresponding guidance provided by the virtual fixtures. This provides a useful tool for generating a large number of trials in order to compare the operation of each of the virtual fixtures. The emulation considers the motion behavior and tremor [153] of different hands and different hand motion trajectories mimic holding and moving the HIP through the volumetric force field.

For comparison purposes, each trial begins from the same start position (start point S in Figure 5.3) and the objective is to reach the penetration point P. Failure to reach the penetration point P constitutes a failed task. The distance between S and P is consistently 700 μm in all trials. In order to adequately consider combinations of K_S (i.e. 20, 40, 60, 100, 125 and 150) and either the neiloid, cone, paraboloid or no virtual fixture, 528 trials were completed. The result is 22 sets of results for each combination. K_S is the workspace scaling factor between the haptic device and the micromanipulator which introduced in Chapter 3. Table 5.1 summarizes number of successful trials. Table 5.2 reports the mean time for completion of successful trials. Table 5.3 shows failure rate of trials scaled between 0 to 1.

K_s	No fixture	Neiloid	Cone	Paraboloid
	number of successful trials			
20	12	9	17	20
40	13	11	18	22
60	14	13	17	20
100	15	12	19	21
125	15	14	20	21
150	16	15	21	22

Table 5.1 Number of successful trials for different combinations of K_s and virtual fixtures. 22 trials were completed for each K_s and virtual fixture combination.

K_s	No fixture	Neiloid	Cone	Paraboloid
	mean completion time (sec.)			
20	1.04	0.72	0.86	0.91
40	2.1	1.45	1.69	1.83
60	2.96	2.1	2.49	2.66
100	5.18	3.54	4.25	4.51
125	6.6	4.54	5.29	5.42
150	7.75	5.2	6.16	6.7

Table 5.2 Mean completion time for successful trials of different combinations of K_s and virtual fixtures.

K_s	No fixture	Neiloid	Cone	Paraboloid
	failure rate			
20	0.45	0.59	0.23	0.09
40	0.41	0.50	0.18	0.00
60	0.36	0.41	0.23	0.09
100	0.32	0.45	0.14	0.05
125	0.32	0.36	0.09	0.05
150	0.27	0.32	0.05	0.00

Table 5.3 Failure rate for different combinations of K_s and virtual fixtures.

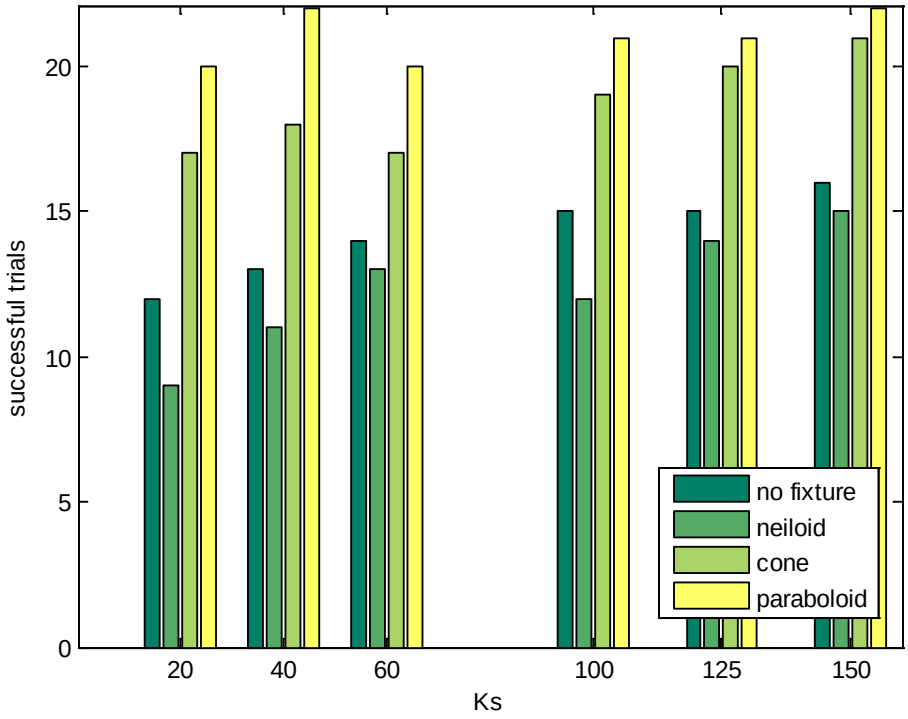

Figure 5.10 Number of successful trials for different combinations of K_s and virtual fixtures. 22 trials were completed for each K_s and virtual fixture combination.

Figure 5.10 shows the number of successful trials for different K_S and virtual fixture combinations. The results indicate that the cone and paraboloid virtual fixtures can increase the success rate in reaching the penetration point P. The neiloid virtual fixture however, may prove worse than having no virtual fixture guidance at all. Figure 5.11 considers the observed failure rates in more detail. The results demonstrate that the cone and paraboloid virtual fixtures have very low rates of failure, indicative of the ability to guide the user to the deposition location. The paraboloid virtual fixture clearly indicates the lowest incidence of failure. The neiloid virtual fixture has the highest incidence of failure for all values of K_S , even more so than having no virtual fixture. Through our observations we

suggest that this is caused by the geometry of the neiloid virtual fixture. When approaching the neiloid's vertex, it is unavoidable that the HIP is close to the surface of the virtual fixture and subject to the high gradient of the potential field. Under this condition, any hand tremor or deviation from the optimum trajectory results in a very large force applied to the bio-operator's hand. As mentioned earlier, this likely leads to instability and oscillation.

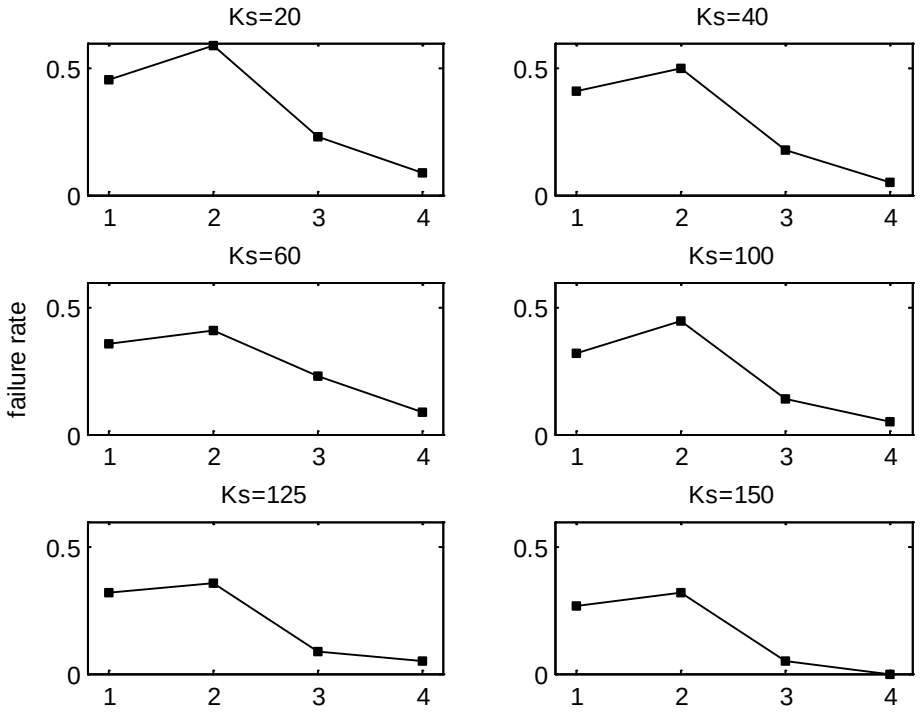

Figure 5.11 Failure rate for different combinations of K_s and virtual fixtures. No. 1-4 on the horizontal axis represent no fixture, neiloid, cone and paraboloid respectively.

Such a situation is much less likely for the cone and paraboloid virtual fixtures because they are far less narrow when approaching the vertex. It is suggested that the same phenomena contributes to the higher success rate of the paraboloid in comparison to the cone virtual fixture. Considering

the three volumetric potential fields, the paraboloid provides the smoothest gradient transitions (as demonstrated by Figure 5.9). This corresponds to the smoothest guidance force applied to the bio-operator.

Figure 5.12 shows the mean completion time for successful trials of different combinations of K_S values and virtual fixtures. As can be expected the results demonstrate that an increasing K_S corresponds to increasing mean completion time for all four virtual fixture configurations (three volumetric as well as no virtual fixture). This occurs because as K_S increases so does the length of the necessary user input trajectory in order to complete the task (reach penetration point P).

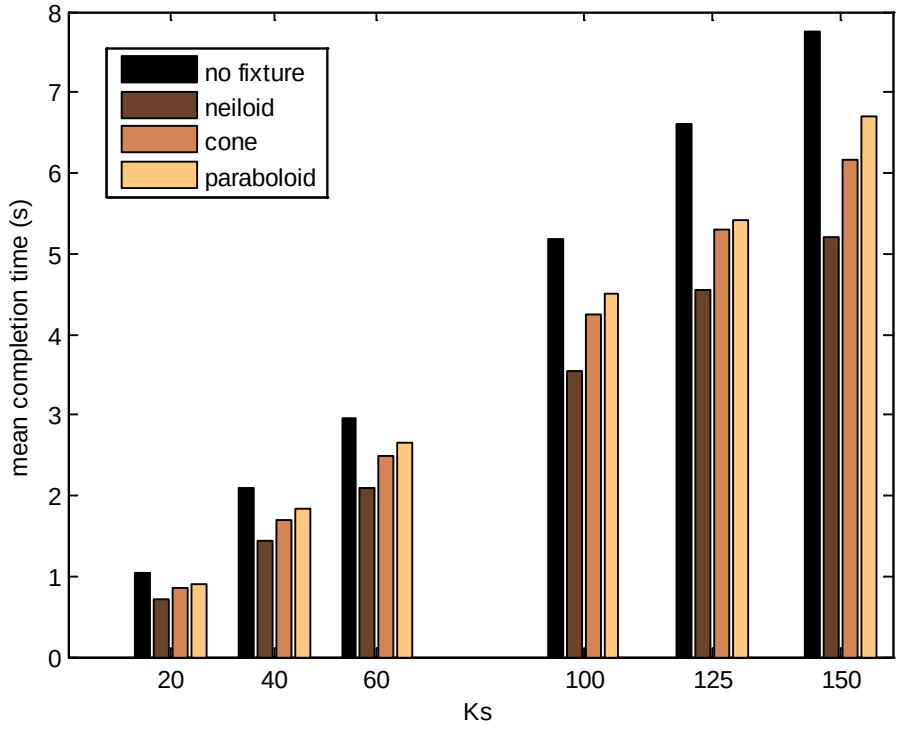

Figure 5.12 Mean completion time for successful trials of different combinations of K_s and virtual fixtures.

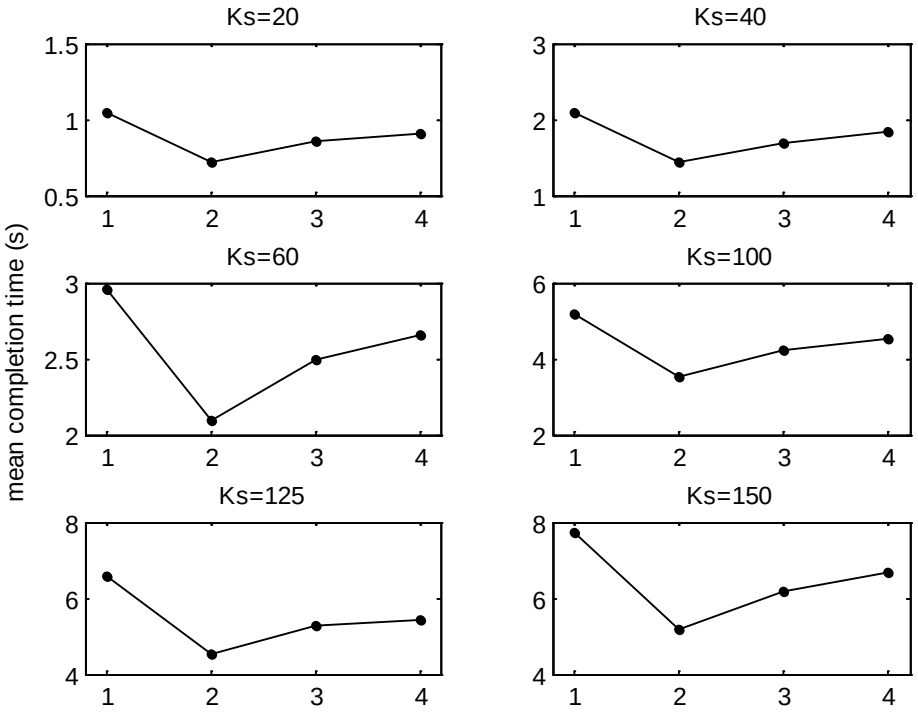

Figure 5.13 Mean completion time for trials of different combinations of K_s and virtual fixtures. No. 1-4 on the horizontal axis represent no fixture, neiloid, cone and paraboloid respectively.

Figure 5.13 shows the mean completion time in more detail. No. 1 (no virtual fixture) represents the benchmark, and the results indicate that the use of any of the three virtual fixtures can reduce the completion time. The neiloid virtual fixture has the lowest mean completion time and it is suggested that this can be attributed to the large forces encountered when approaching the vertex.

These large forces are applied to the bio-operator's hand and encourage faster completion of the trajectory. Recall however that achieving the fastest completion time is coupled with the highest failure

rate of the three virtual fixtures. The cone virtual fixture has a slightly faster completion time than the paraboloid, however achieves a lower success rate.

These findings suggest that in the context of the proposed haptic cell injection task, this success rate is of more importance than completion time. As such the paraboloid would be the best choice of the three force field virtual fixtures.

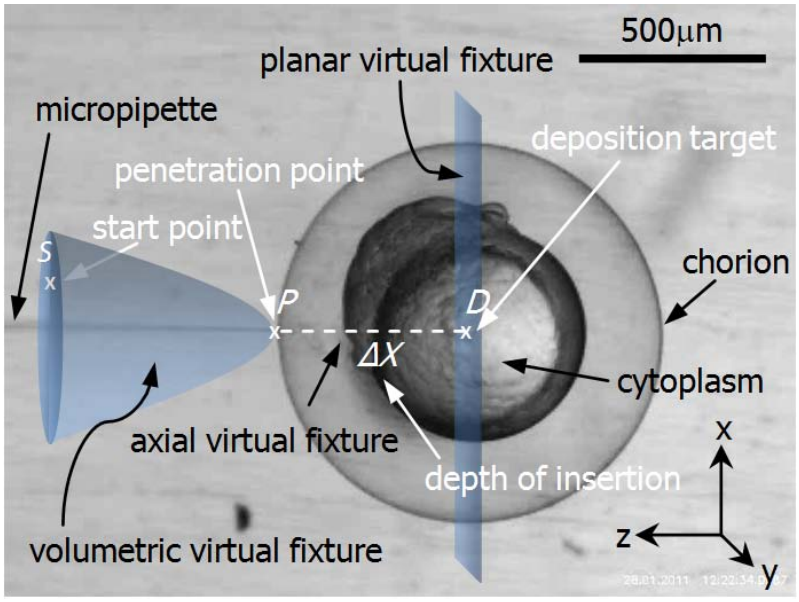

Figure 5.14 A snapshot of microrobotic zebrafish embryo injection while haptic virtual fixtures are in operation for guidance.

Figure 5.14 demonstrates the zebrafish embryo injection process where the penetration point, *P* and the deposition target, *D* are determined by the image processing (Figure 5.1) and paraboloid force field, axial and planar virtual fixtures are set to guide the bio-operator while performing the injection. For this operation, the scaling factor, K_s is set to 40.

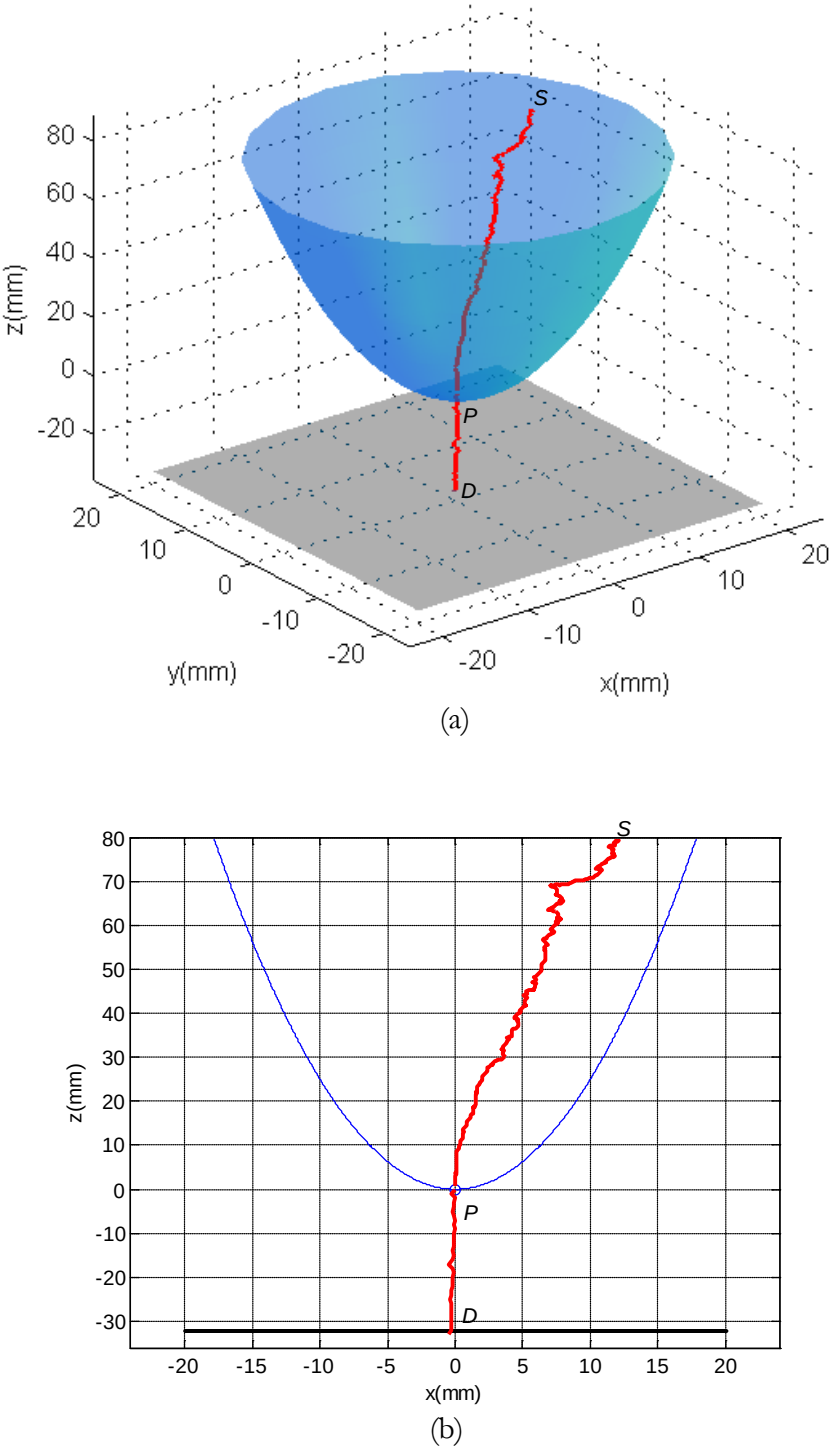

Figure 5.15 Real-time trajectory of the Haptic Interaction Point. (a) 3D view of the trajectory, (b) trajectory projected in the xz-plane. *S*, *P* and *D* denote the start point, penetration point and deposition target respectively.

Figure 5.15 demonstrates the real-time ability of the proposed virtual fixtures to guide the bio-operator's control of the micropipette tip to the penetration point, *P* and stop at the deposition target, *D*. Figure 5.15 (a) and (b) show the operator's control of the HIP within the force field and along the axial haptic virtual fixtures in 3D and projected in the xz- plane respectively. It indicates how smoothly the operator is guided to the penetration point and stops at the deposition target by haptic force guidance. Figure 5.16 illustrates the corresponding guidance force applied to the bio-operator's hand along the trajectory.

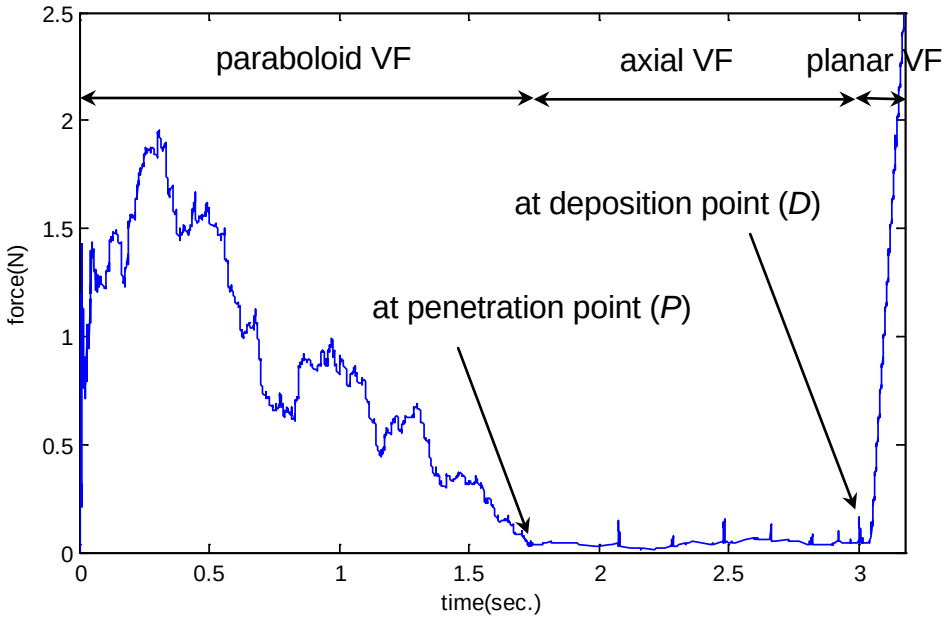

Figure 5.16 Force magnitude along the trajectory.

5.3 SUMMARY

This Chapter introduced a guidance system for haptically assisting the bio-operator to perform intracellular injection. In order to guide the bio-operator to reach the desired penetration point, to penetrate along the

appropriate axis, and to stop at a desired deposition target, three haptic virtual fixtures were addressed each aiming to assist the bio-operator with a particular aspect of the cell injection task. Three novel volumetric potential field virtual fixtures based on a multi-charged particle system model were introduced for haptically assisting the operator in penetrating the biological cell at the desired location. The neiloid, cone and paraboloid virtual fixtures were investigated as the force field virtual fixtures and evaluation results compared the functionality of the different volumetric virtual fixtures. After the bio-operator has penetrated the cell, an axial virtual fixture assists motion in the micropipette's longitudinal axis. A virtual fixture plane attempts to restrict the bio-operator from injecting beyond the deposition target. Results demonstrated the operation of the haptically assisted microrobotic cell injection system.

"There is no pleasure without a tincture of bitterness."

Hafez
1315-1390, Persian poet

Chapter 6

MICROPILLAR-BASED ON-CHIP SYSTEM FOR DYNAMIC FORCE MEASUREMENT OF *C. ELEGANS*

This Chapter and Chapter 7 are concerned with the second major contribution of this thesis. This Chapter introduces a micropillar-based on-chip system capable of quantifying the multi-point locomotive forces of moving *C. elegans*. The system consists of a PDMS (Polydimethylsiloxane) micropillar-based structure and an image processing algorithm for tracking pillars with sub-pixel resolution. Based on the deflection of micropillars when contacting the moving *C.elegans,* the interaction forces can be inferred. The system and presented experimental techniques form a powerful system for high resolution measurement of moving *C. elegans*.

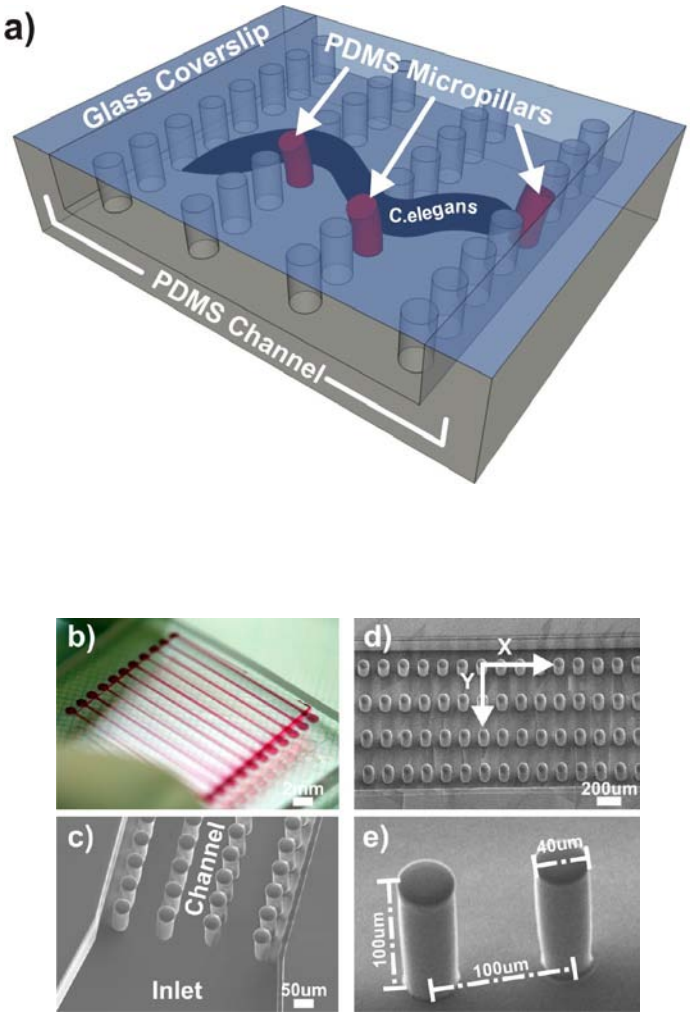

Figure 6.1 PDMS micropillar-based device for *C. elegans* force measurement. (a) The schematic of a worm deflecting micropillars while moving between them in a channel. (b) Photograph of the device with multiple channels having an inlet and outlet on both ends. The channels are filled with dye-coloured water for illustration. (c) Zoom-in view of one end of the channel with pillars and inlet. (d-e) SEM micrographs of the pillars with dimensions labeled.

6.1 MICROPILLAR-BASED PDMS DEVICE

Figure 6.1(a) graphically depicts the micropillar-based PDMS device's principle of operation. The device consists of a channel containing parallel rows of micropillars (fabricated in PDMS) and enclosed by a glass

coverslip. To measure the forces exerted during *C.elegan* motion, *C.elegans* are loaded into the water-filled channel. When the *C.elegans* move contact with pillars causes bending, which is sensed by a camera attached to a microscope.

6.1.1 DEVICE DESIGN

The device consists of a number of straight and parallel channels (those filled with dye-colored water in Figure 6.1(b)). Each channel, containing several parallel rows of rising cantilever-like micropillars supported by the channel base, functions as an independent force measuring unit dedicated for one individual *C. elegans*. By doing so, cross-contamination of worms which otherwise share a same channel is eliminated. In the mean time, to increase fabrication throughput, multiple channels are designed in one chip to allow more worms to be assayed. More importantly, due to the same fabrication procedure, negligible variances in micropillars (size and mechanical properties) make force measurements highly consistent and comparable across channels or worms.

A glass coverslip is put on top of the PDMS device to protect the micropillars, worms, and channels from potential physical contamination, interference or damage. To facilitate loading of solutions, water, or the worm into the enclosed micropillar-filled channel, an inlet (Figure 6.1(c)) and outlet are extended from both ends of each channel, which are simply an open and clear concaved planar area. To prevent the micropillars from sticking to the glass coverslip, the depth of the channel is set to 20 μm greater than the height of micropillars, leaving a vertical gap between the top of the pillar and the coverslip.

Currently, the number of rows per each channel is four but more rows of micropillars can be easily added to the device as necessary. According to the width of an adult *C. elegans*, the height of micropillars is 100 μm, to ensure the worm moves inside the arrays of pillars rather than on their top (Figure 6.1(e)). The diameter of pillars can affect the force measurement resolution and currently is set to be 40 μm. The inter-pillar distances in the *x*- and *y*- directions are 100 μm and 150 μm, respectively.

6.1.2 FABRICATION

Standard soft-lithography technology was used for device fabrication, as shown in Figure 6.2. First, a master mold was formed in SU-8 negative photoresist (MicroChem) on a 4" silicon wafer as substrate. As the height of the pillars is not equal to the depth of the channels, a two-layer photoresist mold was made. An initial layer of SU-8 2025 was spin-coated to a thickness of 20 μm, softbaked according to the resist datasheet and exposed in a Suess MA6 mask aligner using a high-resolution chrome mask to form the channel outline. After postbake, a second, 100 μm thick layer of SU-8 2100 was coated on top of the first layer. The wafer was softbaked again and exposed through a second mask containing both the channel outline and pillar array. Following postbake of the second layer, the resist pattern was developed in (1-methoxy-2-propyl) acetate in an ultra-sonic bath, rinsed with IPA and hardbaked for 20 min at 150°C.

For replica-molding, PDMS pre-polymer was prepared by mixing Sylgard 184 (Dow Corning) base:curing agent in a 10:1 w/w ratio. The pre-polymer was thoroughly mixed and degassed to remove any air bubbles. The surface of the SU-8 mold was treated by exposure to

trimethylchlorosilane (TMCS, Sigma Aldrich) vapor for 2 hours to facilitate de-molding.

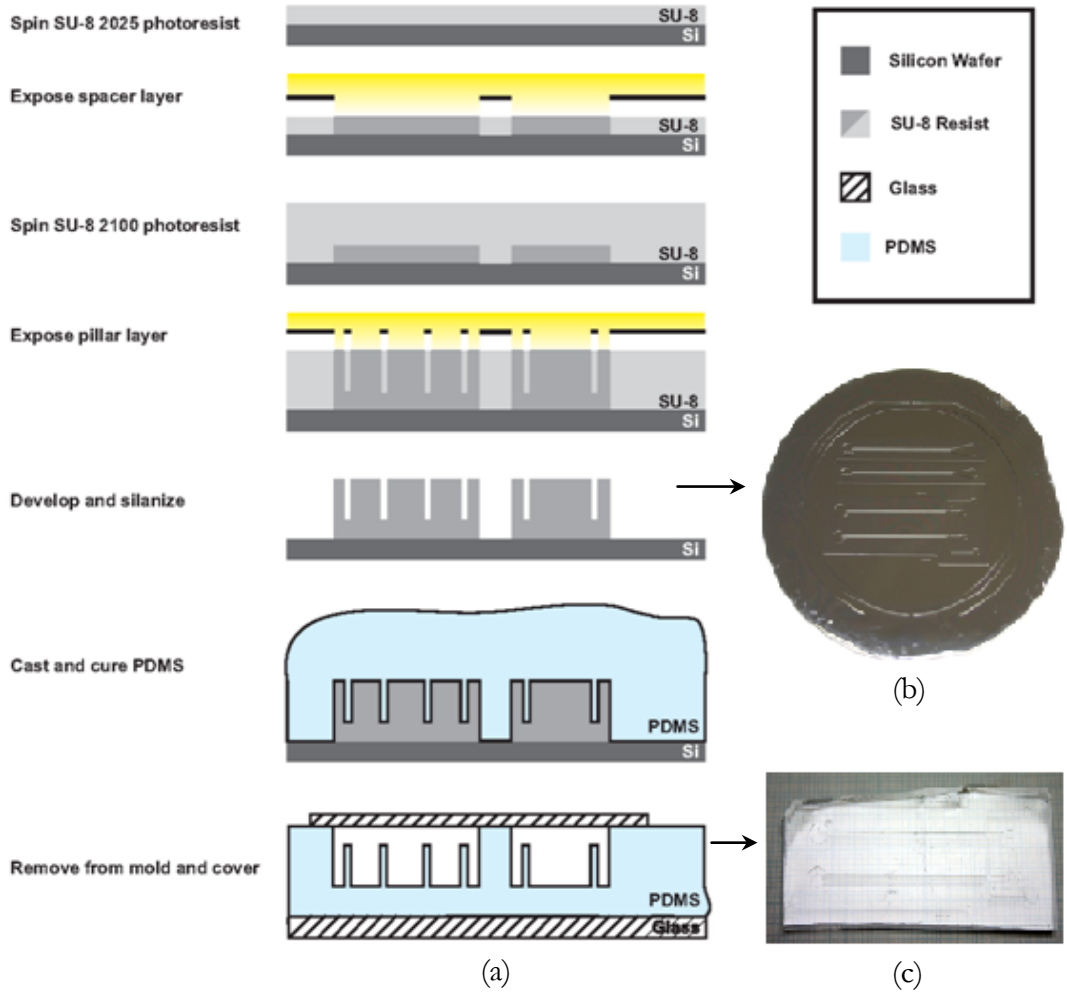

Figure 6.2 Main fabrication steps of Micropillar-based PDMS device. (a) Schematic of the device fabrication process. (b) Photograph of SU-8 mold. (c) Photograph of fabricated PDMS device.

Following this step, the polymer was poured onto the mold and degassed again to allow for bubble-free filling of the pillar holes. The mold was then placed on a hotplate and cured for 1 h at 80°C. After cooling to room temperature, the replica was carefully peeled off and cured for a further 4 hrs at 200°C. Individual devices were cut out using a scalpel and

placed on microscope slides for handling. Figure 6.3 shows two fabricated micro-pillar-based PDMS device prototypes with different intake layout.

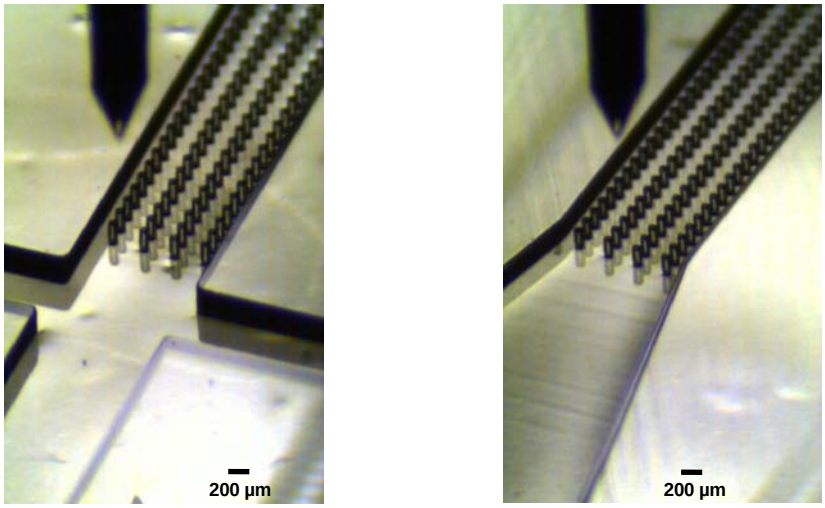

Figure 6.3 Photograph of two fabricated micro-pillar-based PDMS device prototypes with different intake layout.

6.2 FORCE SENSING PRINCIPLE

Figure 6.4 shows the deflection of a pillar undergoing force which is originating from the contact of the worm body with the pillar. Note that drag forces applied to the pillar by the fluidic environment were safely ignored, which were determined to be at a force level of 10^{-13} N using the fluidic drag model [154]. Through an imaging system (a camera mounted on a microscope), the deflection Δ of the free end of the pillars was recorded and measured via a custom image processing algorithm. With the deflection available, the force f was subsequently obtained by a linear spring force-deflection model

$$f = k\Delta \tag{6.1}$$

where k is the stiffness of the pillar, and described in the subsequent section.

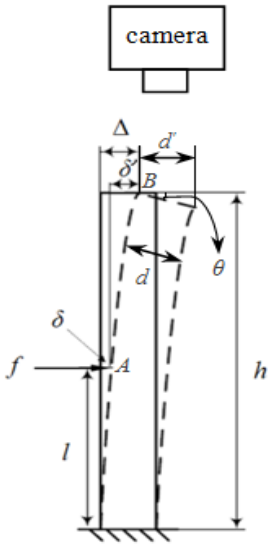

Figure 6.4 Schematic of the bending pillar for force analysis. h is length of the pillar, f the force, l the height where force is imposed, δ deflection at force point and Δ deflection at top end of the pillar.

6.2.1 FORCE-DEFLECTION MECHANICS MODEL

As the worm moves inside the array of pillars, the force does not apply at the free end of the pillar. Due to this the total deflection of the free end is attributed to two parts: (i) the deflection δ proportional to the load force at the force loading point A, and (ii) the linear displacement δ' of the free end B geometrically transmitted from point A.

A valid application of linear elasticity requires small pillar deflections, which can be evaluated by the slope of the posts' free ends, θ (Figure 6.3)

$$\theta = \cos^{-1}(d'/d) \tag{6.2}$$

where d is the pillar diameter, and d' is the projection of the deflected pillar, which was measured from image sequences. The maximum value of θ was found to be 17°, which satisfies $\sin\theta \approx \theta$ and thus, the small-deflection assumption of linear elasticity holds [155]. The small vertical force component and hydrostatic pressure exerted by the fluidic environment are at least three orders of magnitude lower than sufficient for buckling a rising pillar.

Deflection of a cantilever beam is attributed to both bending and shear incurred by the force load. When the aspect ratio (i.e., height to diameter ratio) of a cantilever beam is greater than 5, deflection due to the shear can be safely ignored as it contributes less than 5% to the total deflection. However, as the aspect ratio of the micro fabricated pillar is 2.5 (i.e., 100:40), both bending and shear must be considered in the force-deflection mechanics model given by

$$\delta = \left(\frac{l^3}{3EI} + \frac{d^2(1+\gamma)l}{4EI} \right) . f \tag{6.3}$$

where f is the force, l is the length from the load to the support, I is the moment of inertia, and E and γ are Young's modulus and Poisson's ratio for PDMS, respectively. The first term and second term in expression (6.3) represent pure bending and shear respectively. Pillar diameters are considered uniform along the height, which was verified by high-magnification SEM imaging (see Figure 6.1(e)), thus I can be given by

$$I = \frac{\pi d^4}{64} \tag{6.4}$$

Beyond the load, the displacement is linear because no other force exists. Therefore, this displacement can be derived based only on bending

$$\delta' = \frac{l^2}{2EI}(h-l).f \tag{6.5}$$

where h is the pillar height.

The total free-end deflection of the pillar is a superposition of the two components in expressions (6.3) and (6.5):

$$\Delta = \delta + \delta' = f\left\{\left(\frac{l^3}{3EI} + \frac{d^2(1+\gamma)l}{4EI}\right) + \frac{l^2}{2EI}(h-l)\right\} \tag{6.6}$$

rearranging terms results in

$$f = \frac{\Delta}{\left(\frac{l^3}{3EI} + \frac{d^2(1+\gamma)l}{4EI}\right) + \frac{l^2}{2EI}(h-l)} \tag{6.7}$$

substituting f from expression (6.1) into expression (6.7) yields k, the stiffness of the pillar:

$$k = \left\{\left(\frac{l^3}{3EI} + \frac{d^2(1+\gamma)l}{4EI}\right) + \frac{l^2}{2EI}(h-l)\right\}^{-1} \tag{6.8}$$

To quantify k, the only unknown parameter is the Young's modulus (E) of the PDMS, which should be calibrated and this is described in the next section.

Note that expression (6.1) implies that the direction of load follows that of the deflection, permitting the dynamic force of a moving worm to be resolved with both magnitude and direction.

6.2.2 CALIBRATION OF YOUNG'S MODULUS

To determine the Young's modulus value, a PDMS cantilever beam produced under the same processing conditions was calibrated with a piezoresistive silicon force sensor (AE801, SensorOne, USA), similar to the process described in [57]. It has been demonstrated that Young's modulus characterized from bulk PDMS and a micro-PDMS structure, both constructed with the same microfabrication parameters, differ within 5% [156].

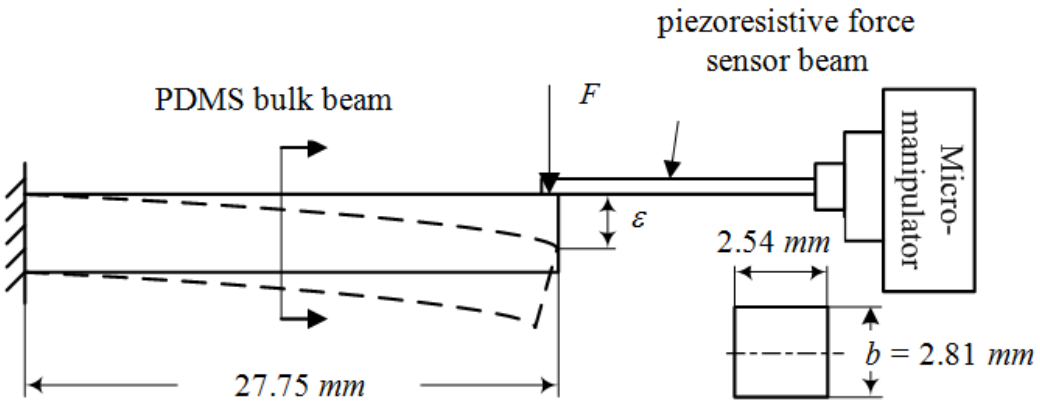

Figure 6.5 System setup for PDMS Young's modulus calibration.

As shown in Figure 6.5, the sensor was controlled to push the free end of the PDMS cantilever beam. In the calibration experiment, the contact area was carefully controlled such that the loads applied to the PDMS cantilever beam can be treated as concentrated forces. The stiffness of the silicon force sensor is $2\ N\ mm^{-1}$, from which deflections of the sensor beam were calculated. The deflection of the PDMS bulk cantilever

beam is thus equivalent to the difference between the displacement of the micromanipulator (MP-285, Sutter, USA) and the deflection of the sensor beam.

The calibration data points pairing the applied force F and free-end deflection ε of the bulk beam, shown in Figure 6.6, were substituted into the following mechanics model describing pure-bending cantilever beams

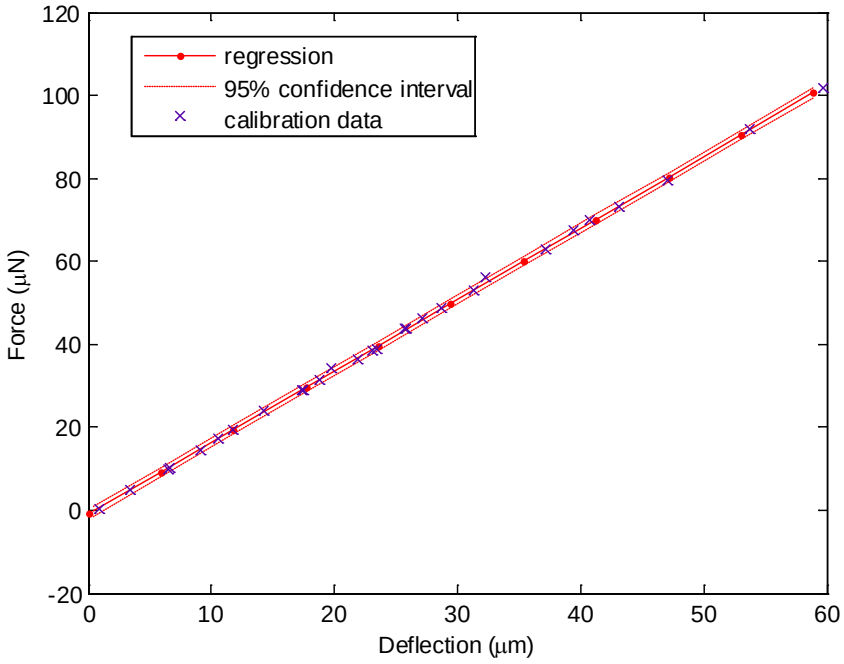

Figure 6.6 Calibration results of the PDMS cantilever beam.

to calibrate the Young's modulus [155]:

$$F = \frac{3EI}{h^3}\varepsilon \tag{6.9}$$

where $I = ab^3/12$. a and b are rectangular cross-section dimensions of the beam where b is the dimension in the plane of bending. The Young's modulus value was determined to be 2.6 MPa, which is in good agreement

with the previously reported value based on the same fabrication procedure [157].

6.2.3 PILLAR STIFFNESS

As *C. elegans* has a cylindrical body shape, it is assumed that the worm applies forces to the pillar at its half height location. Thus, l in expression (6.8) is taken as half of the worm width, indicating that the stiffness of the pillar varies with the worm width. Normally, a worm has a relatively constant body width except at its tapered head and tail. While there is some variation across individual worms as well, the worm width could be measured visually at the contact body part to compensate for these variations. Given the Poisson ratio ($\gamma = 0.5$) for PDMS [158], substituting the calibrated Young's modulus E, diameter (i.e., d) and height (i.e., h) of the pillar, and worm width (i.e., $2l$) into expression (6.8) gives the quantitative stiffness, as shown in Table 6.1, for varying worm widths in a typical range.

Parameters	Worm Width - $2l$ (μm)	Pillar Stiffness (μN/μm)
$\gamma = 0.5$	10	77.25
$E = 2.6$ MPa	20	30.16
$d = 40$ μm	40	10.65
$h = 100$ μm	60	5.58
	80	3.50
	100	2.43

Table 6.1 Pillar stiffness for varying worm width.

6.2.4 VISUAL TRACKING OF PILLAR DEFLECTION

An image processing algorithm was developed to track pillar deflection with sub-pixel accuracy. Figure 6.7 shows a worm moving inside pillars, where the deflection of those pillars with worm force loads is visually noticeable. Without loss of generality, three pillars, labeled in green, yellow and red colors in Figure 6.7, were chosen as the example.

For each pillar subject to deflection, the tracking is twofold: (i) to track the image patch containing the top circular surface of the pillar. (ii) to detect the circular center position accurately. The deflection is equivalent to the displacement of the circle center with respect to its neutral position where the load is zero.

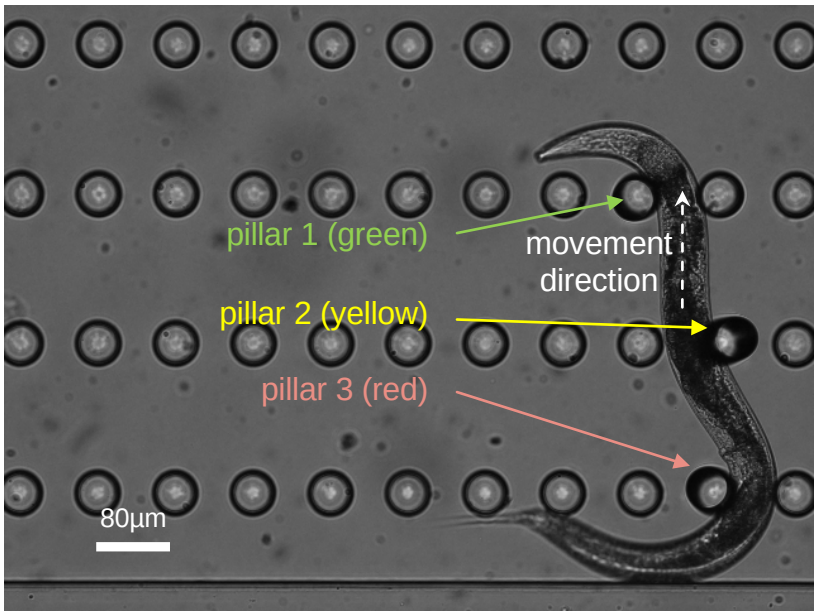

Figure 6.7 *C.elegans* moves inside the array of micropillars and deflects three-labeled pillars of interest.

A template matching algorithm with template update is used to track the motion of the deflecting pillars, providing processing areas for the subsequent least-squares circle detection (LSCD) to determine the pillars' center positions. Template matching with constant template update permits small changes in image patterns between successive frames of images; therefore, it is capable of robustly tracking the top surfaces of the deflecting pillars. Accumulative errors caused by updating templates are eliminated in the subsequent detection of circular centers using the LSCD algorithm. For detailed use of the template matching refer to [159].

The image patch tracked by template matching contains the deflecting pillar, whose circular surface or contour is used to detect the center position with LSCD. Thresholding a tracked image patch (Figure 6.8(a)) results in a binary image (Figure 6.8(b)). The curve edge of pillar top

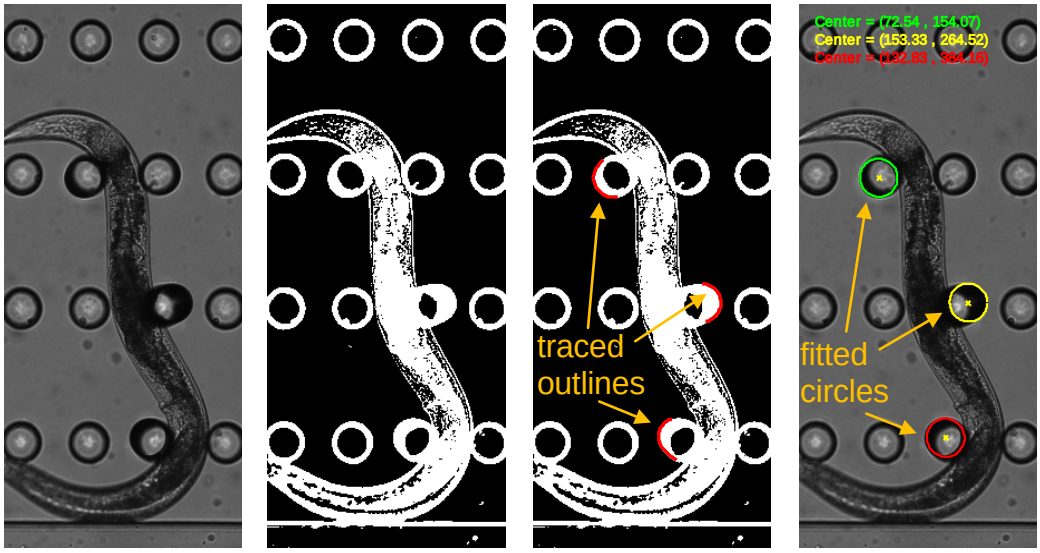

(a) (b) (c) (d)

Figure 6.8 Sub-pixel visual tracking results. (a) Original image patch. (b) The image after conversion to binary. (c) The outmost portion along the deflection of the pillars used for circle fitting. (d) Final fitted circles.

surface is then extracted for circle fitting. During curve edge extraction, only half portion of noncontact part (Figure 6.8(c)) was selected for circle fitting, with the objective of minimizing the error in the circle detection process. The other half was discarded as it is distorted due to the fact that the view is blocked by a portion of the worm body which can cause significant errors in circle fitting.

A least-square fitting algorithm was then used to fit the extracted curve edge points to a circle. Let traced points be (x_i, y_i), $i = 0,1,2,\dots,n-1$. The LSCD algorithm minimizes the following objective function, which is the sum of squares of algebraic distance from the n curve edge points to the circle center:

$$G(x_c, y_c, r) = \sum_{i=0}^{n-1}\left[(x_i - x_c)^2 + (y_i - y_c)^2 - r^2\right]^2 \tag{6.10}$$

Here, x_c and y_c are the coordinates of the circle center and r is the circle radius, which are to be determined. Define $A = -2x_c$, $B = -2y_c$ and $C = x_c^2 + y_c^2 + r^2$, then expression (6.10) can be rewritten as

$$G(A, B, C) = \sum_{i=0}^{n-1}\left(x_i^2 + y_i^2 + Ax_i + By_i + C\right)^2 \tag{6.11}$$

Differentiating expression (6.11) with respect to A, B and C and letting the derivatives be zero yields a set of linear equations:

$$\sum_{i=0}^{n-1}\left(x_i^2 + y_i^2 + Ax_i + By_i + C\right)x_i = 0 \tag{6.12}$$

$$\sum_{i=0}^{n-1}\left(x_i^2 + y_i^2 + Ax_i + By_i + C\right)y_i = 0 \tag{6.13}$$

$$\sum_{i=0}^{n-1}\left(x_i^2 + y_i^2 + Ax_i + By_i + C\right) = 0 \tag{6.14}$$

By solving this linear equation set, the center coordinates and radius of the circle are obtained. The standard deviation of the algebraic distances of the n curve edge points to the fitted circle center can be obtained by

$$\sigma = sqrt\left[G(x_c, y_c, r)/n\right] = sqrt\left\{\sum_{i=0}^{n-1}\left[\left(x_i - x_c\right)^2 + \left(y_i - y_c\right)^2 - r^2\right]^2 / n\right\} \tag{6.15}$$

Figure 6.8(d) shows the final fitted circle. The deflection of the pillar is therefore a directional vector pointing from its neutral (fixed) center to its updated center.

6.3 *C. ELEGANS* FORCE MEASUREMENT EXPERIMENT

6.3.1 NEMATODE CULTURE

Wild-type (N2) *C. elegans* nematodes were cultured as described by Brenner [77]. Regular 90 mm Nematode Growth Medium (NGM) Petri dishes were prepared for culturing *C. elegans*. The basal medium contained 3 g/L NaCl; Bacto-peptone, 2.5 g/L; Agar, 21 g/L. 1 L of distilled water was added to the basal media which was autoclaved at 121°C at 15 psi. The basal media was cooled to 55°C and the following were added aseptically: 1 mL cholesterol (5 mg/mL in ethanol), 1 mL 1M CaCl , 1 mL 1M MgSO and 25 mL 1M KH PO. A 100 mL sample of a 24 hr *E. coli* OP50 grown in Nutrient Broth was spread onto the medium and incubated for 24 hrs. An approximately 1 cm square piece of agar from the previous *C. elegans*

culture was inoculated onto the *E. coli* OP50 NGM and incubated at 20°C for 3-5 days before harvesting of nematodes.

6.3.2 DEVICE LOADING

Prior to loading of *C.elegans*, the surface of the PDMS measurement device was rendered hydrophilic by use of a laboratory corona treater (Electro-Technic Products). The top of the device was then covered with a standard 22×22 mm glass coverslip (ESCO Inc.) to enclose the channel part containing the micropillar array. Following this, a small drop of de-ionized water (DI) was dispensed onto the uncovered inlet by pipette, filling the channel via capillary force. This pre-loading of the device with water provides the moisturized environment required for the worm to move naturally. However, to minimize the effect of fluids on motion, the amount of water was critically controlled so that only a very thin layer of water with a negligible thickness relative to the worm width exists throughout the channel. Young adult *C. elegans*, picked at the L4 stage and cultivated at 20°C on plates for 12-18 hrs before experiments, were individually transferred from the culture dish by use of an inoculating needle and carefully placed in the open channel inlet. Each worm was given at least 5 minutes for acclimation in the new structured environment before it was imaged.

6.3.3 EXPERIMENTAL SETUP AND DATA PROCESSING

Worm movement through the pillar arrays was imaged using a Nikon Eclipse 80i fluorescence microscope under 10× magnification in bright-field mode. Figure 6.7 was recorded under this condition to have both the worm and surrounding pillars inside the field of view. A digital camera (DS-5Mc, Nikon) was used to record movies at 8 HZ for subsequent force

analysis on a PC. The microscopy stage was manually moved in a discrete manner only when the worm was about to move beyond the field of view of the camera which is desired for reducing potential disturbances caused by the stage movement on the worm's locomotive behavior. Image segments recorded while the stage was kept stationary were post-processed using the developed image processing algorithm to determine pillar deflection vectors, and to calculate corresponding forces using the established linear force-deflection model (expression (6.1)). Particularly, a video segment containing 35 frames during which the three pillars (shown in Figure 6.7) were seen to have most significant deflections (or forces) imposed by different parts of the worm body. Therefore these frames were considered for processing to examine the force measurement system. It should be noted that although the image frames were processed offline, the image processing software is readily capable for real-time force analysis as the vision-based deflection measurement involving template matching and LSCD algorithm amounts to less than 24 ms for processing for each image frame.

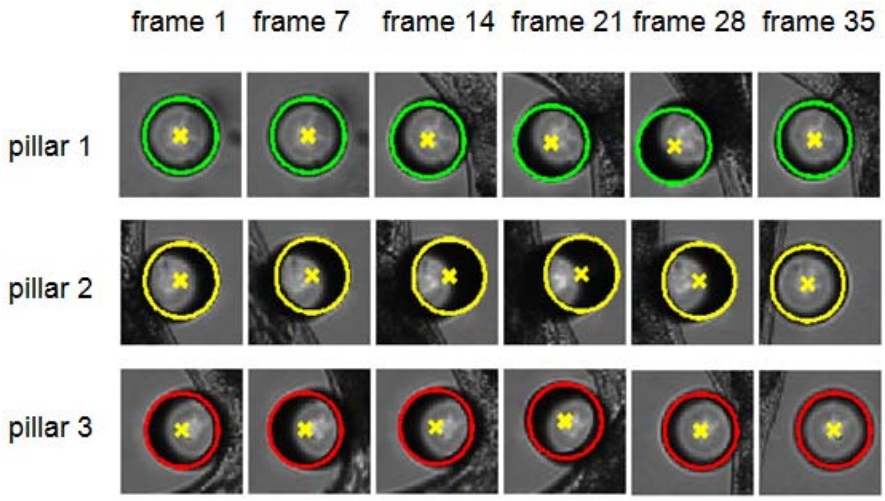

Figure 6.9 Visual tracking of pillars. Outlined is the fitted circle with center labeled by ×.

Figure 6.9 gives sample demonstration of micropillars being visually tracked over time.

6.3.4 FORCE RESOLUTION

For the imaging system with equal pixel size in both *x*- and *y*-directions, which is the case for this study, force resolution, ∂f, is given by the following expression

$$\partial f = k \cdot u \cdot \sigma \tag{6.16}$$

where k is the stiffness of the pillar given by expression (6.8), u is the pixel size in either direction, and σ is the standard deviation given in expression (6.15) representing the visual tracking resolution for the pillar deflection.

Visual tracking of the pillar center was conducted with 35 image patches each containing a pillar. Figure 6.9 shows the fitted circles for the three pillars (indicated in Figure 6.7) for every seven frames. The tracking resolution was found to be 0.05 ± 0.01 pixel. The pixel size was calibrated to be 1.18×1.18 μm/pixel. Corresponding to a L4 worm with average width of 60 μm, the stiffness of the pillar is 5.58 μN/μm (in Table 6.1), thus the force resolution is 0.33 μN.

6.3.5 FORCE MEASUREMENT RESULTS

Figure 6.10(a) shows the force measurements for the three pillars which underwent load from the worm at one image frame. The capability of giving both magnitude and direction of the force renders the force measurement system suitable for constantly tracking the dynamic force trends in *C. elegans* continuous motion over a period of time.

For the selected three pillars, the curve of their load force magnitude and 3D view of force vectors vs. image frame index when the worm forwarded is plotted in Figure 6.10(b) and Figure 6.11 respectively.

Table 6.2 shows the maximum absolute value of force received by three pillars in x and *y* coordinate directions and in total ($\vec{F} = \overrightarrow{F_x} + \overrightarrow{F_y}$). In the example, *C. elegans* was observed to generate a maximum force of 55.41 μN to the micropillars corresponding to a peak deflection of 20.36 μm, while having a continuous force output spectrum.

Figure 6.12 demonstrates the cumulative distribution of calculated forces (for all non-zero forces on the three pillars). Sorting the forces ascendantly and scaling them with respect to the greatest between 0 to 1 with steps of one over the number of sorted forces, a nearly linear cumulative distribution function (CDF) can be obtained. This implies an approximately uniform distribution of forces. This result shows a highly variable and continuous force level produced by the nematode, as supposed to be consistent with biological results and the anatomy of *C. elegans*.

Parameters	Pillar 1	Pillar 2	Pillar 3
max | f_x | (μN)	28.40	51.76	28.01
max | f_y | (μN)	16.38	18.72	10.69
max | f | (μN)	32.11	55.41	28.08

Table 6.2 Maximum forces imposed to the three pillars of interest by *C.elegans*.

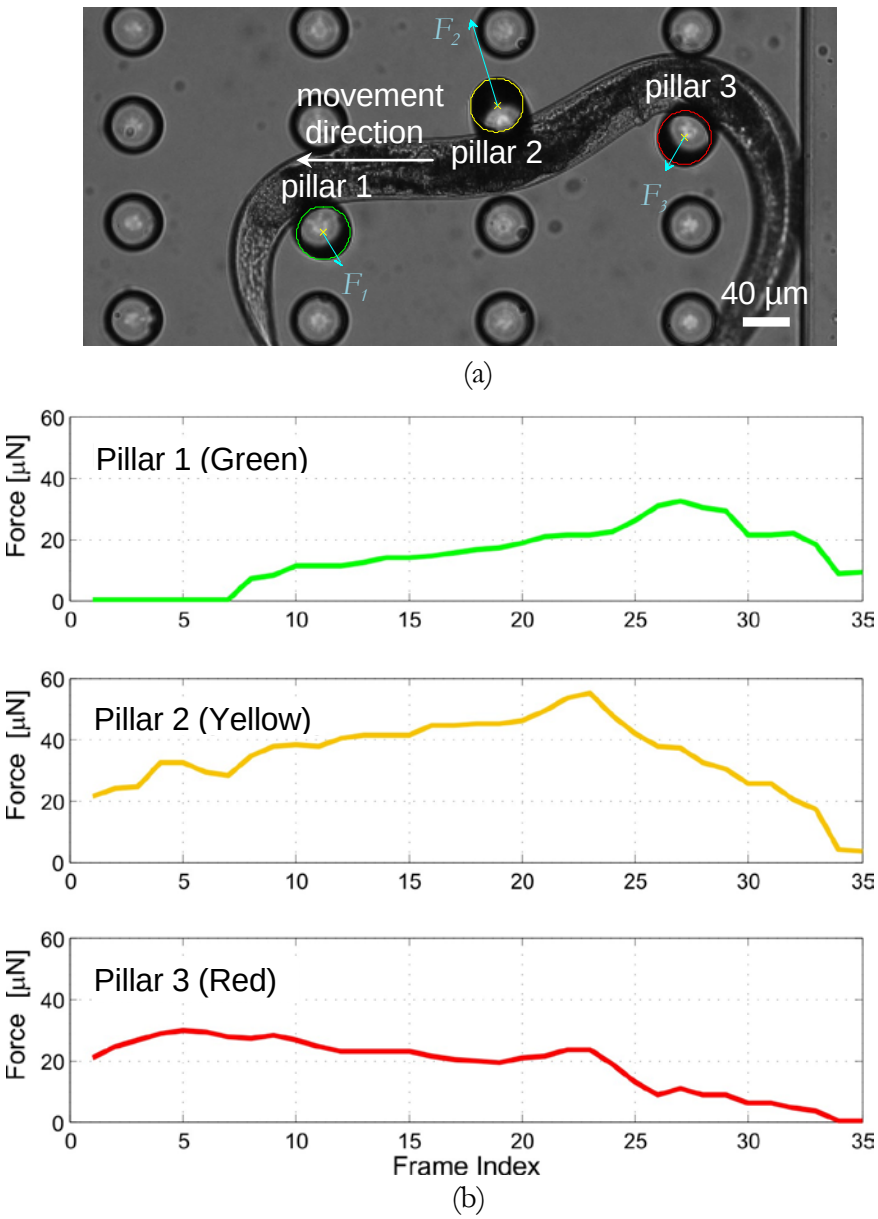

Figure 6.10 Example of the deflection-based force measurement. Three pillars (green, yellow and red) are chosen and tracked by the image processing algorithm to demonstrate force measurement. (a) Optical micrograph of *C. elegans* moving through the quadruple micropillar arrangement with fitted circles for tracking and resolved force vectors superimposed on the image. Movement direction is from right to left. (b) Plot of the magnitude of force exerted on the individual pillars vs. frame index.

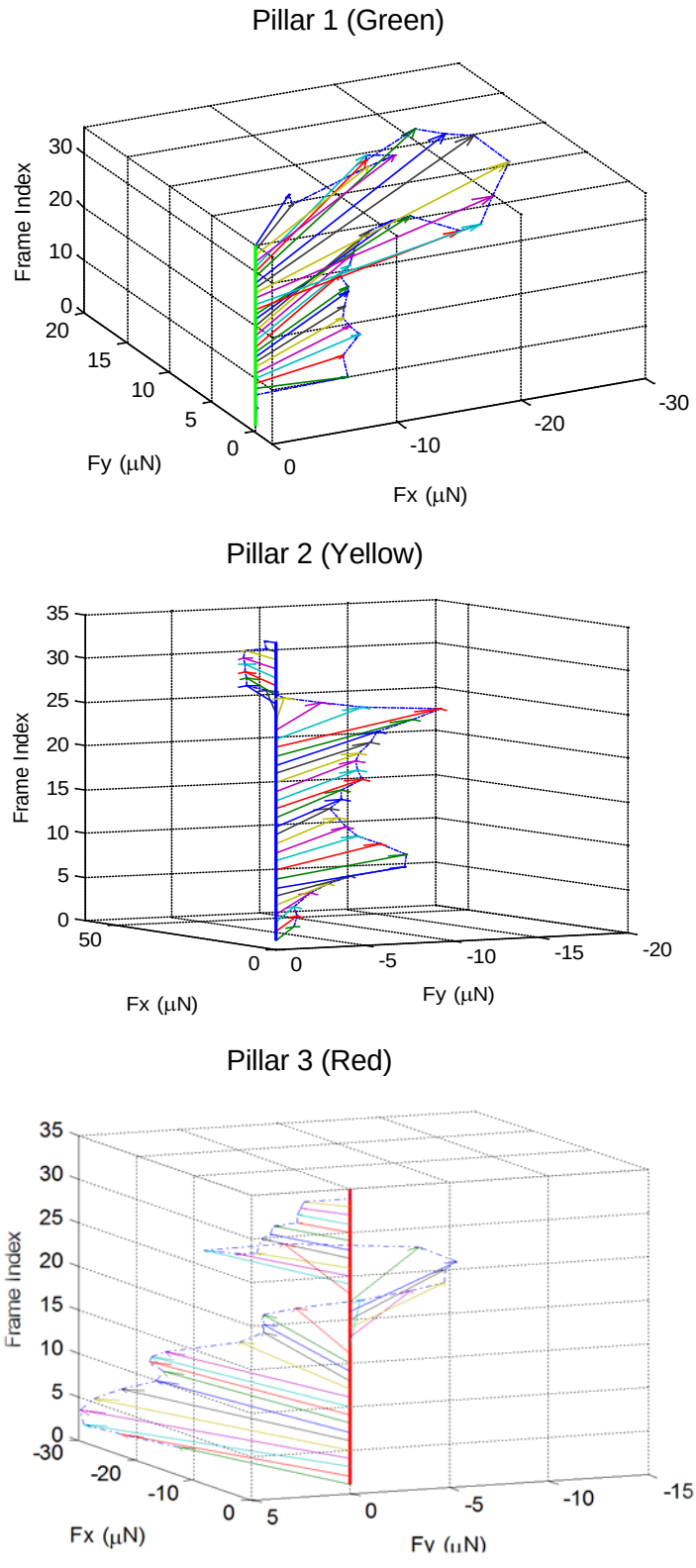

Figure 6.11 3D view of force vectors measured through visually measured deflections of three pillars of interest vs. frame index.

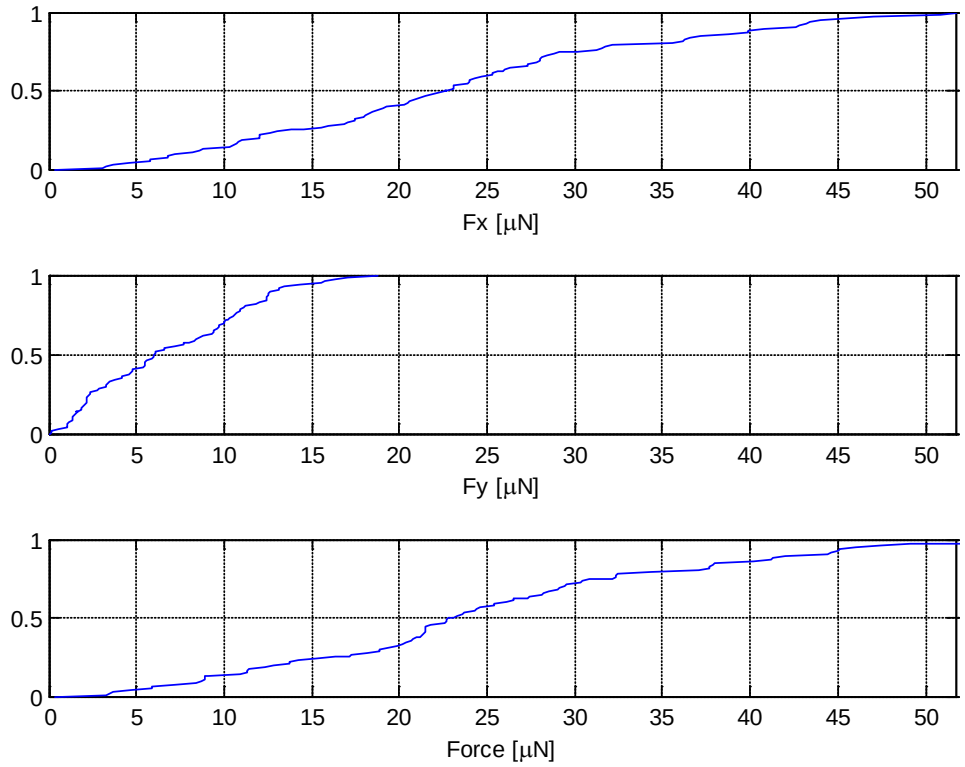

Figure 6.12 Cumulative distribution of locomotive forces on the three example pillars along x-axis, y-axis and in total. The nearly linear cumulative distribution function implies an approximately uniform distribution of forces, as supposed to be in accordance with the anatomy of *C. elegans* and biological observations of muscle force outputs.

6.4 SUMMARY

This Chapter demonstrated a novel system to infer forces from measured micropillar deflections. The system consisted of a microfabricated PDMS device to load *C. elegans* into a matrix of micropillars in a channel and an image processing algorithm. The image processing algorithm was shown to be able to accurately track the deflected pillars top circle and track their center points. The developed

system is able to visually resolve force with a 0.33 μN resolution. A maximum force level of 55.41 μN for a young adult wild type of *C. elegan* was observed. Cumulative distribution of locomotive forces suggested an approximately uniform distribution of forces. This is in accordance with the anatomy of *C. elegans* and biological observations of muscle force outputs.

"In order to succeed, your desire for success should be greater than your fear of failure."

Bill Cosby
1937-present, American author

Chapter 7

AUTOMATED VISION-BASED FORCE MEASUREMENT OF MOVING *C. ELEGANS*

This Chapter extends the force measurement system presented in the previous Chapter to introduce an automated tracking and force measurement system for *C. elegans* in motion. The system is capable of quantifying multi-point locomotive forces. This contributes to achieving more thorough force pattern analysis and extraction of *C. elegans'* locomotion characteristics. In particular, this Chapter introduces an image processing algorithm for tracking the *C. elegans* and deflecting micropillars while the microscopy stage is in motion.

7.1 AUTOMATED VISUAL MEASUREMENT OF PILLAR DEFLECTION

Figure 7.1 shows the top view of *C. elegans* moving inside array of micropillars, where the deflection of those pillars with *C. elegans* force loads is visually noticeable. For each pillar subject to deflection, top circular surface should be fitted a circle to detect the circular center position. The deflection is equivalent to the displacement of the circle center with respect to its neutral position where the load is zero. An image processing algorithm is developed to detect and track those pillars which are in contact with *C. elegans* moving in array of pillars, and measure their deflection all automatically. It processes stream of image frames in four main steps, namely, i) identifying contact pillars and worm, ii) detecting circles for contact pillars, iii) determining neutral position for contact pillars, and iv) tracking pillars.

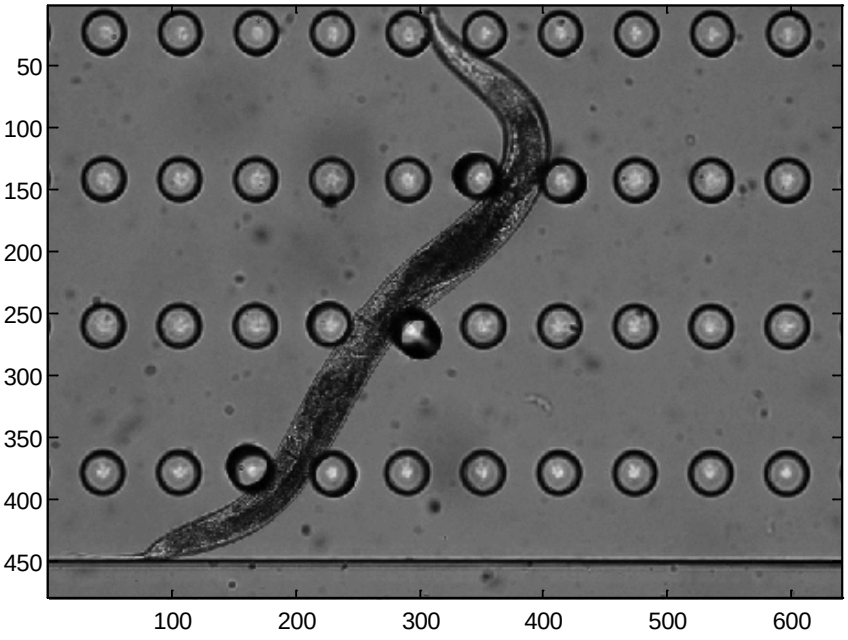

Figure 7.1 A raw image frame showing *C.elegans* inside the matrix of micropillars.

7.1.1 DETECTING CONTACT PILLARS AND WORM

Pillars of interest for force measurement purposes are those that worm contacts and would force against. Thus, it is necessary to separate non-contact pillars from contact pillars for next steps to improve accuracy and efficiency.

As Figure 7.2 indicates, all non-contact pillars are isolated from either the worm body or neighboring pillars. In contrast, contact pillars (highlighted in red) are mixed together with *C. elegans*, forming the largest object in the image. This is generally true for all image frames and results in an algorithm to differentiate non-contact pillars and contact ones. The detailed steps follow.

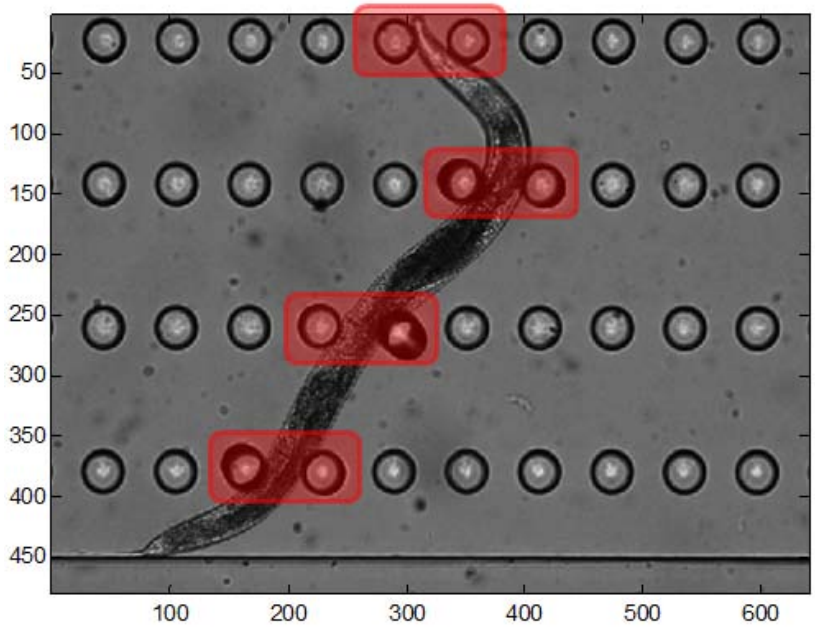

Figure 7.2 Targeted contact pillars (highlighted in red) to detect.

1. The gray-scale raw image is binarized with an optimized threshold empirically found to give the best result for subsequent steps. Figure 7.3(a) shows the resultant binary image.

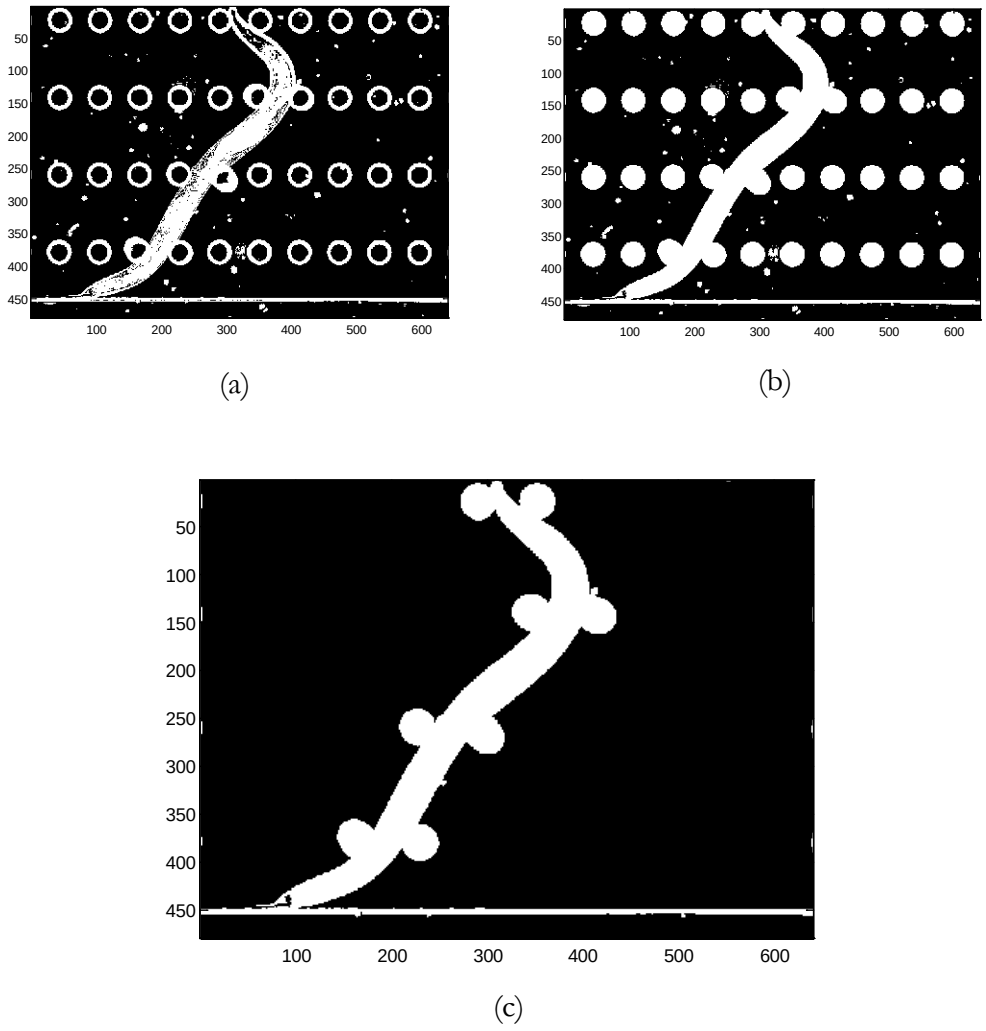

Figure 7.3 Noncontact pillars elimination process. (a) Converting to binary image. (b) Filling holes. (c) Detected contact pillars and worm.

2. An algorithm based on morphological reconstruction [160] is applied to fill in holes in the binary image. A hole is defined as a block of black pixels enclosed by a block of connected white pixels. This step aims at labeling all objects with white pixels. Figure 7.3(b) shows resultant image with holes filled.

3. Counting the number of white pixels of each isolated object, the object with the largest number is taken as the combination of worm

and the contact pillars. Figure 7.3(c) shows the resultant image with all non-contact pillars removed, indicating the non-contact pillars' coordinates can be determined.

7.1.2 DETECTING CIRCLES FOR CONTACT PILLARS

As their name indicates, contact pillars are partially overlapped/ occluded by the worm body. It is required to detect these top view circles for contact pillars (Figure 7.4).

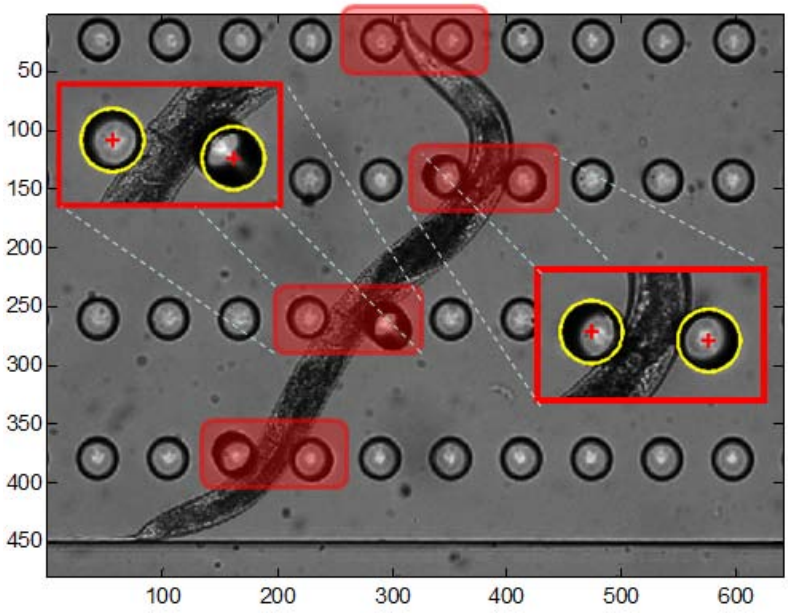

Figure 7.4 Top view circles for contact pillars subject to detect.

To separate these circular pillars from the worm body, a circle detection algorithm based on Hough transform [161] and array of accumulators [162] is adapted. Before applying of Hough transform, the raw image is processed with the Sobel operator only in the area consisting of contact pillars and worm, rather than in the entire image. The resultant gradient image is then used in Hough transform for circle detecting.

A circle in the 2-D x-y image plane (also called as geometric space) can be defined as

$$(x-a)^2+(y-b)^2=r^2 \tag{7.1}$$

where $\{a,b,r\}$ is a triplet defining the center and radius of the circle. Hough transform suggests that any point (x_i,y_i) in geometric space could be transformed onto a conical surface in the a-b-r parameter space described by

$$(x_i-a)^2+(y_i-b)^2=r^2 \tag{7.2}$$

Therefore, each 2-D point is mapped to a 3-D right circular cone surface. If any two cones in the parameter space intersect at $\{a_0,b_0,r_0\}$, their corresponding points in geometric space lie on the same circle characterized by this triplet [163]. In implementation, a 3-D array of accumulators representing the 3-D parameter space would be defined. For those points on the perimeter of a same circle, a triplet will correspond to the accumulation cell where the locally largest number of cone surfaces intersects.

For the device used in this work, the pillars have a known diameter. Thus, in the parameter space, r in expression (7.2) is a constant and a 2-D array of accumulator has been used.

Normally, in implementation of the Hough transform, each edge point is mapped to the full spectrum of those discretized accumulator. The computation burden has been lessened by using image gradient of the edge point. In principle, for an edge point (x_i, y_i) on a circle $\{a_0, b_0, r_0\}$, its

gradient should point to the circle center [164]. If $f(\bar{x})$ represents the gray level at $\bar{x} = (x_i, y_i)$ in the original image and $\nabla(\bar{x})$ represents the gradient of $f(\bar{x})$, then let the modulus and direction of $\nabla(\bar{x})$ be denoted by $g(\bar{x})$ and $\Phi(\bar{x})$ respectively. Therefore, in complex number notation

$$\nabla(\bar{x}) = g(\bar{x})e^{j\Phi(\bar{x})} \tag{7.3}$$

Let's $\nabla_1(\bar{x})$ and $\nabla_2(\bar{x})$ represent the horizontal and vertical terms of $\nabla(\bar{x})$ respectively:

$$\nabla(\bar{x}) = (\nabla_1(\bar{x}), \nabla_2(\bar{x})) \tag{7.4}$$

These terms are calculated from $f(\bar{x})$:

$$\nabla_1(\bar{x}) = \frac{f(\bar{x} + (s,0)) - f(\bar{x} - (s,0))}{2s} \tag{7.5}$$

$$\nabla_2(\bar{x}) = \frac{f(\bar{x} + (0,s)) - f(\bar{x} - (0,s))}{2s} \tag{7.6}$$

where s equals a positive integer. The gradient $\nabla(\bar{x})$ is calculated from terms of $\nabla_i(\bar{x}), i = 1,2$ by

$$g(\bar{x}) = \sqrt{\nabla_1^2(\bar{x}) + \nabla_2^2(\bar{x})} \tag{7.7}$$

$$\Phi(\bar{x}) = tan^{-1}\frac{\nabla_2(\bar{x})}{\nabla_1(\bar{x})} \tag{7.8}$$

If $\bar{x}_i$ lies on a circle embedded in $f(\bar{x})$, then the gradient of $f(\bar{x})$ at $\bar{x} = \bar{x}_i$ will point to the center of the circle.

In other words, the center point (a_0, b_0) is collinear with (x_i, y_i) and the slope of the straight line is given by the gradient. In comparison, without the gradient information, the center point (a_0, b_0) should be searched through a circular (2π) range around (x_i, y_i). In real computation, therefore, an angle range Φ around the gradient is specified to narrow the searching range of (a_0, b_0) in the parameter space. As a result, the computation burden drops by a factor of $2\pi/\Phi$ [164].

Figure 7.5 shows the Hough transform array of accumulators for the case shown in Figure 7.1. Note there are eight peaks in the graph, corresponding to the eight contact pillars. Figure 7.6 illustrates top view of array of accumulators for Hough transform. The eight brightest points correspond to the circle centers, *x*-*y* coordinates correspond to the image plane. The *x*-*y* coordinates of the peaks correspond to the pillar centers. Figure 7.7 shows the eight detected circles and centers superimposed on the raw image.

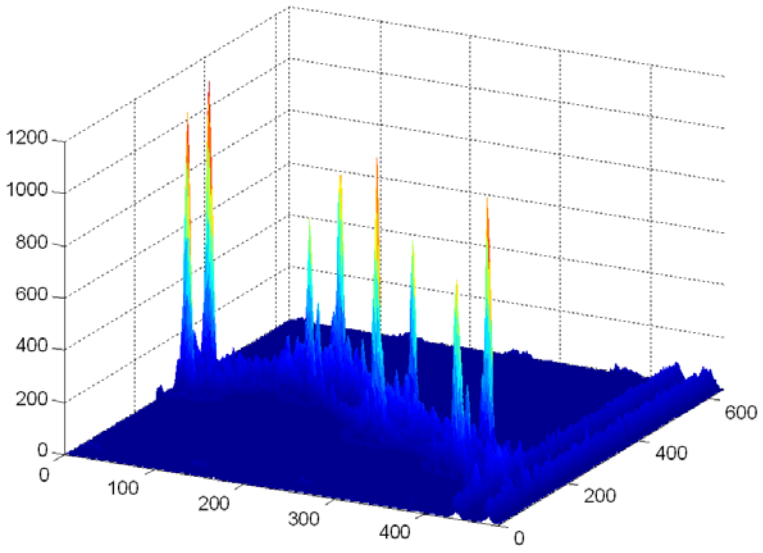

Figure 7.5 3-D view of array of accumulators. Note the *x*-*y* coordinates correspond to the image plane. Spikes correspond to circle centers.

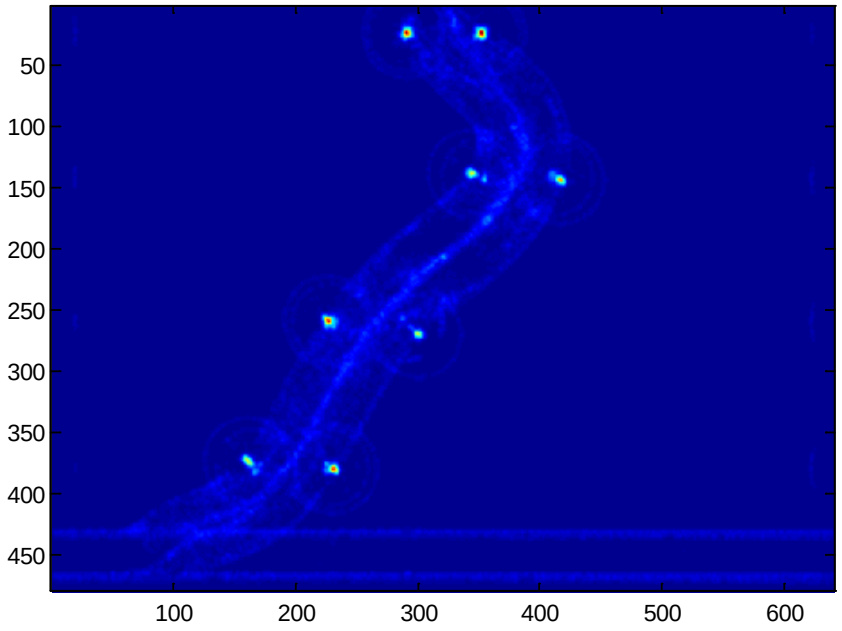

Figure 7.6 Top view of array of accumulators for Hough transform for the case shown in Figure 7.5. Note here the eight brightest points correspond to the circle centers, *x*-*y* coordinates correspond to the image plane.

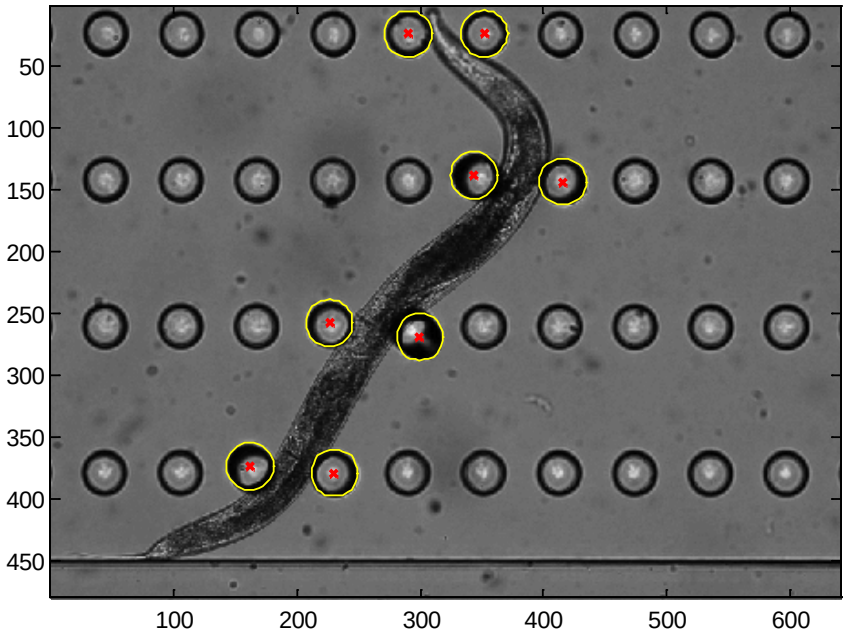

Figure 7.7 The eight detected contact pillars (yellow circles) and corresponding centers (red x's) superimposed on the raw image.

7.1.3 DETERMINING NEUTRAL POSITION FOR CONTACT PILLARS

For each contact pillar, the deflection, Δ in expression (6.1), caused by the worm is equivalent to the displacement of the circle center with respect to its neutral position where the load is zero. The neutral center point of these contact pillars have been interpolated from the center points of neighboring non-contact pillars, by making use of the known geometric parameters (pillars span equidistantly in row and column directions for the device) as illustrated in Figure 7.8. The Hough transform again is used to obtain the center points for non-contact pillars, whose region in the image was determined in Section 7.1.1.

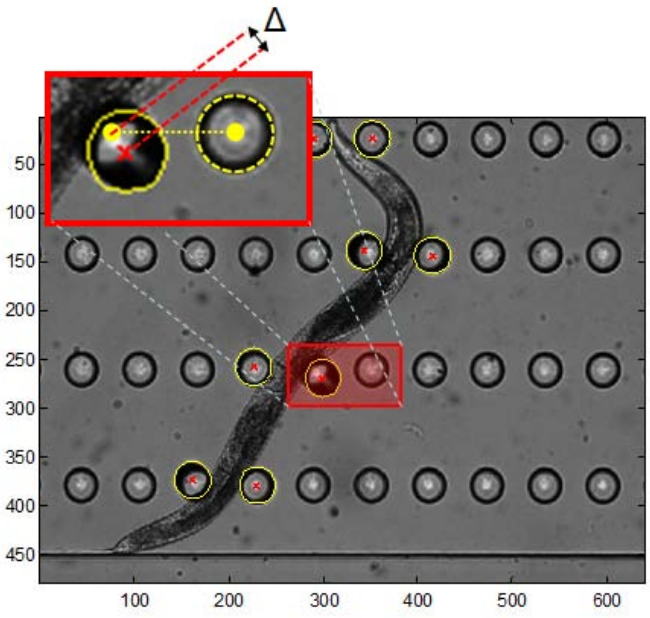

Figure 7.8 Determining neutral center point of a contact pillar interpolated from the center point of a neighboring non-contact pillar. Δ denotes the displacement of the contact pillar with respect to its neutral position.

7.1.4 TRACKING CONTACT PILLARS

While *C.elegans* moves beyond the camera's field of view, microscopy stage moves to bring the worn back to the view which in turn changes the location of pillars in the image. In order to the algorithm be able to track the contact pillars continuously and index them correctly as the stage moves, the new location is required to be obtained as depicted in Figure 7.9.

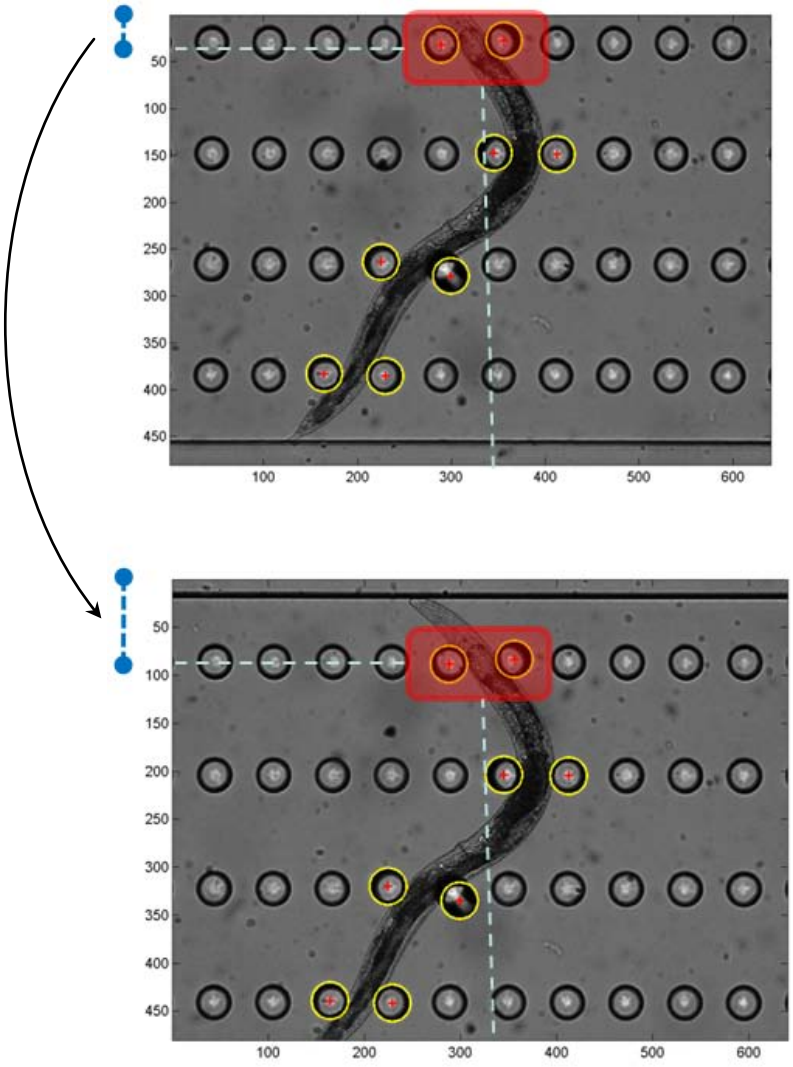

Figure 7.9 Relocation of pillars while microscopy stage moves.

An algorithm based on normalized cross-correlation for template matching [165] is adapted to calculate pillars relocation. Let's $f_1(x, y)$ and $f_2(x, y)$ represent two successive image frames. Then, the algorithm takes the following steps:

1. Calculates cross-correlation of f_1 and f_2.

2. Finds local sums by computing running sums.

3. Uses local sums to normalize the cross-correlation to get correlation coefficients. In here, normalization of f_1 and f_2 vectors to unit length leads to a cosine-like normalized correlation coefficient matrix of *C* with elements of

$$c(u, v) = \frac{\sum_{x,y}[f_2(x, y) - \bar{f}_2^{u,v}][f_1(x - u, y - v) - \bar{f}_1]}{\sqrt{\sum_{x,y}[f_2(x, y) - \bar{f}_2^{u,v}]^2 \sum_{x,y}[f_1(x - u, y - v) - \bar{f}_1]^2}} \quad (7.9)$$

where $\bar{f}_1$ is the mean of f_1 and $\bar{f}_2^{u,v}$ is the mean of f_2 in the region under f_1.

4. Calculates offset between f_2 and f_1:

$$x_{offset} = d_x - i_{c_{max}} \quad (7.10)$$

$$y_{offset} = d_y - j_{c_{max}} \quad (7.11)$$

where ($i_{c_{max}}$, $j_{c_{max}}$) is the element index of matrix C with maximum value and (d_x , d_y) is image frames dimension along x and y. x_{offset} and y_{offset} represent offset along x and y axes respectively.

5. Adds offset values to the location of each pillar in f_1 to determine corresponding pillar relocation in f_2.

Such a template matching algorithm with constant template update permits small changes (due to the *C. elegans* motion) in image patterns between successive frames of images; therefore, it is capable of robustly tracking the top surfaces of the contact pillars.

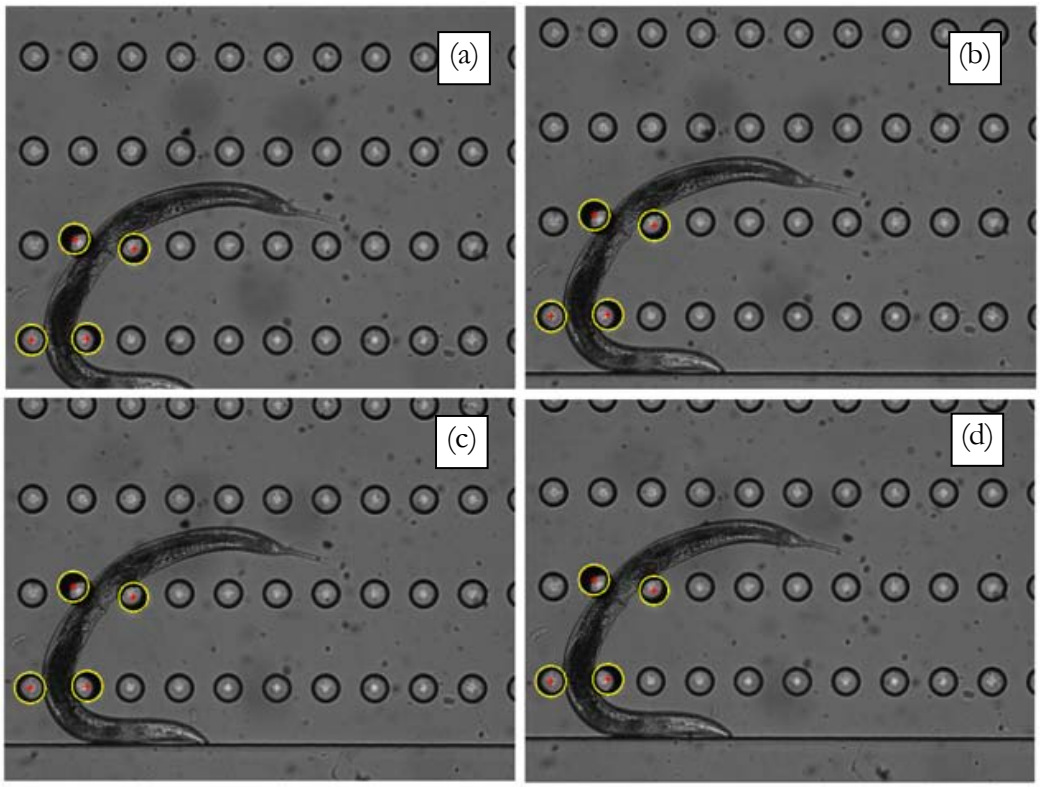

Figure 7.10 Four consecutive image frames (a)-(d) with horizontal motion for the microscopy stage. Note the four contact pillars are constantly tracked.

Figure 7.10 and Figure 7.11 show two sets of four consecutive processed image frames even when microscopy stage was in move along vertical and horizontal axes respectively in the aim of bringing the worm back to the camera's field of view. Tracking of contact pillars proves to work very well.

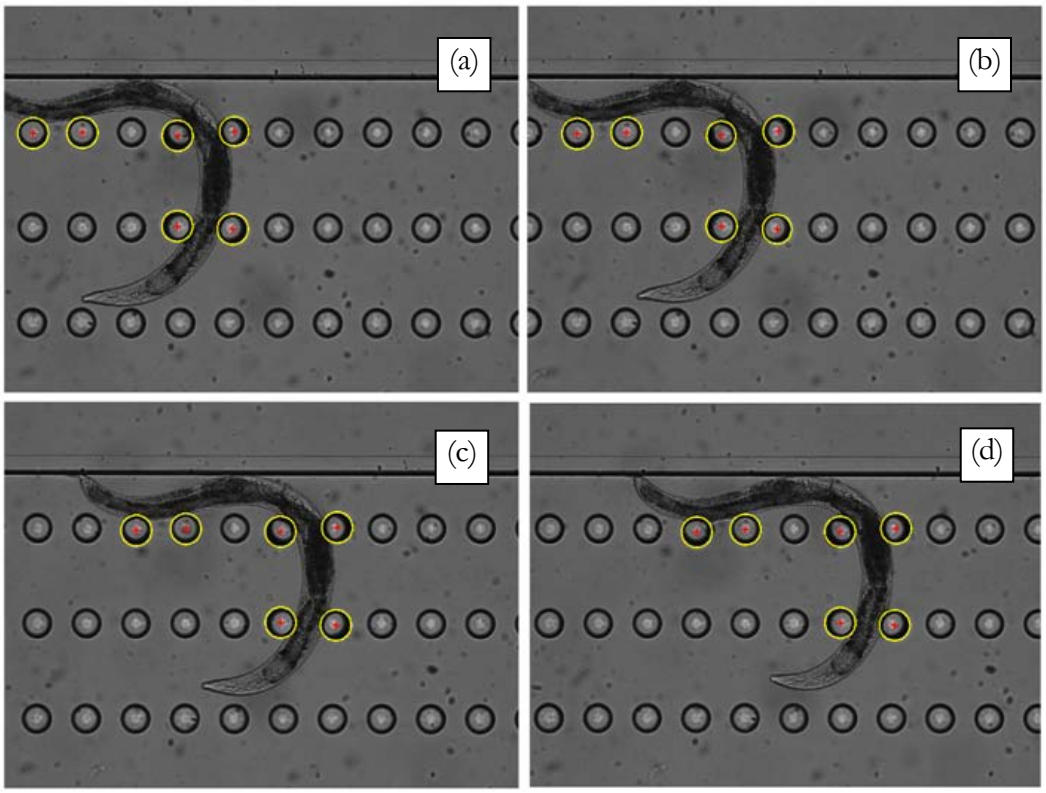

Figure 7.11 Four consecutive image frames (a)-(d) with vertical motion for the microscopy stage. Note the six contact pillars are constantly tracked.

Figure 7.12 shows the multi-point force measurement of pillars which the worm had a whole contact interaction (i.e., initial contact, more deflecting, and exit of contact). During this course, the developed force measurement system is capable of constantly tracking the dynamic force trends in *C. elegans* continuous motion. The presented system enables collecting as much data as desired and high-throughput screening of force patterns in *C. elegans* locomotive phenotypes.

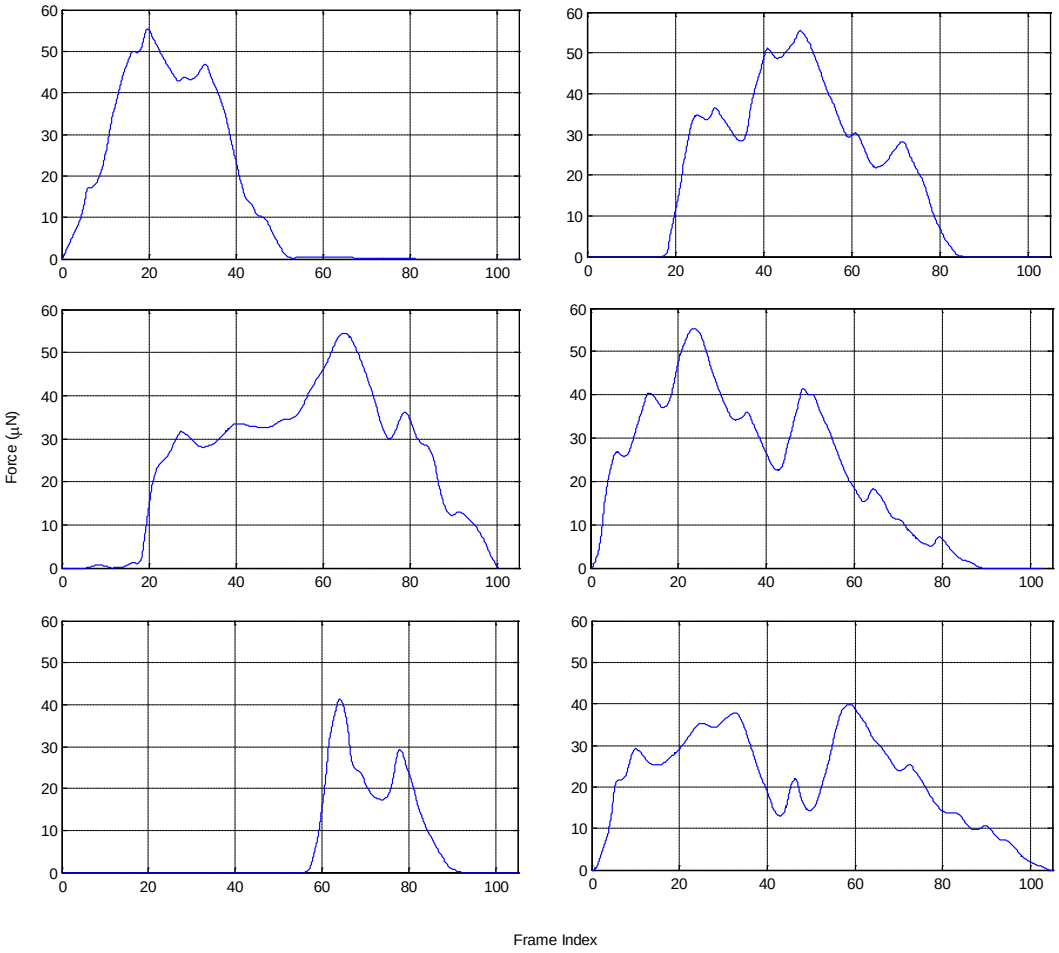

Figure 7.12 Plot of multi-point force measurement exerted on six contact pillars vs. frame index over the course from initial contact till exit of the contact between the pillars and worm while the microscopy stage is in move.

7.2 OBSERVATIONS AND DISCUSSION

Three interesting observations are obtained which may have important implications for *C. elegans* biomechanics and dynamics modeling, although more experiments should be done for conclusive results.

The first observation is that the force was always normal to the curve of worm motion trajectory, indicating the lateral force is the main thrust, which generates the curvature of the worm body and subsequently the

curved motion. The same mechanism exists [100] for a worm moving on an agar surface, which does not have any enhanced structures such as pillars in this study. Interestingly, it implies that the worm maintains its motion generation mechanism by producing lateral thrust regardless of its environment, which can be either natural (i.e., agar surface) or artificially structured such as pillars. This mechanism may be inherent in the muscle contraction of *C. elegans*.

The second observation is that when the worm forwarded, different body parts generate randomly varying force levels for motion. This suggests that the worm body cannot be treated as a linear or constant force generator in biomechanics modeling. Quantitatively, the forwarding worm is observed to be able to produce a maximum force at the 55.41 μN level. This maximum force is generated before the worm moves faster, indicating burst forces are fuelling *C. elegans* accelerating motion. The nonlinear curve of the differentiated forces shows that the worm generates time-varying forces corresponding to the structured environment. The maximum differentiation values between two frames (i.e., 1/8 s) for magnitude 13.42 μN and direction 4.94°, indicates that the worm is able to change its force at speed of 107.36 μN/s and 39.52 °/s. These quantitative values, enabled for the first time by the on-chip force measurement system, can be useful for establishing *C. elegans* biomechanics and dynamics models.

The third observation is that when forwarding, the worm is able to positively synchronize the force levels generated by different body parts. The force level showed an increase followed by a decrease, with the pattern being the same for all three pillars contacting different parts of the worm. This positive synchronization in force level suggests that all the

muscle arms of *C. elegans* work in a same pace during motion, probably by collectively receiving either an 'increase force' or 'decrease force' signal at each single moment from the corresponding neurons.

7.3 SUMMARY

This Chapter introduced an automated tracking and multi-point force measurement system for moving *C. elegans*. The developed force measurement system was capable of constantly tracking the dynamic force trends in *C. elegans* continuous motion using an image processing algorithm. The algorithm automatically infers forces using measured micropillar deflections according to the structure of the device and the transparency of PDMS. It is suggested that the reported system can be combined with existing small-organism screening systems and has the potential to enable high-throughput screening of force patterns in *C. elegans* locomotive phenotypes.

"Logic will get you from A to Z; imagination will get you everywhere."

Albert Einstein
1879-1955, German-born physicist

Chapter 8

CONCLUSION AND FUTURE DIRECTIONS

This Chapter summarizes the main contributions of this thesis and draws conclusions to the research. Recommendations for future work are also made.

8.1 THESIS SUMMARY AND CONCLUSION

The work presented in this thesis contributes to the understanding of force interaction and sensing in the field of bio-micromanipulation. This is achieved through the introduction of a novel haptically enabled microrobotic system for cell injection and a first-of-its-kind on-chip system for dynamic force measurement of *C. elegans*.

The haptically enabled microrobotic system integrates the operator's haptic sensory modality to offer immense benefits over conventional approaches. A 3D position-to-position kinematic mapping strategy was presented to provide the bio-operator with the ability to move the micropipette in a manner similar to handheld needle insertion. The performance of the approach was discussed and the importance of the mapping workspaces, scaling factor, tracking delay and resolution were demonstrated. Other than providing an intuitive method to control the microrobot, the proposed mapping framework layed the foundation for rendering haptic feedback/assistance to the bio-operator while conducting the cell injection operation.

To achieve adequate control of the micromanipulator as required by the haptically enabled cell injection system, an ANFIS-based system identification and control scheme was introduced. It was demonstrated that the control scheme is capable of high precision tracking control. The system's performance for different scaling factors was examined and experimental results suggest that the tracking delays are bounded to the $176 \pm 1\ ms$ and $194 \pm 1\ ms$ with $0.2\mu m$ and $0.04\mu m$ resolutions in coarse and fine modes respectively.

In order to provide the bio-operator with haptic guidance during cell injection, this thesis introduced three haptic virtual fixtures. The virtual fixtures, namely the planar, axial, and volumetric virtual fixtures haptically assist the bio-operator to approach the immobilised cell, insert inside the cell and inject at the desired location. The volumetric virtual fixtures are based on symmetric volume (neiloid, cone and paraboloid) force fields. In order to generatate the virtual force field within the volumetric fixtures, a multi-charged particle system model was proposed and also optimised for

real-time operation. The force field operates by applying forces to the bio-operator's hand so as to guide (suggest) the desired trajectory to the penetration point *P* (volumetric vertex) on the cell membrane. After the bio-operator has penetrated the cell, the axial virtual fixture guides motion in the direction of the micropipette's longitudinal axis. Then, the virtual fixture plane restricts the operator from moving beyond the deposition target location. Given the nature of the cell injection task, success rate is considered as more important than completion time. As such, the findings of the performance evaluations suggest that the paraboloid is the best choice of the three force field-based virtual fixtures. Results demonstrated the sucessful operation of the haptically enabled microrobotic cell injection system. Furthermore, in order to facilitate virtual offline bio-operator training, a novel approach to replicating the physical cell injection system using a virtual environment was introduced.

The micropillar-based on-chip system was introduced for force pattern characterization of *C. elegans* in motion. The system consists of a PDMS (Polydimethylsiloxane) micropillar-based device and a vision-based algorithm to resolve force from the deflection of the cantilever-like micropillars. The microfabricated PDMS device allowed *C. elegans* to move in a matrix of micropillars. A force-deflection mechanics model and image processing algorithm were introduced to infer forces from measured micropillar deflections. In order to be able to constantly detect and track micropillars contact an optimized Hough transform technique with an array of accumulators and a template matching algorithm based on normalized cross-correlation were adapted. This provided the ability to quantify multi-point locomotive forces of moving *C.elegans*.

The system demonstrated the ability to constantly measure the force exerted by *C. elegans* in motion. The measured force was provided with both magnitude and direction and a 0.33 μN resolution. The provision of both force magnitude and direction renders the system suitable for the tracking of *C. elegans* continuous motion over a period of time. Analysis of the locomotive force's cumulative distribution indicates a nearly linear CDF (cumulative distribution function). This suggests an approximately uniform distribution of forces in accordance with *C. elegans* anatomy. The measured forces show that *C. elegans* modulates their force levels across a continuum based on the direction of movement or resistance experienced. These findings match biological observations of muscles with a continuous force output spectrum. The maximum differentiation values between two frames (i.e., 1/8 s) for force magnitude (13.42 μN) and direction (4.94°), show that *C. elegans* was able to change the exerted force at speeds of 107.36 μN/s and 39.52 °/s. The attainment of these values was enabled for the first time by the on-chip force measurement system. The system may prove useful for establishing *C. elegans* biomechanic and dynamic models.

8.2 FUTURE DIRECTIONS

The haptically enabled microinjection system introduced in this thesis provides valuable haptic assistance/feedback during cell injection. While the haptic virtual fixtures guide the bio-operator during the cell injection process, it is also desirable to provide the bio-operator with the real-time cell indentation force (Figure 3.2) . To contribute towards achieving this, the author has collaborated in the following ongoing projects 1) A 3D particle-based biological cell model for haptic microrobotic cell injection

[166] and 2) A PVDF-based (Polyvinylidene Fluoride) 3D force sensor for micro and nano manipulation [167].

The cell modeling research effort aims to achieve a method combining the vision-based sensing technique introduced in Chapters 6 and 7, and a 3D particle-based model which simulates the deformation of the cell membrane and corresponding cellular forces during cell injection. The model considers the inner cell organelles effective to the cell shape, membrane's mechanical behaviour, liquid-like property of the cell and the external imposed forces including micropipette tip forces. The membrane is considered as a viscoelastic material modeled by DEM (discrete element method). The result is that the micropipette's tip is tracked with respect to the membrane of the real cell, and the motion of the tip is input to the model. The model then indicates the indentation forces applied by the micropipette to the membrane during cell injection. Such a cell model facilitates haptic representation of the cell membrane indentation force to provide real-time force feedback to the operator. The model can also be used to replicate the cell injection process in a virtual training environment.

Most of the cell injection force sensors reported in the literature are limited to measuring force in 1D or 2D [37, 60-65, 159]. The aim of the PVDF-based force sensor project is to achieve real-time measurement of the cell indentation forces in 3D. The sensor consists of coupled PVDF (polyvinylidene fluoride) piezoelectric polymer film surfaces and a microfabricated SU-8 corner shape structure for trapping the cell. The 3D force sensor would then be used online to provide force feedback during cell injection or offline for developing a cell model for the virtual training system.

The proposed haptically enabled microrobotic system can be extended to provide haptic assistance in applications with similar requirements. Examples include micro-surgery [168-170], tele-micro-surgery [171-174] and even micro assembly [175] operations.

The automated system for measuring *C. elegans* motion is capable of collecting large amounts of data. This can facilitate thorough force pattern analysis and extraction of locomotion characteristics. The automated nature of the system allows force patterns for various *C. elegan*s locomotive behaviors to be obtained. Such behaviors include turning, foraging and forward/reversing. The analysis and comparison of these force patterns may help contribute to a better understanding of the relationship between arm muscles and the force patterns of *C. elegans* in motion.

The micropillar-based force measurement system can also be extended to other applications. One such application could be to investigate force patterns for swimming *C. elegans* [176-177]. Another application could be to optimize the configuration of pillars so as to enhance the locomotion of *C. elegans*. As reported in [73], the speed of wild-type *C. elegans* increased 10 times using structured agar pillars. Using the PDMS pillars can provide force measurement which would not be achievable using agar pillars. It would provide a comparison of *C. elegans* forces for different pillar structures. Such results may contribute to explaining the causes of enhanced locomotion.

The literature [178-182] indicates significant research interest in the development of an accurate mathematical model of *C.elegans* locomotion. The force measurement system introduced in the thesis is capable of constantly tracking the dynamic force vectors of continuous *C. elegans*

motion. In addition to dynamic forces, the structure and transparency of the device allows other locomotive metrics (e.g., speed, distance, wave amplitude) to be measured. Therefore, the system can provide valuable experimental information to contribute to achieving accurate *C. elegans* locomotion models.

As motioned in the background chapter of this thesis, one of the exciting directions of this work would also be the fusion of haptic microrobotic injection and *C. elegance* force measurement systems. Such a fusion forms an integrated system of precision microinjection and locomotion behavior analysis of *C. elegans*.

BIBLIOGRAPHY

[1] T. Fukuda and F. Arai, "Micromanipulation and robotic technology," *in Proceedings of International Conference on Modeling and Simulation of Microsystems, Semiconductors, Sensors and Actuators,* pp. 11-16, 6-8 April 1998.

[2] A. Ghanbari, B. Horan, S. Nahavandi, X. Chen, and W. Wang, "Haptic microrobotic cell injection system," *IEEE Systems Journal,* pp. 1-13, 2012.

[3] A. Ghanbari, B. Horan, S. Nahavandi, X. Chen, and W. Wang, "Towards haptic microrobotic intracellular injection," *in Proceedings of IEEE/ASME International Conference on Mechatronic and Embedded Systems and Applications,* pp. 1-8, 30 August - 2 September 2009.

[4] A. Ghanbari, X. Chen, and W. Wang, "Neuro-fuzzy microrobotic system identification for haptic intracellular injection," *in Proceedings of IEEE International Conference on Control and Automation,* pp. 860-866, 9-11 December 2009.

[5] A. Ghanbari, H. Abdi, B. Horan, S. Nahavandi, X. Chen, and W. Wang, "Haptic guidance for microrobotic intracellular injection," *in Proceedings of IEEE/RAS-EMBS International Conference on Biomedical Robotics and Biomechatronics,* pp. 162-167, 26-29 September 2010.

[6] A. Ghanbari, B. Horan, H. Abdi, S. Nahavandi, X. Chen, and W. Wang, "Haptic microrobotic intracellular injection assistance using virtual fixtures," *in Proceedings of International Conference on Control, Automation, Robotics and Vision,* pp. 781-786, 7-10 December 2010.

[7] A. Ghanbari, V. Nock, S. Johari, R. Blaikie, X. Chen, and W. Wang, "A micropillar-based on-chip system for continuous force measurement of *C. elegans*," *Journal of Micromechanics and Microengineering,* vol. 22, pp. 1-10, September 2012.

[8] A. Ghanbari, V. Nock, W. Wang, R. Blaikie, J. G. Chase, X. Chen, and C. E. Hann, "Force pattern characterization of *C. elegans* in motion," *in Proceedings of International Conference on Mechatronics and Machine Vision in Practice,* pp. 634-639, 2-4 December 2008.

[9] A. Ghanbari, V. Nock, R. Blaikie, X. Chen, J. G. Chase, and W. Wang, "Automated vision-based force measurement of moving *C. elegans*," *in Proceedings of IEEE International Conference on Automation Science and Engineering,* pp. 198-203, 21-24 August 2010.

[10] A. Ghanbari, V. Nock, W. Wang, R. Blaikie, J. G. Chase, X. Chen, and C. E. Hann, "Force pattern characterisation of Caenorhabditis elegans in motion," *International Journal of Computer Applications in Technology,* vol. 39, pp. 137-144, 2010.

[11] V. Khemka, D. See, J. See, J. Chang, S. Chou, and J. Tilles, "The capacity of a combined liposomal hepatitis B and C vaccine to stimulate humoral and cellular responses in mice," *Viral Immunology,* vol. 11, pp. 73-78, 1998.

[12] G. Fanning, "RNA as a target for host defense and anti-HIV drugs," *Current Drug Targets,* vol. 7, pp. 1607-1613, December 2006.

[13] G. Beretta, P. Perego, and F. Zunino, "Mechanisms of cellular resistance to camptothecins," *Current Medicinal Chemistry,* vol. 13, pp. 3291-3305, 2006.

[14] A. Kalota, S. E. Shetzline, and A. M. Gewirtz, "Progress in the development of nucleic acid therapeutics for cancer," *Cancer Biology and Therapy,* vol. 3, pp. 4-12, January 2004.

[15] J. Yu, M. A. Vodyanik, K. Smuga-Otto, J. Antosiewicz-Bourget, J. L. Frane, S. Tian, J. Nie, G. A. Jonsdottir, V. Ruotti, R. Stewart, Slukvin, II, and J. A. Thomson, "Induced pluripotent stem cell lines derived from human somatic cells," *Science,* vol. 318, pp. 1917-1920, December 2007.

[16] J. Sundaram, B. R. Mellein, and S. Mitragotri, "An experimental and theoretical analysis of ultrasound-induced permeabilization of cell membranes," *Biophysical Journal,* vol. 84, pp. 3087-101, May 2003.

[17] M. P. Rols, "Electropermeabilization, a physical method for the delivery of therapeutic molecules into cells," *Biochimica et Biophysica Acta-Biomembranes,* vol. 1758, pp. 423-428, March 2006.

[18] J. W. Park, "Liposome-based drug delivery in breast cancer treatment," *Breast Cancer Research,* vol. 4, pp. 95-99, April 2002.

[19] W. Wang, X. Y. Liu, and S. Yu, "High-throughput automated injection of individual biological cells," *IEEE Transactions on Automation Science and Engineering,* vol. 6, pp. 209-219, April 2009.

[20] X. D. Li, G. H. Zong, and S. S. Bi, "Development of global vision system for biological automatic micro-manipulation system," *in Proceedings of International Conference on Robotics and Automation,* vol. 1, pp. 127-132, 21-26 May 2001.

[21] J. E. Celis, "Microinjection of somatic-cells with micropipettes - comparison with other transfer techniques," *Biochemical Journal,* vol. 223, pp. 281-291, October 1984.

[22] T. Kasaya, H. Miyazaki, S. Saito, and T. Sato, "Micro object handling under SEM by vision-based automatic control," *in Proceedings of IEEE International Conference on Robotics and Automation* vol. 3, pp. 2189-2196, 10-15 May 1999.

[23] J. Sprague, L. Bayraktaroglu, D. Clements, T. Conlin, D. Fashena, K. Frazer, M. Haendel, D. G. Howe, P. Mani, S. Ramachandran, K. Schaper, E. Segerdell, P. Song, B. Sprunger, S. Taylor, C. E. Van Slyke, and M. Westerfield, "The zebrafish iInformation network: the zebrafish model organism database," *Nucleic Acids Research,* vol. 34, pp. 581-585, January 2006.

[24] M. S. McPeek, "From mouse to human: fine mapping of quantitative trait loci in a model organism," *Proceedings of the National Academy of Sciences of the United States of America,* vol. 97, pp. 12389-12390, 7 November 2000.

[25] Y. Sun and B. Nelson, "Biological cell injection using an autonomous microrobotic system," *The International Journal of Robotics Research,* vol. 21, pp. 861-868, October 2002.

[26] P. Scherp and K. Hasenstein, "Microinjection-a tool to study gravitropism," *Advances in Space Research,* vol. 31, pp. 2221-2227, May 2003.

[27] N. Tran, X. Liu, Z. Yan, D. Abbote, Q. Jiang, E. Kmiec, C. Sigmund, and J. Engelhardt, "Efficiency of chimeraplast gene targeting by direct nuclear injection using a GFP recovery assay," *Molecular Therapy,* vol. 7, pp. 248-253, February 2003.

[28] R. Kumar, A. Kapoor, and R. H. Taylor, "Preliminary experiments in robot/human cooperative microinjection," *in Proceedings of IEEE/RSJ International Conference on Intelligent Robots and Systems,* pp. 3186-3191, 27-31 October 2003.

[29] H. Matsuoka, T. Komazaki, Y. Mukai, M. Shibusawa, H. Akane, A. Chaki, N. Uetake, and M. Saito, "High throughput easy microinjection with a single-cell manipulation supporting robot," *Journal of Biotechnology,* vol. 116, pp. 185-194, March 2005.

[30] K. Kobayashi, K. Kato, M. Saga, M. Yamane, C. M. Rothman, and S. Ogawa, "Subzonal insemination of a single-mouse spermatozoon with a personal computer-controlled micromanipulation system," *Molecular Reproduction and Development,* vol. 33, pp. 81-88, September 1992.

[31] L. Mattos, E. Grant, R. Thresher, and K. Kluckman, "New developments towards automated blastocyst microinjections," *in Proceedings of IEEE International Conference on Robotics and Automation,* pp. 1924-1929, 10-14 April 2007.

[32] A. Pillarisetti, M. Pekarev, A. D. Brooks, and J. P. Desai, "Evaluating the role of force feedback for biomanipulation tasks," *in Proceedings of Symposium on Haptics Interfaces for Virtual Environment and Teleoperator Systems,* pp. 11-18, 25-26 March 2006.

[33] L. Mattos and D. Caldwell, "Interface design for microbiomanipulation and teleoperation," *in Proceedings of International Conferences on Advances in Computer-Human Interactions,* pp. 342-347, 1-7 February 2009.

[34] L. Mattos, E. Grant, R. Thresher, and K. Kluckman, "From teleoperated to automatic blastocyst microinjections: designing a new system from expert-controlled operations," *in Proceedings of IEEE/RSJ International Conference on Robots and Intelligent Systems,* pp. 4036-4041, 22-26 September 2008.

[35] L. S. Mattos, E. Grant, R. Thresher, and K. Kluckman, "Blastocyst microinjection automation," *IEEE Transactions on Information Technology in Biomedicine,* vol. 13, pp. 822-831, September 2009.

[36] M. Motamedi, M. T. Ahmadian, G. Vossoughi, S. M. Rezaei, and M. Zareinejad, "Adaptive sliding mode control of a piezo-actuated bilateral teleoperated micromanipulation system," *Precision Engineering - Journal of the International Societies for Precision Engineering and Nanotechnology,* vol. 35, pp. 309-317, April 2011.

[37] Z. Lu, P. Chen, J. Nam, R. Ge, and W. Lin, "A micromanipulation system with dynamic force-feedback for automatic batch microinjection," *Journal of Micromechanics and Microengineering,* vol. 17, pp. 314-321, 2007.

[38] Y. Zhang, M. Han, C. Shee, and W. Ang, "Automatic vision guided small cell injection: feature detection, positioning, penetration and injection," *in Proceedings of IEEE International Conference on Mechatronics and Automation,* pp. 2518-2523, 5-8 August 2007.

[39] S. Zappe, M. Fish, M. P. Scott, and O. Solgaard, "Automated MEMS-based Drosophila embryo injection system for high-throughput RNAi screens," *Lab on a Chip,* vol. 6, pp. 1012-1019, 2006.

[40] S. Hashmi, P. Ling, G. Hashmi, M. Reed, R. Gaugler, and W. Trimmer, "Genetic-transformation of nematodes using arrays of micromechanical piercing structures," *Biotechniques,* vol. 19, pp. 766-770, November 1995.

[41] K. Chun, G. Hashiguchi, H. Toshiyoshi, H. Fujita, Y. Kikuchi, J. Ishikawa, Y. Murakami, and E. Tamiya, "An array of hollow microcapillaries for the controlled injection of genetic materials into animal/plant cells," *in Proceedings of IEEE International Conference on Micro Electro Mechanical Systems,* pp. 406-411, 17-21 January 1999.

[42] S. B. Leighton and M. J. Brownstein, *Array-Type multiple cell injector*: Patent U.S.5262128, Nov. 1993.

[43] R. O. Ginaven and D. Facciotti, *Needle array and method of introducing biological substances*: Patent U.S.5457041, Oct. 1995.

[44] Y. Yeshurun, *Systems and methods for the transport of fluids through a biological barrier and production techniques for such systems*: Patent U.S.6558361, May 2003.

[45] K. Salisbury, F. Conti, and F. Barbagli, "Haptic rendering: introductory concepts," *IEEE Computer Graphics and Applications Magazine, Special issue on Haptic Rendering,* pp. 24-32, April 2004.

[46] B. Baxter, V. Scheib, M. C. Lin, and D. Manocha, "DAB: Interactive haptic painting with 3D virtual brushes," *in Proceedings of ACM Siggraph Conference,* pp. 461-468, 12-17 August 2001.

[47] M. Lazzari, A. Francois, M. L. McLaughlin, J. Jaskowiak, W. L. Wong, M. Akbarian, E. Y. E. Kang, W. Peng, and W. R. Zhu, "Using haptics and a 'virtual mirror' to exhibit museum objects with reflective surfaces," *in Proceedings of International Conference on Advanced Robotics,* pp. 1247-1252, 30 June - 3 July 2003.

[48] A. Balijepalli and T. Kesavadas, "Value-addition of haptics in operator training for complex machining tasks," *Journal of Computing and Information Science in Engineering,* vol. 4, pp. 91-98, June 2004.

[49] B. Horan, Z. Najdovski, S. Nahavandi, and E. Tunstel, "Haptic control methodologies for telerobotic stair traversal," *International Journal of Intelligent Control and Systems,* vol. 13, pp. 3-14, 2008.

[50] Z. Najdovski, B. Horan, A. Bhatti, and S. Nahavandi, *Method and apparatus for haptic control*: Patent WO/2008/074081, 2008.

[51] S. K. Cho, H. Z. Jin, J. M. Lee, and B. Yao, "Teleoperation of a mobile robot using a force-reflection joystick with sensing mechanism of rotating magnetic field," *IEEE/ASME Transactions on Mechatronics,* vol. 15, pp. 17-26, February 2010.

[52] A. Mor, S. Gibson, and J. Samosky, "Interacting with 3-dimensional medical data: haptic feedback for surgical simulation," *in Proceedings of Phantom Users Group Workshop,* 27-30 September 1996.

[53] C. Basdogan, S. De, J. Kim, M. Muniyandi, H. Kim, and M. Srinivasan, "Haptics in minimally invasive surgical simulation and training," *IEEE Computer Graphics and Applications Magazine,* vol. 24, pp. 56-64, March 2004.

[54] C. Basdogan, C. H. Ho, and M. A. Srinivasan, "Virtual environments for medical training: graphical and haptic simulation of laparoscopic common bile duct exploration," *IEEE/ASME Transactions on Mechatronics,* vol. 6, pp. 269-285, September 2001.

[55] A. Gupta and M. K. O'Malley, "Design of a haptic arm exoskeleton for training and rehabilitation," *IEEE/ASME Transactions on Mechatronics,* vol. 11, pp. 280-289, Jun 2006.

[56] P. R. Ouyang, W. J. Zhang, M. M. Gupta, and W. Zhao, "Overview of the development of a visual based automated bio-micromanipulation system," *Mechatronics,* vol. 17, pp. 578-588, December 2007.

[57] X. Liu, Y. Sun, W. H. Wang, and B. Lansdorp, "Vision-based cellular force measurement using an elastic microfabricated device," *Journal of Micromechanics and Microengineering,* vol. 17, pp. 1281-1288, 2007.

[58] M. Ammi, H. Ladjal, and A. Ferreira, "Evaluation of 3D pseudo-haptic rendering using vision for cell micromanipulation," *in Proceedings of IEEE/RSJ International Conference on Intelligent Robots and Systems,* pp. 2115-2120, 9-15 October 2006.

[59] J. Kim, F. Janabi-Sharifi, and J. Kim, "Haptic feedback based on physically based modeling for cellular manipulation systems," *in Proceedings of International Conference on Haptics: Perception, Devices and Scenarios,* pp. 661-667, 10-13 June 2008.

[60] A. Pillarisetti, W. Anjum, J. P. Desai, G. Friedman, and A. D. Brooks, "Force feedback interface for cell injection," *in Proceedings of World Haptics Conference* pp. 391-400, 18-20 March 2005.

[61] C. Sung-Yong and S. Jae-Hong, "A new micro biological cell injection system," *in Proceedings of IEEE/RSJ International Conference on Intelligent Robots and Systems* vol. 2, pp. 1642-1647, 28 September - 2 October 2004.

[62] Y. Xie, D. Sun, H. Tse, C. Liu, and S. Cheng, "Force sensing and manipulation strategy in robot-assisted microinjection on zebrafish embryos," *IEEE/ASME Transactions on Mechatronics,* pp. 1-9, 2010.

[63] A. Sieber, P. Valdastri, K. Houston, C. Eder, O. Tonet, A. Menciassi, and P. Dario, "A novel haptic platform for real time bilateral biomanipulation with a MEMS sensor for triaxial force feedback," *Sensors and Actuators A: Physical,* vol. 142, pp. 19-27, March 2008.

[64] A. Pillarisetti, C. Keefer, and J. P. Desai, "Mechanical response of embryonic stem cells using haptics-enabled atomic force microscopy," in *Experimental Robotics*. vol. 54, O. Khatib*, et al.*, Eds., ed: Springer 2009, pp. 261-269.

[65] H. Huang, D. Sun, J. K. Mills, and W. J. Li, "Visual-based impedance force control of three-dimensional cell injection system," *in Proceedings of IEEE International Conference on Robotics and Automation,* pp. 4196-4201, 10-14 April 2007.

[66] Y. Sun, K. T. Wan, K. P. Roberts, J. C. Bischof, and B. J. Nelson, "Mechanical property characterization of mouse zona pellucida," *IEEE Transactions on Nanobioscience,* vol. 2, pp. 279-286, December 2003.

[67] T. *C. e.* S. Consortium, "Genome sequence of the nematode *C. elegans*: a platform for investigating biology," *Science,* vol. 282, pp. 2012-2018, December 1998.

[68] G. Wei, P. Cosman, C. C. Berry, F. Zhaoyang, and W. R. Schafer, "Automatic tracking, feature extraction and classification of *C. elegans* phenotypes," *IEEE Transactions on Biomedical Engineering,* vol. 51, pp. 1811-1820, October 2004.

[69] G. Tsechpenakis, L. Bianchi, D. N. Metaxas, and M. Driscoll, "A novel computational approach for simultaneous tracking and feature extraction of *C. elegans* populations in fluid environments," *IEEE Transactions on Biomedical Engineering* vol. 55, pp. 1539-1549, May 2008.

[70] C. Cronin, J. Mendel, S. Mukhtar, Y.-M. Kim, R. Stirbl, J. Bruck, and P. Sternberg, "An automated system for measuring parameters of nematode sinusoidal movement," *BMC Genetics,* vol. 6, February 2005.

[71] S.-J. Park, M. B. Goodman, and B. L. Pruitt, "Analysis of nematode mechanics by piezoresistive displacement clamp," *Proceedings of the National Academy of Sciences of the United States of America,* vol. 104, pp. 17376-17381, October 2007.

[72] L. Herndon, P. Schmeissner, J. Dudaronek, P. Brown, K. Listner, Y. Sakano, M. Paupard, D. Hall, and M. Driscoll, "Stochastic and genetic factors influence tissue-specific decline in ageing C. elegans," *Nature,* vol. 419, pp. 808 - 814, 2002.

[73] S. Park, H. Hwang, S. W. Nam, F. Martinez, R. H. Austin, and W. S. Ryu, "Enhanced Caenorhabditis elegans locomotion in a structured microfluidic environment," *Plos One,* vol. 3, June 2008.

[74] G. Anderson, W. Boyd, and P. Williams, "Assessment of sublethal endpoints for toxicity testing with the nematode Caenorhabditis

elegans," *Environmental Toxicology and Chemistry,* vol. 20, pp. 833 - 838, 2001.

[75] W. Boyd, R. Cole, G. Anderson, and P. Williams, "The effects of metals and food availability on the behavior of Caenorhabditis elegans," *Environmental Toxicology and Chemistry,* vol. 22, pp. 3049 - 3055, 2003.

[76] W. Boyd and P. Williams, "Comparison of the sensitivity of three nematode species to copper and their utility in aquatic and soil toxicity tests," *Environmental Toxicology and Chemistry,* vol. 22, pp. 2768 - 2774, 2003.

[77] S. Brenner, "The genetics of Caenorhabditis elegans," *Genetics,* vol. 77, pp. 71 - 94, 1974.

[78] L. Brundage, L. Avery, A. Katz, U.-J. Kim, J. E. Mendel, P. W. Sternberg, and M. I. Simon, "Mutations in a C. elegans Gq[alpha] Gene Disrupt Movement, Egg Laying, and Viability," *Neuron,* vol. 16, pp. 999-1009, 1996.

[79] T. A. Starich, R. K. Herman, and J. E. Shaw, "Molecular and Genetic Analysis of unc-7, a Caenorhabditis elegans Gene Required for Coordinated Locomotion," *Genetics,* vol. 133, pp. 527-541, March 1993.

[80] D. M. Miller-III, C. J. Niemeyer, and P. Chitkara, "Dominant unc-37 mutations suppress the movement fefect of a homeodomain mutation in unc-4, a neural specificity gene in Caenorhabditis elegans," *Genetics,* vol. 135, pp. 741-753, November 1993.

[81] S. J. Dixon and P. J. Roy, "Muscle arm development in Caenorhabditis elegans," *Development,* vol. 132, pp. 3079-3092, July 2005.

[82] N. Roussel, C. A. Morton, F. P. Finger, and B. Roysam, "A computational model for *C. elegans* locomotory behavior: application to multiworm tracking," *IEEE Transactions on Biomedical Engineering* vol. 54, pp. 1786-1797, October 2007.

[83] J. Gray and H. W. Lissmann, "The locomotion of nematodes," *The Journal of Experimental Biology,* vol. 41, pp. 135-54

March 1964.

[84] W. H. Wang, Y. Sun, S. J. Dixon, M. Alexander, and P. J. Roy, "A micropositioning system with real-time feature extraction capability for quantifying *C. elegans* locomotive behavior," *in Proceedings of IEEE International Conference on Automation Science and Engineering,* pp. 243-248, 22-25 September 2007.

[85] J. J. Norman, V. Mukundan, D. Bernstein, and B. L. Pruitt, "Microsystems for biomechanical measurements," *Pediatric Research,* vol. 63, pp. 576-583, May 2008.

[86] M. Sitti and H. Hashimoto, "Teleoperated touch feedback from the surfaces at the nanoscale: Modeling and experiments," *IEEE/ASME Transactions on Mechatronics,* vol. 8, pp. 287-298, June 2003.

[87] H. K. Chu, J. K. Mills, and W. L. Cleghorn, "MEMS capacitive force sensor for use in microassembly," *in Proceedings of IEEE/ASME International Conference on Advanced Intelligent Mechatronics,* pp. 797-802, 2-5 July 2008.

[88] S. Yantao, X. Ning, L. Wen Jung, and T. Jindong, "A high sensitivity force sensor for microassembly: design and experiments," *in Proceedings of IEEE/ASME International Conference on Advanced Intelligent Mechatronics,* vol. 2, pp. 703-708, 20-24 July 2003.

[89] R.-J. Chang and C.-Y. Cheng, "Vision-based compliant-joint polymer force sensor integrated with microgripper for measuring gripping force," *in Proceedings of IEEE/ASME International Conference on Advanced Intelligent Mechatronics,* pp. 18-23, 14-7 July 2009.

[90] J. Conia, B. S. Edwards, and S. Voelkel, "The micro-robotic laboratory: Optical trapping and scissing for the biologist," *Journal of Clinical Laboratory Analysis,* vol. 11, pp. 28-38, 1997.

[91] Z. Zhang, K. Huang, and C. H. Menq, "Design, implementation, and force modeling of quadrupole magnetic tweezers," *IEEE/ASME Transactions on Mechatronics,* pp. 1-10, 2009.

[92] L. Guangyong, X. Ning, Y. Mengmeng, F. Salem, D. H. Wang, and L. Jianping, "Manipulation of living cells by atomic force microscopy," *in Proceedings of IEEE/ASME International Conference on Advanced Intelligent Mechatronics,* vol. 2, pp. 862-867, 20-24 July 2003.

[93] G. T. Charras, P. P. Lehenkari, and M. A. Horton, "Atomic force microscopy can be used to mechanically stimulate osteoblasts and evaluate cellular strain distributions," *Ultramicroscopy,* vol. 86, pp. 85-95, January 2001.

[94] J. N. Fass and D. J. Odde, "Tensile force-dependent neurite elicitation via anti-{beta}1 integrin antibody-coated magnetic beads," *Biophysical Journal,* vol. 85, pp. 623-636, July 2003.

[95] R. M. Hochmuth, "Micropipette aspiration of living cells," *Journal of Biomechanics,* vol. 33, pp. 15-22, January 2000.

[96] A. K. Harris, P. Wild, and D. Stopak, "Silicone rubber substrata: a new wrinkle in the study of cell locomotion," *Science,* vol. 208, pp. 177-179, April 1980.

[97] J. L. Tan, J. Tien, D. M. Pirone, D. S. Gray, K. Bhadriraju, and C. S. Chen, "Cells lying on a bed of microneedles: an approach to isolate mechanical force," *Proceedings of the National Academy of Sciences of the United States of America,* vol. 100, pp. 1484-1489, February 2003.

[98] O. du Roure, A. Saez, A. Buguin, R. H. Austin, P. Chavrier, P. Siberzan, and B. Ladoux, "Force mapping in epithelial cell migration," *Proceedings of the National Academy of Sciences of the United States of America,* vol. 102, pp. 2390-2395, February 2005.

[99] Y. Zhao and X. Zhang, "Cellular mechanics study in cardiac myocytes using PDMS pillars array," *Sensors and Actuators A: Physical,* vol. 125, pp. 398-404, January 2006.

[100] Y. N. Xia and G. M. Whitesides, "Soft lithography," *Angewandte Chemie International Edition* vol. 37, pp. 551-575, March 1998.

[101] S. R. Lockery, K. J. Lawton, J. C. Doll, S. Faumont, S. M. Coulthard, T. R. Thiele, N. Chronis, K. E. McCormick, M. B. Goodman, and B. L. Pruitt, "Artificial dirt: microfluidic substrates for nematode neurobiology and behavior," *Journal of Neurophysiology,* vol. 99, pp. 3136-3143, June 2008.

[102] F. Zeng, C. B. Rohde, and M. F. Yanik, "Sub-cellular precision on-chip small-animal immobilization, multi-photon imaging and femtosecond-laser manipulation," *Lab on a Chip,* vol. 8, pp. 653-656, April 2008.

[103] C. B. Rohde, F. Zeng, R. Gonzalez-Rubio, M. Angel, and M. F. Yanik, "Microfluidic system for on-chip high-throughput whole-animal sorting and screening at subcellular resolution," *Proceedings of the National Academy of Sciences of the United States of America,* vol. 104, pp. 13891-13895, 28 August 2007.

[104] S. E. Hulme, S. S. Shevkoplyas, J. Apfeld, W. Fontana, and G. M. Whitesides, "A microfabricated array of clamps for immobilizing and imaging C-elegans," *Lab on a Chip,* vol. 7, pp. 1515-1523, 2007.

[105] J. H. Qin and A. R. Wheeler, "Maze exploration and learning in C-elegans," *Lab on a Chip,* vol. 7, pp. 186-192, 2007.

[106] J. M. Gray, D. S. Karow, H. Lu, A. J. Chang, J. S. Chang, R. E. Ellis, M. A. Marletta, and C. I. Bargmann, "Oxygen sensation and social feeding mediated by a *C. elegans* guanylate cyclase homologue," *Nature,* vol. 430, pp. 317-322, July 2004.

[107] J. C. Doll, N. Harjee, N. Klejwa, R. Kwon, S. M. Coulthard, B. Petzold, M. B. Goodman, and B. L. Pruitt, "SU-8 force sensing pillar arrays for biological measurements," *Lab on a Chip,* vol. 9, pp. 1449-1454, May 2009.

[108] H. Tabara, A. Grishok, and C. C. Mello, "RNAi in *C. elegans*: soaking in the genome sequence," *Science,* vol. 282, pp. 430-431, October 1998.

[109] I. Ruvinsky, U. Ohler, C. B. Burge, and G. Ruvkun, "Detection of broadly expressed neuronal genes in *C. elegans*," *Journal of Developmental Biology,* vol. 302, pp. 617-626, February 2007.

[110] P. Ruzanov, D. L. Riddle, M. A. Marra, S. J. McKay, and S. M. Jones, "Genes that may modulate longevity in *C. elegans* in both dauer larvae and long-lived daf-2 adults," *Journal of Experimental Gerontology,* vol. 42, pp. 825-839, April 2007.

[111] S. E. J. Fischer, "Small RNA-mediated gene silencing pathways in *C. elegans*," *The International Journal of Biochemistry and Cell Biology,* vol. 42, pp. 1306-1315, March 2010.

[112] K. G. Miller, M. D. Emerson, J. R. McManus, and J. B. Rand, "RIC-8 (Synembryn): A novel conserved protein that is required for Gqα signaling in the *C. elegans* nervous system," *Neuron,* vol. 27, pp. 289-299, August 2000.

[113] J. F. Nahabedian, H. Qadota, J. N. Stirman, H. Lu, and G. M. Benian, "Bending amplitude – A new quantitative assay of *C. elegans* locomotion: Identification of phenotypes for mutants in genes encoding muscle focal adhesion components," *Methods,* vol. 56, pp. 95-102, January 2012.

[114] C. C. Mello, J. M. Kramer, D. Stinchcomb, and V. Ambros, "Efficient gene transfer in *C. elegans*: extrachromosomal maintenance and integration of transforming sequences," *Trends in Genetics,* vol. 10, pp. 3959–3970, December 1991.

[115] R. C. Lee, R. L. Feinbaum, and V. Ambros, "The *C. elegans* heterochronic gene lin-4 encodes small RNAs with antisense complementarity to lin-14," *Cell,* vol. 75, pp. 843-854, December 1993.

[116] W. H. Wang, M. M. Alkaisi, J. G. Chase, X. Q. Chen, and C. E. Hann, "Suspended cell patterning for automatic microrobotic cell injection," *in Proceedings of IEEE/ASME International Conference on Mechatronic and Embedded Systems and Applications,* pp. 100-105, 12-15 October 2008.

[117] *MP-285 with ROE Operation Manual*: Sutter Instrument Co., 2009.

[118] J. Denavit and R. S. Hartenberg, "A kinematic notation for lower-pair mechanisms based on matrices," *Journal of Applied Mechanics,* vol. 22, pp. 215–221, June 1955.

[119] J. Craig, *Introduction to Robotics: Mechanics and Control*: Addison-Wesley Longman Publishing Co., Inc. Boston, MA, USA, 1989.

[120] *PHANTOM® Omni Technical Specifications*: The Sensable Technologies, 2009.

[121] S. N. Kurenov and J. C. Cendan, "Devices and Methods for Utilizing Mechanical Surgical Devices in a Virtual Environment," *US Patent App.12/446,587,* 2007.

[122] C. B. Zilles and J. K. Salisbury, "A constraint-based god-object method for haptic display," *in Proceedings of IEEE/RSJ International*

Conference on Intelligent Robots and Systems, vol. 3, pp. 146 - 151, 5-9 August 1995.

[123] V. Hayward, P. Gregorio, O. Astley, S. Greenish, M. Doyon, L. Lessard, J. McDougall, I. Sinclair, S. Boelen, and X. Chen, "Freedom-7: A high fidelity seven axis haptic device with application to surgical training," *Experimental robotics V: Lecture Notes in Control and Information Sciences,* vol. 232, pp. 443-456, 1998.

[124] O. Michel, "Webots: professional mobile robot simulation," *Journal of Advanced Robotic Systems,* vol. 1, pp. 39-42, November 2004.

[125] E. W. Bai, "A blind approach to the Hammerstein-Wiener model identification," *Automatica,* vol. 38, pp. 967-979, June 2002.

[126] D. Nauck, F. Klawonn, and R. Kruse, *Foundations of Neuro-Fuzzy Systems*. New York: Wiley, 1997.

[127] J. Vieira, F. M. Dias, and A. Mota, "Artificial neural networks and neuro-fuzzy systems for modelling and controlling real systems: a comparative study," *Engineering Applications of Artificial Intelligence,* vol. 17, pp. 265-273, April 2004.

[128] J. S. R. Jang, "ANFIS: adaptive-network-based fuzzy inference system," *IEEE Transactions on Systems Man and Cybernetics,* vol. 23, pp. 665-685, May/June 1993.

[129] M. A. Denai, F. Palis, and A. Zeghbib, "ANFIS based modelling and control of non-linear systems : a tutorial," *in Proceedings of IEEE International Conference on Systems, Man and Cybernetics,* vol. 4, pp. 3433-3438, 10-13 October 2004.

[130] J. S. R. Jang and S. Chuen-Tsai, "Neuro-fuzzy modeling and control," *Proceedings of the IEEE,* vol. 83, pp. 378-406, March 1995.

[131] J. S. Jang, C. T. Sun, and E. Mizutani, *Neuro-fuzzy and soft computing*. NJ: Prentice Hall, 1997.

[132] T. Takagi and M. Sugeno, "Fuzzy identification of systems and its applications to modeling and control," *IEEE Transactions on Systems Man and Cybernetics,* vol. 15, pp. 116-132, February 1985.

[133] L. Ljung, *System Identification:Theory for the User*. NJ: Prentice Hall, 1987.

[134] J. S. R. Jang, "Input selection for ANFIS learning," *in Proceedings of IEEE International Conference on Fuzzy Systems,* vol. 2, pp. 1493-1499, 8-11 September 1996.

[135] M. A. Denai, F. Palis, and A. Zeghbib, "Modeling and control of non-linear systems using soft computing techniques," *Applied Soft Computing,* vol. 7, pp. 728-738, June 2007.

[136] D. Psaltis, A. Sideris, and A. A. Yamamura, "A multilayered neural network controller," *IEEE Control Systems Magazine,* vol. 8, pp. 17-21, April 1988.

[137] J. J. Abbott, P. Marayong, and A. M. Okamura, "Haptic virtual fixtures for robot-assisted manipulation," *Robotics Research,* vol. 28, pp. 49-64, 2007.

[138] A. Bettini, S. Lang, A. Okamura, and G. Hager, "Vision assisted control for manipulation using virtual fixtures: Experiments at macro and micro scales," *in Proceedings of IEEE International Conference on Robotics and Automation,* pp. 3354-3361, 11-15 May 2002.

[139] P. Marayong, M. Li, A. M. Okamura, and G. D. Hager, "Spatial motion constraints: Theory and demonstrations for robot guidance using virtual fixtures," *in Proceedings of IEEE International Conference on Robotics and Automation,* pp. 1954-1959, 12-17 May 2003.

[140] P. Marayong and A. M. Okamura, "Speed-accuracy characteristics of human-machine cooperative manipulation using virtual fixtures with variable admittance," *Human Factors,* vol. 46, pp. 518-532, September 2004.

[141] W. T. Yu, R. Alqasemi, R. Dubey, and N. Pernalete, "Telemanipulation assistance based on motion intention recognition," *in Proceedings of IEEE International Conference on Robotics and Automation,* pp. 1121-1126, April 2005.

[142] M. Ammi and A. Ferreira, "Robotic assisted micromanipulation system using virtual fixtures and metaphors," *in Proceedings of IEEE International Conference on Robotics and Automation,* pp. 454-460, 10-14 April 2007.

[143] J. J. Abbott, G. D. Hager, and A. M. Okamura, "Steady-hand teleoperation with virtual fixtures," *in Proceedings of IEEE International Workshop on Robot and Human Interactive Communication,* pp. 145-151, 31 October - 2 November 2003.

[144] S. Payandeh and Z. Stanisic, "On application of virtual fixtures as an aid for telemanipulation and training," *in Proceedings of 10th Symposium on Haptic Interfaces for Virtual Environment and Teleoperator Systems,* pp. 18-23, 24-25 March 2002.

[145] L. B. Rosenberg, "Virtual fixtures - perceptual tools for telerobotic manipulation," *in Proceedings of IEEE Annual International Symposium on Virtual Reality,* pp. 76-82, 18-22 September 1993.

[146] G. Burdea and J. C. Zhuang, "Dexterous Telerobotics with Force Feedback - an Overview .1. Human-Factors," *Robotica,* vol. 9, pp. 171-178, April-June 1991.

[147] G. Burdea and J. C. Zhuang, "Dexterous telerobotics with force feedback - an overview .2. control and implementation," *Robotica,* vol. 9, pp. 291-298, July-September 1991.

[148] M. Westerfield, *The Zebrafish book: A guide for the laboratory use of zebrafish (Danio rerio)*: University of Oregon Press, 2000.

[149] W. Wang, D. Hewett, C. E. Han, J. G. Chase, and X. Q. Chen, "Application of machine vision for automated cell injection," *International Journal of Mechatronics & Manufacturing Systems,* vol. 2, pp. 120-134, 2009.

[150] O. Khatib, K. Yokoi, and A. Casal, "Cooperative tasks in mobile manipulation systems," *Intelligent Components for Vehicles,* pp. 245-250, 1998.

[151] J. C. Fraile, J. Perez-Turiel, J. L. Gonzalez-Sanchez, E. Baeyens, and R. Perez, "Comparative analysis of collision-free path-planning methods for multi-manipulator systems," *Robotica,* vol. 24, pp. 711-726, November 2006.

[152] F. R. Zypman, "Off-axis electric field of a ring of charge," *American Journal of Physics,* vol. 74, pp. 295-300, April 2006.

[153] R. N. Stiles, "Frequency and displacement amplitude relations for normal hand tremor," *Journal of Applied Physiology,* vol. 40, pp. 44-54, January 1976.

[154] W. F. Hughes and J. A. Brighton, *Schaums's Outline of Theory and Problems of Fluid Dynamics*. NY: McGraw-Hill, 1999.

[155] A. C. Ugural and S. K. Fenster, *Advanced Strength and Applied Elasticity*. Upper Saddle River: Prentice Hall, 2003.

[156] Y. Zhao, C. C. Lim, D. B. Sawyer, R. Liao, and X. Zhang, "Microchip for subcellular mechanics study in living cells," *Sensors and Actuators B: Chemical,* vol. 114, pp. 1108-1115, 2006.

[157] F. Schneider, T. Fellner, J. Wilde, and U. Wallrabe, "Mechanical properties of silicones for MEMS," *Journal of Micromechanics and Microengineering,* vol. 18, June 2008.

[158] J. E. Mark, *Polymer Data Handbook*. NY: Oxford University Press USA, 2009.

[159] X. Liu, Y. Sun, W. Wang, and B. M. Lansdorp, "Vision-based cellular force measurement using an elastic microfabricated device," *Journal of Micromechanics and Microengineering,* vol. 17, pp. 1281-1288, 2007.

[160] P. Soille, *Morphological Image Analysis: Principles and Applications*. New York: Springer-Verlag, 1999.

[161] P. V. C. Hough, "A method and means for recognizing complex patterns," *U.S. Patent No.3.069.654,* 1962.

[162] C. Kimme, D. Ballard, and J. Sklansky, "Finding circles by an array of accumulators," *Communications of the ACM,* vol. 18, pp. 120-122, 1975.

[163] R. O. Duda and P. E. Hart, "Use of Hough transformation to detect lines and curves in pictures," *Communications of the ACM,* vol. 15, 1972.

[164] F. Ogorman and M. B. Clowes, "Finding picture edges through collinearity of feature points," *IEEE Transactions on Computers,* vol. 25, pp. 449-456, August 1976.

[165] J. Gray and H. W. Lissmann, "The locomotion of nematodes," *The Journal of Experimental Biology,* vol. 41, pp. 135-54, March 1964.

[166] M. Asgari, A. Ghanbari, S. Nahavandi, and X. Chen, "3D particle-based cell modelling for haptic microrobotic cell injection," *in Proceedings of 15th International Conference on Mechatronics Technology,* pp. 1-6, 30 November - 2 December 2011.

[167] S. Faramarzi, A. Ghanbari, X. Chen, and W. Wang, "A PVDF based 3D force sensor for micro and nano manipulation," *in Proceedings of IEEE International Conference on Control and Automation,* pp. 867-871, 9-11 December 2009.

[168] T. Dohi, "Computer aided surgery and micro machine," *in Proceedings of 6th International Symposium on Micro Machine and Human Science* pp. 21-24, 4-6 October 1995.

[169] B. Young Min, Y. Kozuka, N. Sugita, A. Morita, S. Sora, R. Mochizuki, and M. Mitsuishi, "Highly precise master-slave robot system for super micro surgery," *in Proceedings of IEEE RAS and EMBS International Conference on Biomedical Robotics and Biomechatronics,* pp. 740-745, 26-29 September 2010.

[170] Y. Tian, Z. Jianxun, W. Shumei, T. Huan, and L. Wenqin, "Motion planning and error analysis in robot assistant micro-surgery system," *in Proceedings of 6th World Congress on Intelligent Control and Automation* vol. 2, pp. 8819-8823, 21-23 June 2006.

[171] M. Mitsuishi, K. Kobayashi, T. Watanabe, H. Nakanishi, H. Watanabe, and B. Kramer, "Development of an inter-world tele-micro-surgery system with operational environment information transmission capability," *in Proceedings of IEEE International Conference on Robotics and Automation,* vol. 3, pp. 3081-3088, 21-27 May 1995.

[172] M. Mitsuishi, T. Watanabe, H. Nakanishi, T. Hori, H. Watanabe, and B. Kramer, "A tele-micro-surgery system across the Internet with a fixed viewpoint/operation-point," *in Proceedings of IEEE/RSJ International Conference on Intelligent Robots and Systems,* vol. 2, pp. 178-185, 5-9 August 1995.

[173] M. Mitsuishi, H. Nakanishi, H. Watanabe, H. Kubota, and Y. Tomizawa, "A human interface which enables natural view selection during tele-micro-surgery," *in Proceedings of IEEE/RSJ International Conference on Intelligent Robots and Systems,* vol. 3, pp. 1203-1210, 4-8 November 1996.

[174] M. Mitsuishi, S. Tomisaki, T. Yoshidome, H. Hashizume, and K. Fujiwara, "Tele-micro-surgery system with intelligent user

interface," *in Proceedings of IEEE International Conference on Robotics and Automation* vol. 2, pp. 1607-1614, 24-28 April 2000.

[175] T. Tanikawa, Y. Hashimoto, and T. Arai, "Micro drops for adhesive bonding of micro assemblies and making a 3-D structure "micro scarecrow"," *in Proceedings of IEEE/RSJ International Conference on Intelligent Robots and Systems* vol. 2, pp. 776-781, 13-17 October 1998.

[176] J. T. Pierce-Shimomura, B. L. Chen, J. J. Mun, R. Ho, R. Sarkis, and S. L. McIntire, "Genetic analysis of crawling and swimming locomotory patterns in *C. elegans*," *Proceedings of the National Academy of Sciences of the United States of America,* vol. 105, pp. 20982-20987, 30 December 2008.

[177] S. Berri, J. H. Boyle, M. Tassieri, I. A. Hope, and N. Cohen, "Forward locomotion of the nematode *C. elegans* is achieved through modulation of a single gait," *Hfsp Journal,* vol. 3, pp. 186-193, June 2009.

[178] A. Cangelosi and D. Parisi, "A neural network model of Caenorhabditis elegans: The circuit of touch sensitivity," *Neural Processing Letters,* vol. 6, pp. 91-98, December 1997.

[179] M. Suzuki, T. Tsuji, and H. Ohtake, "A dynamic body model of the nematode *C. elegans* with a touch-response circuit," *in Proceedings of IEEE International Conference on Robotics and Biomimetics,* pp. 538-543, 5-9 July 2006.

[180] M. Suzuki, T. Takeshi Goto, T. Toshio, and O. Hisao, "A dynamic body model of the nematode *C. elegans* with neural oscillators," *Journal of Robotics and Mechatronics,* vol. 17, pp. 318-326, May 2005.

[181] J. Bryden and N. Cohen, "A simulation model of the locomotion controllers for the nematode Caenorhabditis elegans," in *From Animals to Animats 8*, S. Schaal*, et al.*, Eds., ed, 2004, pp. 183-192.

[182] R. Mailler, J. Avery, J. Graves, and N. Willy, "A biologically accurate 3D model of the locomotion of Caenorhabditis elegans," *in Proceedings of International Conference on Biosciences* pp. 84-90, 7-13 March 2010.